ZINC-BASED THIN FILMS FOR TRANSPARENT CONDUCTING OXIDE APPLICATIONS

DOMINIC POTTER

This thesis is submitted in partial fulfilment of the requirements for the Degree of Doctor of Philosophy (Chemistry)

2017

DECLARATION

I, Dominic B. Potter, confirm that the work presented in this thesis is my own. Where information has been derived from other sources, I confirm that this has been indicated in the thesis.

Dedicated to the loving memory of my grandpa, Martin Kaufman.

ABSTRACT

This thesis describes the synthesis of zinc-based transparent conducting oxide (TCO) thin films, as sustainable alternatives to commercial TCOs. There are two main aims to this work. The first is the discovery of suitable TCO materials, which involves finding the optimum optoelectronic properties for applications in photovoltaic devices. The second aim is investigating the scale up of aerosol assisted chemical vapour deposition (AACVD), which is the technique used to deposit the majority of the films in this work.

The films deposited in this work were characterised by X-ray diffraction (XRD) to find the crystal structures, X-ray photoelectron spectroscopy (XPS) to find the elemental compositions, scanning electron microscopy (SEM) to analyse the surface morphologies, UV/vis spectroscopy to find the optical properties, and by Hall effect measurements to find the electrical properties.

Aluminium, gallium, indium, silicon, and fluorine have been examined as dopants for ZnO, in various combinations, and at different concentrations. The films were generally found to have high transparency, and electrical properties that approached those of industrial TCO materials. The merits of the films are particularly promising, when considering the relative ease through which the films were synthesised. Additionally, the effect of varying the solvent used to make up the precursor solution is investigated. The deposition of $ZnSb_2O_6$ thin films *via* spin coating is also discussed.

This thesis also details an investigation into the scale-up of AACVD. An aerosol transport study was performed, whereby the aerosol was transported prior to deposition. It was found that a considerable

amount of aerosol was condensing within the tubing, prior to reaching the reactor. Additionally, increasing the film growth rates was investigated by depositing FTO films using high concentrations in the precursor solution. Growth rates of approximately 2 μm min^{-1} were achieved, making the use of AACVD for commercial applications significantly more feasible.

PUBLICATIONS

1. **D. B. Potter**, D. S. Bhachu, M. J. Powell, J. A. Darr, I. P. Parkin, C. J. Carmalt, “Al-, Ga-, and In-doped ZnO thin films via aerosol assisted CVD for use as transparent conducting oxides,” *Physica Status Solidi A*, 2016, vol. 7, no. 5, pp. 1346-1352.

2. **D. B. Potter**, M. J. Powell, J. A. Darr, I. P. Parkin, C. J. Carmalt, “Transparent conducting oxide thin films of Si-doped ZnO prepared by aerosol assisted CVD,” *RSC Advances*, 2017, vol. 7, pp. 10806-10814.

3. D. S. Y. Jayathilake, T. A. Nirmal Peiris, J. S. Sagu, **D. B. Potter**, C. J. Carmalt, D. J. Southee, “Microwave-Assisted Synthesis and Processing of Al-Doped, Ga-Doped, and Al, Ga Codoped ZnO for the Pursuit of Optimal Conductivity for Transparent Conducting Oxide Film Fabrication,” *ACS Sustainable Chemistry & Engineering*, 2017, vol. 5, pp. 4820-4829.

4. M. J. Powell, **D. B. Potter**, R. L. Wilson, J. A. Darr, I. P. Parkin, C. J. Carmalt, “Scaling aerosol assisted chemical vapour deposition: Exploring the relationship between growth rate and film properties,” *Materials and Design*, 2017, vol. 129, pp. 116-124.

5. P. I. O. Filho, **D. B. Potter**, M. J. Powell, C. J. Carmalt, P. Angeli, E. S. Fraga, "Probability Density Functions for Aerosol Transport Modelling," *27th European Symposium on Computer Aided Process Engineering*, 2017, vol. 4, pp. 2245-2250.

6. I. Swiatkowska, J. F. W. Mosselmans, T. Geraki, C. C. Wyles, J. J. Maleszewski, J. Henckel, B. Sampson, **D. B. Potter**, I. Osman, R.

T. Trousdale, A. J. Hart, "Synchrotron analysis of human organ tissue exposed to implant material," *Journal of Trace Elements in Medicine and Biology*, 2018, vol. 46, pp. 128-137.

7. **D. B. Potter**, M. J. Powell, I. P. Parkin, C. J. Carmalt, "Aluminium/gallium, indium/gallium, and aluminium/indium co-doped ZnO thin films deposited via aerosol assisted CVD," *Journal of Materials Chemistry C*, 2017 (Accepted).

8. M. J. Powell, B. A. D. Williamson, S.-Y. Baek, J. Manzi, **D. B. Potter**, D. O. Scanlon, C. J. Carmalt, “Phosphorous Doped SnO_2 Thin Films with Excellent Optical and Electrical Properties for Transparent Conducting Oxide Applications,” *Chemical Science*, 2017 (Submitted).

ACKNOWLEDGEMENTS

Firstly, I would like to sincerley thank my supervisors for this project, Professor Claire Carmalt, and Professor Ivan Parkin, for the continual support and inspiration they provided me with. Thank you for always finding time for me, and for guiding me through the last three years.

Secondly, a huge thanks to Michael for constantly offering support to help me finish this project, and for being great to work with every day. Thanks to Michael for collaborating on the the work described in Section 6.4.

I would like to thank Dav for getting me started in the lab during my first few months. I am also very grateful to Sanjay, Caroline, and Nick, who were always around to help when I needed it. I would like to thank the other academic staff at UCL — Eric Fraga, Jawwad Darr, Rob Palgrave, and David Scanlon. Additionally, I would like to thank the technical staff — Steve Firth, Martin Vickers, Tony Field, Joe Nolan, Tom Bridges, John Cowley, and everyone in the workshop.

A big thanks to every single person in the Carmalt/Parkin research group, who made it a pleasure to come to the lab each day. You have all been a delight to work with. I feel very lucky to have had the chance to work in such a cooperative, helpful environment.

I am very grateful to Simon and everyone else at NSG for their guidance, and for being such great hosts when I had the opportunity to work with them at Lathom. I am also grateful to Fraser and everyone at Malvern for hosting me there. I would also like to thank everyone at Loughborough for collaborating on this project and helping to get some great results.

I owe a great debt to my parents for all the support they have provided. Thank you so much for always being there. I am eternally grateful for everything you have given me.

Finally, I would like to thank my fiancée Ilona for being there for me at the end of every day. I would never have made it this far without you.

This thesis exists thanks to you all.

CONTENTS

LIST OF FIGURES

LIST OF TABLES

ACRONYMS

AACVD	Aerosol assisted chemical vapour deposition
AGZO	Aluminium/gallium co-doped zinc oxide
AIZO	Aluminium/indium co-doped zinc oxide
ALD	Atomic layer deposition
AO	Atomic orbital
APCVD	Atmospheric pressure chemical vapour deposition
AZO	Aluminium-doped zinc oxide
BGN	Band gap narrowing
BM	Burstein-Moss
CBM	Conduction band minimum
CVD	Chemical vapour deposition
CPS	Counts per second

FACVD	Flame assisted chemical vapour deposition
FSZO	Fluorine/silicon co-doped zinc oxide
FTO	Fluorine-doped tin oxide
FWHM	Full-width at half maximum
FZO	Fluorine-doped zinc oxide
GSAS	General Structure Analysis System
GZO	Gallium-doped zinc oxide
IGZO	Indium/gallium co-doped zinc oxide
IPA	Isopropyl alcohol
ITO	Tin-doped indium oxide
IZO	Indium-doped zinc oxide
LCD	Liquid crystal display
LED	Light emitting diode
LPCVD	Low pressure chemical vapour deposition
MO	Molecular orbital
NIR	Near infrared
PECVD	Plasma enhanced chemical vapour deposition
PLD	Pulsed laser deposition
PVD	Physical vapour deposition
RPM	Revolutions per minute
SEM	Scanning electron microscopy
SZO	Silicon-doped zinc oxide
TCO	Transparent conducting oxide
TEOS	Tetraethyl orthosilicate
TFA	Trifluoroacetic acid

THF	Tetrahydrofuran
UHVCVD	Ultra high vacuum chemical vapour deposition
UV	Ultraviolet
VBM	Valence band maximum
XPS	X-ray photoelectron spectroscopy
XRD	X-ray diffraction

Part I

INTRODUCTION AND EXPERIMENTAL METHODS

1

INTRODUCTION

1.1 GENERAL INTRODUCTION

This thesis describes the deposition of transparent conducting oxide (TCO) thin films onto glass substrates. TCOs are a unique subset of semiconductors which are both optically transparent and electrically conductive.

Typical industrial TCO materials are tin-doped indium oxide, also known as indium-tin-oxide (ITO), and fluorine-doped tin oxide (FTO). These materials are favoured due to their excellent optoelectronic properties. They display optical transparency above 80% and resistivity as low as, or lower than 10^{-4} Ω·cm. However, despite their desireable properties, ITO and FTO are becoming less and less feasible for commercial applications due to the unstable price of raw indium and tin. For this reason, a significant amount of research has focussed on alternative TCO materials, made from inexpensive, more Earth-abundant elements. One such material is doped zinc oxide [ZnO], which is the main focus of this thesis. Another benefit of zinc oxide is the relatively low toxicity of zinc, in comparison to both indium and tin.[1]

In this work, the technique used to deposit TCO thin films is a variation of chemical vapour deposition (CVD), known as aerosol assisted chemical vapour deposition (AA)CVD. AACVD uses an aerosol mist generated from a precursor solution as the mechanism for transporting the precursors to the substrate. This has several

advantages over conventional CVD, which will be explained later in this chapter. At present, AACVD has not been used as an industrial deposition technique. However, it has the potential to be scaled up due to its versatility, and the ease through which effective functional coatings can be deposited at a laboratory scale.

To establish context for the results in this thesis, this introductory chapter will outline TCOs, and discuss the reasons for their optoelectronic properties. The intricacies and advantages of AACVD will also be overviewed. Subsequently, there will be a chapter explaining the experimental and analytical techniques used. Following this, the experimental work conducted for this research project will be outlined and the results discussed.

1.2 TRANSPARENT CONDUCTING OXIDES

Transparent conducting oxides (TCOs) are an important class of semiconductor material which combine electrical conductivity with optical transparency — two properties which would usually be considered to be mutually exclusive.[2,3] The reason for this phenomenon can be explained by examining the band structure of TCO materials.

1.2.1 *Band Theory*

Band theory builds upon the knowledge of the behaviour of electrons in atoms and molecules, and expands it to explain how electrons behave in a solid. Thus, band theory provides insight into bulk material properties such as conductivity and transparency, from a fundamental perspective.

To understand band theory, it is necessary to understand how electrons behave in a solid. A solid can be regarded as giant molecule. As the number of atoms being brought together increases, the separation between the energy levels of the discrete molecular orbitals (MOs) will decrease, as shown in Figure 1.1. When the number of atoms approaches infinity, the energy levels will be so closely spaced that they will effectively resemble a continuum, known as a band. The energy range of a band can extend over several electronvolts (eVs), depending on the interatomic spacing of the crystal.[4,5] Between bands, there are no available electronic states. The space between bands is called the band gap, $\mathrm{E_g}$.

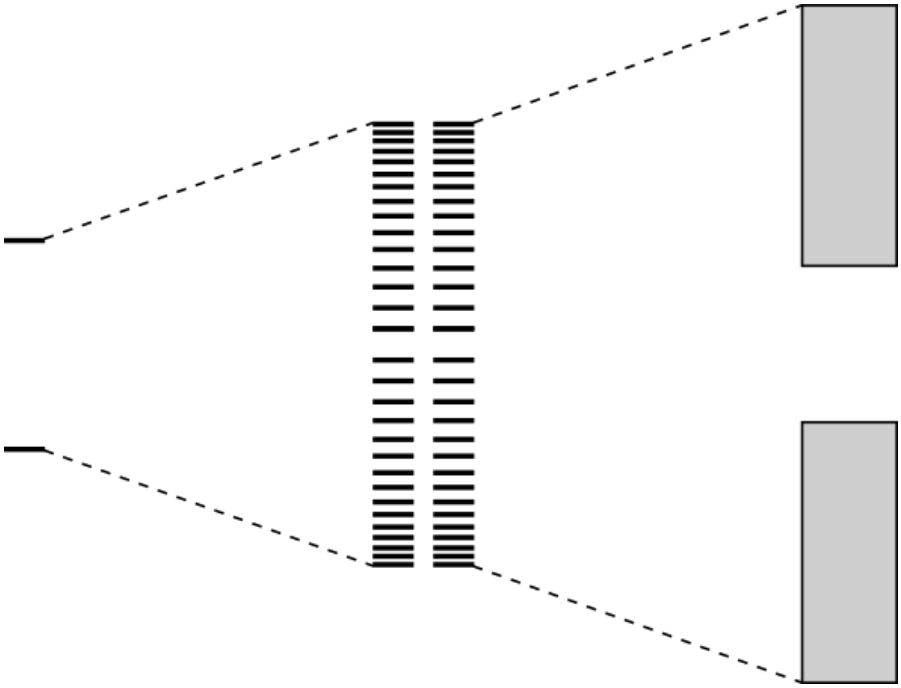

Figure 1.1: Variation in MOs with increasing number of AOs, until continuous bands emerge.

The overlap of different types of atomic orbitals (AOs) results in different types of band, each with different energy ranges. In general, the overlap of bonding AOs results in lower energy bands known as valence bands, whilst the overlap of antibonding AOs results in higher energy bands known as conduction bands.[6] Electronic bands

can be empty, filled, or partially filled. The promotion of an electron to the conduction band results in an electron in an excited state, known as an exciton, which has an associated “electron hole” that remains in the valence band. The hole is effectively the inverse of an electron, and possesses a positive charge. The excited electrons and the associated holes are free to move within their respective band, and thus they are able to carry charge.

The Fermi level, $\mathrm{E_F}$, represents the energy of the highest occupied energy level at absolute zero. In a metal, $\mathrm{E_F}$ lies within a band, and thus thermal excitations of electrons into higher energy levels at temperatures above absolute zero are easy, resulting in a high conductivity. Furthermore, in a metal, the valence band maximum (VBM) lies at a higher energy than the conduction band minimum (CBM), so virtually no energy is required to delocalise a bound electron, to allow it to carry charge. This makes metals extremely good electrical conductors.

Conversely, there can also be a separation between the bands, i.e. a band gap, $\mathrm{E_g}$. In an insulator, $\mathrm{E_g}$ is so large that it is very difficult to promote an electron, hence why insulators are very poor electrical conductors.

A semiconductor can act as an electrical insulator or an electrical conductor, depending on the conditions. It possesses a band gap which is wider than that of a metal, but narrower than that of an insulator. This means that semiconductors usually act as insulators at low temperatures, but electrons can be excited from the valence band to the conduction band by heating or irradiating the material. Therefore, the electrical conductivity of a semiconductor tends to increase at higher temperatures — behaviour which is opposite to that of a metal. In a metal, the conductivity reduces at higher

temperatures due to resistance caused by thermal vibrations within the lattice.

An *i*-type or intrinsic semiconductor is one that is an undoped material, which does not contain a significant amount of intentional or unintentional impurities. The charge carrier concentration is therefore controlled by the material itself, rather than the effect of external species. At finite temperature, $\mathrm{E_F}$ for an *i*-type semiconductor lies halfway between the VBM and the CBM. Any electrical conductivity in an *i*-type semiconductor is due to crystallographic defects (such as oxygen vacancies) or thermal electronic excitation. In an intrinsic semiconductor, the number of excited electrons must be equivalent to the number of holes left in the valence band, since the promotion of an electron to the conduction band will always leave an electron hole in the valence band.

Impurities are often intentionally introduced into the crystal lattice, in a process known as doping. This is done to improve the electronic properties of the material. Semiconductors which have been doped are known as extrinsic semiconductors. The dopant elements can substitute for ions of the host material, or they can insert interstitially into the gaps between ions (Figure 1.2).

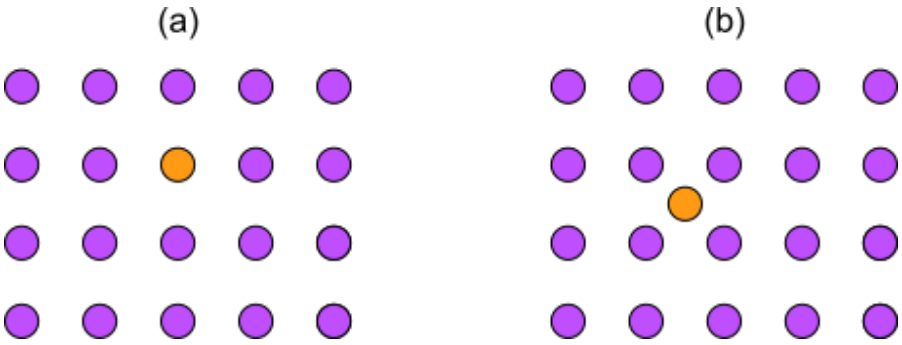

Figure 1.2: Schematic representations of (a) substitutional and (b) interstitial defects.

If the valency of the dopant atoms is higher than the valency of the atoms of the bulk, the additional electrons will occupy a discrete energy level below the conduction band, known as a donor level (Figure 1.3a). The separation between the donor level and the CBM is much smaller than $\mathrm{E_g}$, which makes the promotion of electrons to the conduction band a relatively low energy process, and hence the number of electrons free to carry charge increases. The majority charge carriers in this case are electrons, and this type of material is known as an *n*-type semiconductor.[2]

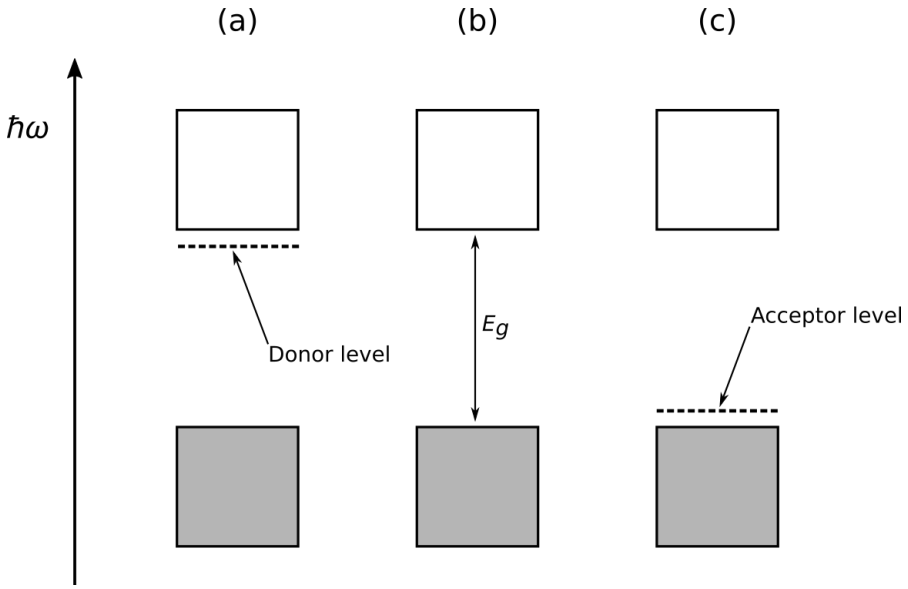

Figure 1.3: Band structures of (a) *n*-type semiconductors, (b) *i*-type semiconductors, and (c) *p*-type semiconductors.

Conversely, if the valency of the dopant atoms is lower than the valency of the atoms of the bulk, there will be a deficiency of electrons in comparison to the pure material. This introduces a discrete, unoccupied energy level above the valence band known as an acceptor level (Figure 1.3c). The separation between the acceptor level and the VBM is much smaller than $\mathrm{E_g}$, and thus thermal occupation of the acceptor level is easily achievable. Generally, the electrons that occupy the acceptor level do not contribute to the overall conductivity of the material.[7] However, the positive holes left

behind in the valence band act as majority charge carriers. This type of material is known as a *p*-type semiconductor.[6]

1.2.2 *Effects of Doping on the Band Gap*

Doping is where atoms or ions of a host matrix are "substituted" for external impurity species, which can affect the optoelectronic properties of the material. An example of this in nature is the mineral corundum, which is a naturally occurring crystalline form of aluminium oxide [Al_2O_3]. It is often transparent and colourless, however when some of the Al^{3+} ions are replaced with impurity ions, the colour of the mineral can change. Randomly substituting approximately 1% of the Al^{3+} ions with Cr^{3+} ions will result in the red gemstone commonly known as ruby. This is achieved through d-d transitions within the chromium chromophore.[8] In fact, similar substitutions are the cause of the colouring in many naturally occurring gemstones.[9,10]

Upon introducing dopant elements into a semiconductor, changes in the band gap are often observed. This is due to the competing effects of the Burstein-Moss effect and the band gap narrowing effect.

1.2.2.1 *Burstein-Moss Effect*

The Bursten-Moss (BM) effect is related to the electron density, or carrier concentration of a material.[11–13] This means that it often becomes more pronounced upon doping, a process which regularly results in an increase in carrier concentration.

The BM effect is a band gap widening process. It is the result of the lower energy levels of the conduction band being filled by the excess electrons provided by the dopant elements. This raises the energy of the Fermi level.[14–16]

The BM shift is given by:

$$\Delta E_{BM} = \frac{h^2}{8\pi^2} \cdot (3\pi^2 n)^{\frac{2}{3}} \cdot \left(\frac{1}{m_e^*} + \frac{1}{m_h^*} \right) \tag{1.1}$$

where h is Plank's constant, n is the electron density, or carrier concentration, m_e^* is the effective mass of electrons ($0.28 m_e$ for ZnO), and m_h^* is the effective mass of holes ($0.59 m_e$ for ZnO).[17–20] Equation 1.1 predicts a band gap energy shift proportional to $n^{\frac{2}{3}}$.[21]

The resulting band gap, considering only the BM effect, is given by:

$$E_{BM} = E_o + \Delta E_{BM} \tag{1.2}$$

where E_o is the band gap of the undoped material. In undoped ZnO for example, the band gap is taken to be ~3.37–3.38 eV at room temperature.[14,22–24]

1.2.2.2 *Band Gap Narrowing Effect*

Like the BM effect, the band gap narrowing (BGN) arises from the excess of charge carriers.[14,17,18,25] It is caused by a combination of several effects:

- Exchange interactions between the electrons (ΔE_{ex}). Electrons have a mutually repulsive Coulomb interaction given by e^2/r. The Fermion nature of the particles tends to keep ones with like spin away from each other. This spatial exclusion reduces the amount of repulsive energy the electrons would have from a uniform distribution of particles. This reduction in repulsive energy is equivalent to an attractive energy, which is called the exchange energy. The exchange interaction between the electrons results in a shift in the CBM towards lower energies.

- Interactions between the electrons and the holes (ΔE_{eh}). This is also known as correlation energy. When an electron is excited from the valence band to the conduction band, it leaves behind an associated, positively charged electron hole. The attractive electrostatic force between the positive holes and the negative electrons results in the electrons and holes arranging themselves to minimise their energy. This interaction between the electrons and the holes results in a shift in the VBM towards higher energies.

- Interactions between electrons and the impurity ions (ΔE_{ei}). If each donor element donates a single electron, then it will be left with a single positive charge. The attractive electrostatic force between the positive ions and the negative electrons causes small electron clouds to gather around the impurities. This configuration has a lower energy as compared to that in which the electrons are randomly distributed. This interaction between the electrons and the impurities results in a shift in the CBM towards lower energies.

- Interactions between holes and the impurity ions (ΔE_{hi}). In an *n*-type semiconductor, where electrons are the majority charge carrier, this type of interaction is less significant. The attractive electrostatic force between the positive holes and the negative electrons results in holes moving towards regions of higher electron density, such as the electron clouds surrounding impurity ions. This many body interaction between the holes and the impurities results in a shift in the VBM towards higher energies.

These four shifts combine to give the total BGN shift, which is given by:

$$\Delta E_{BGN} = \Delta E_{ex} + \Delta E_{eh} + \Delta E_{ei} + \Delta E_{hi} \tag{1.3}$$

This expression can be expanded to the following equation, under the assumption that the electron concentration is equivalent to the donor concentration (i.e. each donor ion donates a single electron):

$$\Delta E_{BGN} = 1.83 \cdot \frac{\Lambda}{N_b^{1/3}} \cdot \frac{R}{r_s} + \frac{0.95R}{r_s^{3/4}} + \left[1 + \frac{m_{min}}{m_{maj}}\right] \cdot \frac{1.57R}{N_b r_s^{3/2}} \tag{1.4}$$

where m_{maj} and m_{min} are the majority and minority charge carrier effective masses, respectively, Λ is the correction factor due to the anisotropy (i.e. directional dependence) in the conduction band. Λ is usually between 0.75 and 1. In the case of *n*-type ZnO, Λ can be taken to be 1, as it is very similar to *n*-type GaAs, which is also taken to be 1.[17,26] N_b is the number of equivalent minima in the conduction band for *n*-type semiconductors (or maxima in the valence band for *p*-type semiconductors) and its value can also be taken to be 1, for the same reason as above. R is the effective Rydberg energy for a carrier bound to a dopant atom, and is related to the binding energy of the electron. It is given by:

$$R = \frac{13.6 m_r}{\epsilon_r^2} \tag{1.5}$$

where m_r is the ratio of the effective mass of electrons in the conduction band and the free electron mass, or $0.28 m_e/m_e = 0.28$.[14,17,20] ϵ_r is the dielectric constant of the material. The dielectric

constant of a doped material is usually unavailable, so the dielectric constant of the pure material should be used instead. This is a valid assumption, because the concentration of dopant is usually relatively small. The dielectric constant for pure ZnO is 8.65.[19] r_s is the average distance between majority carriers, normalised to the effective Bohr radius (approximately equal to the most probable distance between the proton and electron in a hydrogen atom in its ground state), and is given by:

$$r_s = \frac{r_a}{a} \tag{1.6}$$

where r_a is half the average distance between donor atoms, and a is the Bohr radius of the donors in ångstroms (1 Å $= 10^{-10}$ m). They are given by the following formulae:

$$r_a = \left(\frac{3}{4\pi N}\right)^{1/3} \tag{1.7}$$

and

$$a = \frac{0.53\epsilon_r}{m_r} \tag{1.8}$$

Here, N is the impurity concentration. In the case of an *n*-type semiconductor like ZnO, this is the donor concentration. For aluminium/gallium/indium-doped ZnO, each dopant atom donates one electron to the ZnO lattice. Therefore N is equal to the carrier concentration.

m_{maj} and m_{min} are the majority carrier and minority carrier effective masses, respectively. Thus, for an *n*-type semiconductor, $m_{maj} = m_e^*$ and $m_{min} = m_h^*$.

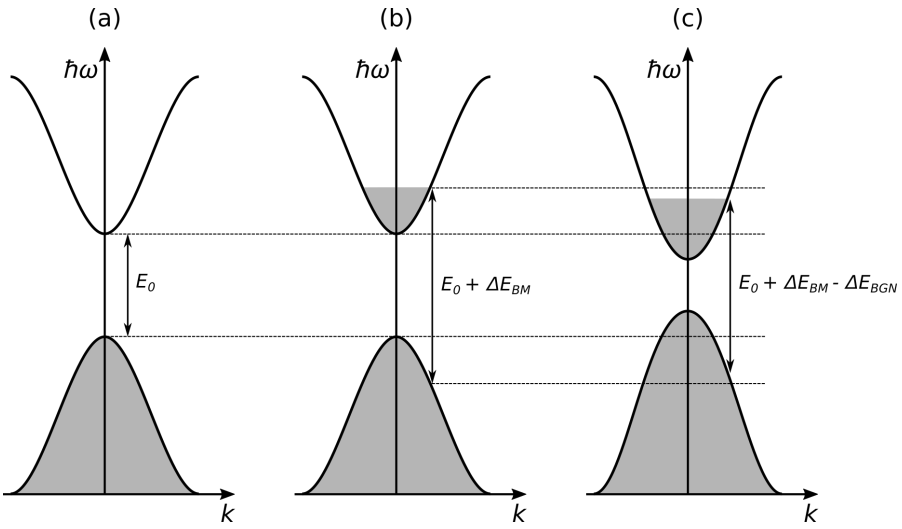

Figure 1.4: Schematic diagram showing (a) band gap of a pure, undoped semiconductor, (b) band gap widening due to the Burstein-Moss effect, and (c) total band gap due to both the Burstein-Moss effect, and the band gap narrowing effect.

The resulting band gap, considering only BGN, is given by:

$$\mathrm{E_{BGN}} = \mathrm{E_o} - \Delta\mathrm{E_{BGN}} \tag{1.9}$$

1.2.2.3 *Total Band Gap*

Finally, by combining the equation for the band gap due to the BM effect (Equation 1.2) and the equation for the band gap due to the BGN effect (Equation 1.9), the total band gap can be calculated:

$$\mathrm{E_{tot}} = \mathrm{E_o} + \Delta\mathrm{E_{BM}} - \Delta\mathrm{E_{BGN}} \tag{1.10}$$

The results of the BM effect and the BGN effects are shown in Figure 1.4. It is clear that doping has a significant effect on the electrical properties of a semiconductor.

In addition, the optical properties are affected by these band gap effects, as the colour and transparency of a material is largely

dependant on its band gap. This is because these optical properties are related to the energy of the photons that are absorbed by the material, which is determined by the energy required to excite a valence electron to the conduction band.

Therefore, doping is fundamentally important for TCOs, as it allows the band gap to be tuned to give specifically desired optoelectronic functional properties. Doped TCOs have found several applications as components of photovoltaic devices. Consequently, there is a large industry producing TCOs for commercial applications.

1.2.3 *Tin-Doped Indium Oxide*

One of the most commonly used industrial TCO material is tin-doped indium oxide, or indium-tin-oxide (ITO). ITO films are typically grown industrially *via* magnetron sputtering. It has also been deposited on the laboratory scale *via* CVD.[27,28] ITO films retain the same cubic bixbyite crystal structure as undoped indium oxide [In_2O_3], but doping with tin results in an increase in the lattice parameters. This can be explained by the substitutional incorporation of Sn^{2+} ions (0.93 Å) into the In^{3+} (0.79 Å) sites and/or into interstitial positions.

Undoped indium oxide is a wide bandgap material (E_g ~3.75 eV at room temperature), which allows for high transparency of visible light. For films deposited *via* pulsed laser deposition (PLD), the bandgap has been shown to increase up to ~4.2 eV as the film was doped with tin.[29] This is a result of an increase in the carrier concentration, leading to the Burstein-Moss effect. Increasing the tin content further resulted in a slight decrease in the bandgap to ~4.1 eV. This was attributed to the excess tin causing crystal disorder, as well as acting as carrier traps rather than electron donors, due to the formation of impurity phases, such as Sn_2O, Sn_2O_4, and SnO.[30]

ITO thin films are *n*-type semiconductors, meaning delocalised electrons are the majority charge carrier. Highly conductive ITO films have been synthesised with resistivities as low as 10^{-5} Ω·cm, carrier concentrations on the order of 10^{21} cm^{-3}, and Hall mobilities which are approximately 30-100 $cm^2/V{\cdot}s$.[31–34]

1.2.4 *Fluorine-Doped Tin Oxide*

Another commonly used TCO material is fluorine-doped tin oxide, also known as fluorine-tin-oxide (FTO). FTO films were originally deposited *via* spray pyrolysis, and used as antifog coatings for aircraft during the second world war. By 1990, FTO coatings were being deposited industrially *via* APCVD.[35]

FTO films maintain the rutile structure of bulk tin oxide [SnO_2]. Unlike ITO films, doping with fluorine does not result in an increase in the lattice parameters.[36,37] This is because F^- has a smaller ionic radius (1.17 Å) than O^{2-} (1.22 Å).[38] For this reason, fluorine-doping typically results in a contraction of the unit cell in FTO films.[39]

Undoped tin oxide has a bandgap of ~3.6 eV at room temperature.[40] Doping with fluorine has been shown to increase the bandgap to ~4.2 eV at room temperature, again due to the Burstein-Moss effect.[41]

Like ITO, FTO films are *n*-type semiconductors. Highly conductive FTO films have been synthesised with resistivities as low as 10^{-4} Ω·cm, carrier concentrations on the order of 10^{20} cm^{-3}, and Hall mobilities which are approximately 1-20 $cm^2/V{\cdot}s$.[42–45]

1.2.5 *Zinc Oxide*

Both indium and tin are mined in geopolitically unstable regions. As a result, their cost per kilogram fluctuates considerably, as shown by

the Mineral Commodity Summaries generated by the U.S. Geological Survey over the last two decades.[46–65] Tin and indium are often expensive to import, which heavily affects industries that use them. This has led to a search for substitute TCOs.

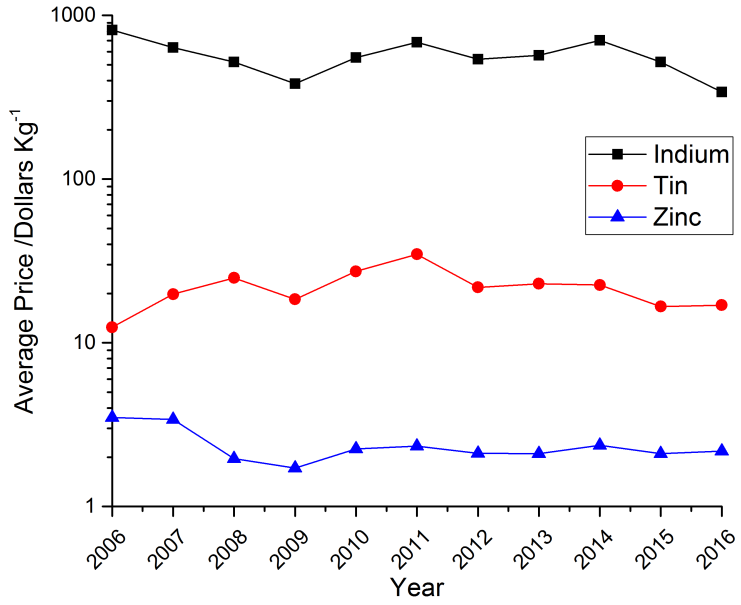

Figure 1.5: Average price of indium, tin and zinc over the last decade, in dollars per kilogram.[54–65] Note the low cost and relative stability of zinc.

A promising alternative TCO material is doped ZnO. There is a much higher natural abundance of zinc in comparison to both indium and tin.[66] Consequently, the cost of zinc is significantly lower and more stable, as shown in Figure 1.5. This means that there is a wide selection of relatively inexpensive zinc-containing precursors available. Hence, effective zinc-based TCO materials can be synthesised at a low cost. Additionally, zinc has a relatively low toxicity, which makes it preferable for handling in large quantities, such as in an industrial manufacturing plant.

ZnO usually crystallises in the hexagonal wurtzite phase, whereby Zn^{2+} cations and O^{2-} anions both sit in tetrahedral sites (Figure 1.6a). The wurtzite structure is more thermodynamically stable than other

possible phases, such as zinc blende (Figure 1.6b), which requires a cubic substrate, and cubic rocksalt (Figure 1.6c), which requires higher growth temperatures.[67]

ZnO has a wide, direct band gap (E_g ~3.37 eV at room temperature), resulting in high optical transparency. Undoped ZnO has an inherent *n*-type conductivity. The source of this intrinsic conductivity is disputed. Traditionally, it was thought to be a result of native defects such as oxygen vacancies (V_O) or zinc interstitials (Zn_I).[67–69] Zn_I defects act as shallow donors. This means that they form energy levels that sit just below the CBM, and as such, there is a small energy gap for electrons to overcome in order to be promoted into the conduction band. However, Zn_I defects have a high formation energy and a low mobility, and are therefore unlikely to be stable at high concentrations in *n*-type ZnO.[70] Conversely, V_O defects are thought to act as a doubly charged deep donor, and hence it is not likely that they will contribute significantly to the carrier concentration.[70–73]

The interaction between these two defects can form a V_O–Zn_I complex. This complex has been investigated *via* computational studies as another potential cause of native *n*-type conductivity in ZnO, since it is also a shallow electron donor, and has a lower formation energy than the sum of its two component point defects. However, although the two defects can be trapped together kinetically, the V_O–Zn_I complex still has a high formation energy and is thermodynamically unstable.[74]

Another possible cause of the inherent conductivity in ZnO is hydrogen-doping. Since hydrogen is difficult to fully eliminate from growth environments, it is usually unintentionally incorporated into ZnO. Computational studies have shown that, in ZnO, hydrogen occurs exclusively in the positive charge state, because H^+ is stable

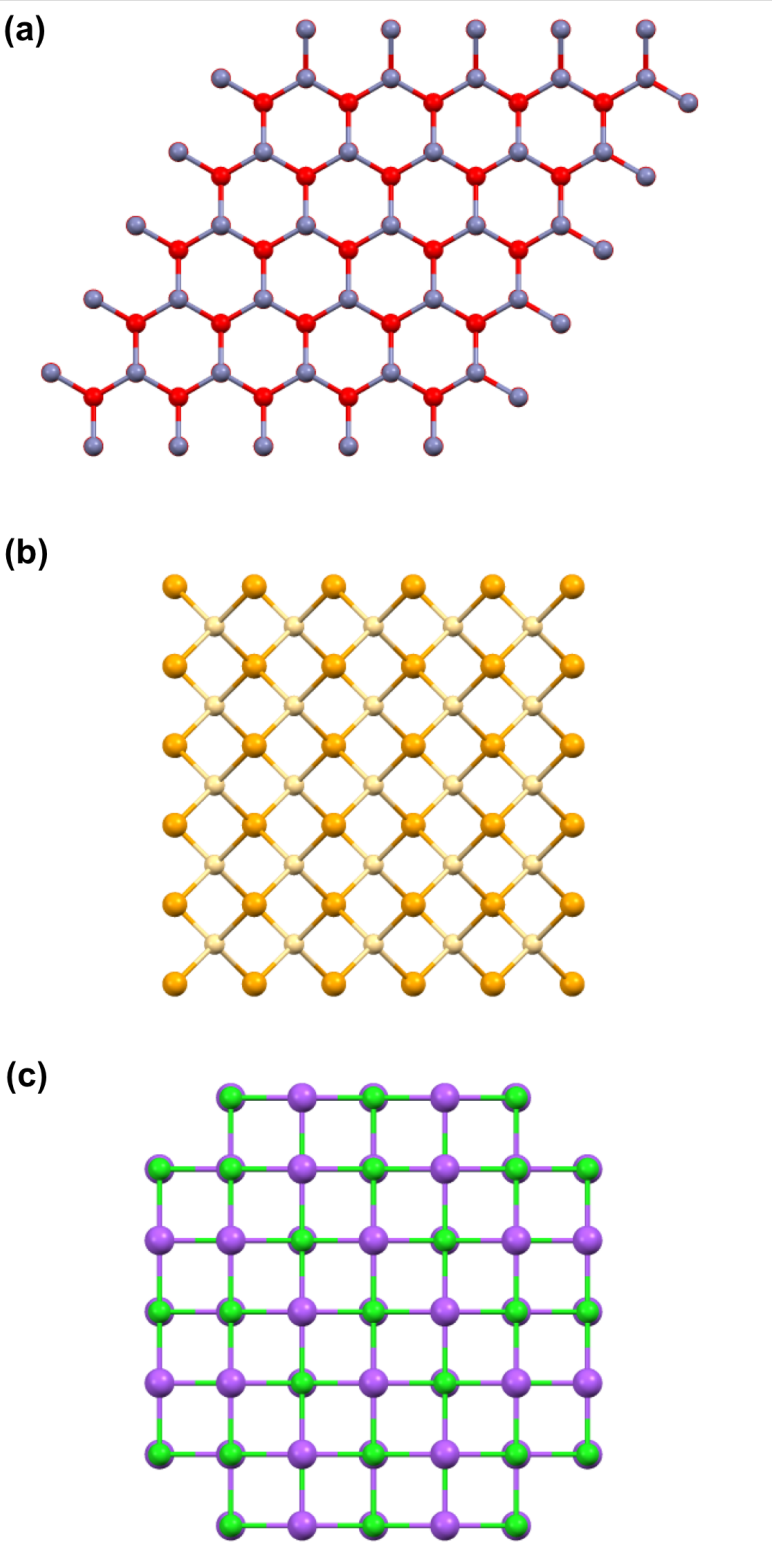

Figure 1.6: Looking along the *c*-axes of the three main crystal structures of ZnO: (a) wurtzite (ICSD #82028), (b) zinc blende (ICSD #41528), and (c) rock salt (ICSD #100633).

for all positions of the Fermi level within the band gap. Hence, it is always a donor in ZnO.[75,76]

There are two main sites where H^+ can exist in ZnO. Computational studies have shown that substitutional hydrogen on an oxygen site (H_O) in a multi-centre bond configuration forms a shallow donor state in ZnO.[77] Under oxygen-poor conditions, the formation energy of H_O is only ~0.1 eV higher than the formation energy of interstitial hydrogen (H_I), and hence the two forms of hydrogen are likely to co-exist in equilibrium. In oxygen-rich conditions, the formation energy of H_O significantly increases, and thus it will be less prominent. The concentration of H_I is also sample dependent, due to the high mobility of H_I and thermal conditions during synthesis. H_I is unstable at high temperatures, hence H_O will dominate in annealed samples, or samples synthesised at high temperatures.

Despite the intrinsic *n*-type conductivity of ZnO, the conductivity is generally not sufficient for applications in photovoltaic devices.[78] In order to improve the conductivity, doping is necessary. There are many known dopants for ZnO.[31] The most commonly investigated of these are the group 13 elements — in particular, aluminium, gallium and indium.

Conversely, *p*-type doping is less easy to achieve for ZnO, due to a lower thermodynamic stability of *p*-type defects.[79] It has even been observed that *p*-type ZnO reverts to *n*-type ZnO within a matter of days.[67] Hence, *n*-type ZnO is more commonly reported, as it is stable at high temperatures, which make it ideal for the commercial fabrication of various devices.[80]

1.2.6 *Applications*

As a result of their high optical transparency, and low electrical resistivity properties, TCOs have found applications in various photovoltaic devices, such as solar cells, light-emitting diodes (LEDs), liquid crystal displays (LCDs) and touch-screen displays.

ZnO in particular has been used as a component in several devices. Its wide room temperature bandgap (3.37 eV) is similar to that of gallium nitride [GaN] (3.44 eV). This enables applications for both materials in optoelectronics in the blue/UV region, such as LEDs, laser diodes, and photodetectors.[81]

A significant advantage of ZnO over GaN is that the exciton binding energy of ZnO (60 meV) is much larger than that of GaN (25 meV). For this reason, efficient excitonic emissions can occur in ZnO at room temperature and above. This makes ZnO suitable for use in devices that are based on excitonic effects, such as photon storage devices, and transistors.[82] ZnO also displays strong luminescence in the green–white region of the spectrum. As such, it is a suitable material for use in phosphor applications.[80] In addition, the *n*-type conductivity of ZnO means that it can be used in vacuum fluorescent displays.

The low symmetry of the ZnO wurtzite structure, along with a large electromechanical coupling means that ZnO can efficiently convert between electrical and acoustic energy. For this reason, ZnO shows strong piezoelectric properties, and can be used in devices such as sensors, transducors and actuators.[83]

The conductivity of ZnO has also been shown to be dependant on surface bound gases. It has been used as a sensor to detect the freshness of various foods and drinks, by detecting trimethylamine — a common decomposition product of plants and animals.[84]

Commercially available ceramic ZnO varistors are widely used to protect electrical powerlines and other electronic components from power surges. Electron trapping and hole creation at grain boundaries is thought to give rise to the non-linear resistance when a large potential difference is applied.[85]

The high thermal conductivity of ZnO has also led to its use as an additive. One application is the addition of ZnO to rubber in order to increase the thermal conductivity of tyres, to improve their lifetime. The high thermal conductivity also allows ZnO to be used as a substrate for the homoepitaxial or heteroepitaxial deposition of materials with similar lattice constants.[80]

ZnO can be etched at low temperatures using a variety of acidic or alkaline solutions. This is beneficial for device fabrication procedures, as the potential for low temperature etching allows for flexibility in the processing, design, and integration of various optoelectronic devices.

Finally, ZnO has been shown to exhibit high radiation hardness, moreso than GaN. This means that it is highly resistant to damage or malfunctions caused by ionising radiation. This is important for electronic devices which are used at high altitudes, or in space.

Thus, ZnO is an important material, with many useful applications. This thesis will focus on the TCO applications of ZnO. ZnO-based TCOs are an important component in many optoelectronic devices, and extensive research has been done into ZnO thin films grown by a variety of techniques.

1.3 CHEMICAL VAPOUR DEPOSITION

There are several known methods to deposit a thin TCO film onto a glass substrate. They can be separated into physical vapour

deposition (PVD) techniques, and chemical vapour deposition (CVD) techniques. This thesis focusses on the latter.

CVD is a method regularly employed to deposit thin film coatings. Unlike physical vapour deposition (PVD) in which a physical process occurs to deposit the film (e.g. evaporation and condensation), CVD requires a chemical reaction between gaseous precursor compounds by utilising an energy source such as heat, light, or plasma.[86] Traditional CVD methods involve the vaporisation of volatile precursors, usually by heating them to high temperatures in a bubbler. The vaporised precursors are then transported *via* a carrier gas to a heated substrate. The gaseous precursors then undergo a heterogeneous reaction, depositing as a solid thin film. While the precursor molecules are being transported to the substrate, they experience various forces due to their motion, which can be described by fluid dynamics.

1.3.1 *Fluid Dynamics*

There are two types of flow regime to describe the movement of a fluid. The first is a laminar flow regime, whereby the fluid flows in a "ribbon-like" fashion. The second is a turbulent flow regime, whereby localised vortices increase lateral mixing of the fluid.

The movement of the precursor molecules/particles/droplets in the reactor can be described by the dimensionless parameters known as the Knudsen number (Kn), and the Reynolds number ($\mathrm{R_e}$).[87,88]

1.3.1.1 *Knudsen number*

The Knudsen number is the ratio between the mean free path of a molecule, and the characteristic length of the reactor, such as the diameter of the tube.[89] It is given by the following equation:

$$\mathrm{Kn} = \frac{\lambda}{\mathrm{L}} = \frac{\mathrm{kT}}{\sqrt{2}\pi \mathrm{d}^2 \mathrm{PL}} \tag{1.11}$$

where λ is the mean free path of a gas molecule, or the average distance travelled by a molecule before it collides with another mollecule, L is the characteristic length of the reactor, k is the Boltzmann constant (1.381 $\times$ 10^{-23} J·K^{-1}),[90] T is the temperature, d is the molecular diameter, and P is the total pressure.[91]

When $\lambda << \mathrm{L}$, or $\mathrm{Kn} << 0.01$, a significant amount of intermolecular collisions occur, and hence the gas behaves like a viscous fluid. This is known as the continuum regime, and is the flow type found when CVD is performed at atmospheric pressure.

When $\lambda >> \mathrm{L}$, or $\mathrm{Kn} >> 10$, the intermolecular collisions are negligible in comparison to the collisions between the molecules and the walls of the reactor. This is known as the free molecular regime, and is the flow type found when CVD is performed at reduced pressures.

When $\lambda \sim \mathrm{L}$, or $10 < \mathrm{Kn} < 0.01$, there is an intermediate transition regime, in which it is difficult to establish a theoretical model.[88,91]

1.3.1.2 *Reynolds number*

The Reynolds number is given by the following equation:

$$\mathrm{R_e} = \frac{\rho \mathrm{v} \mathrm{L}}{\mu} \tag{1.12}$$

where ρ is the density of the fluid, v is the mean fluid velocity, L is the characteristic linear dimension (usually the distance travelled by the fluid), and μ is the fluid viscosity.

The physical implication of the Reynold's number is the ratio between the inertial forces (ρv) and the viscous forces (μ/L).[91] Thus, it emphases the relative importance of these types of forces present in a fluid, and hence the Reynold's number describes which flow regime a fluid is in. For a low value of R_e (<100), there will be a laminar flow. This is ideal for CVD, as it results in more uniform coverage on the substrate. For a high value of R_e (>2100), there will be turbulent flow. For this regime, there will be vortices, which will result in a non-uniform deposition and hence a turbulent flow is unfavourable for CVD. In between these two regimes is the intermediate regime, which has characteristics from both laminar and turbulent flow.[86]

1.3.1.3 *Boundary layer*

A laminar flow regime involves the formation of a static boundary layer at the substrate surface.[92] The boundary layer is defined as a thin fluid film that forms on solid surfaces due to drag forces such as friction. Within the boundary layer, the velocity of the fluid is considered to be zero.

The thickness of the boundary layer is defined as the distance from the wall to the point within the fluid layer at which the flow velocity is 99% of the free stream velocity.[91] Using the Reynolds number, the boundary thickness is estimated with the following equation:

$$\delta = \frac{L}{\sqrt{R_e}} \tag{1.13}$$

In the case of CVD, the boundary layer forms on the walls of the reactor and on the substrate surface. In order to reach the substrate

surface, molecules must first diffuse through the barrier layer *via* random Brownian motion. This diffusion is usually affected by the temperature of the substrate.

1.3.1.4 *Thermophoresis*

As CVD is regularly done in a 'cold-wall' reactor, there is usually a temperature gradient, whereby the temperature decreases with increasing distance from the substrate. Upon entering the temperature gradient, precursor molecules/particles will be repelled from the hot surface of the substrate. This is because they experience thermophoresis, also known as the Soret effect or thermodiffusion, where they are bombarded by high energy gas molecules near the heated surface.[93–95] Whilst the particles still collide with the lower-energy gas molecules that originate from the colder end of the temperature gradient, these collisions are with gas molecules that have less momentum relative to those originating from near the heat source, and therefore there is a net thermophoretic force pushing the particles down the temperature gradient, away from the substrate.

The particles' response to the thermophoretic force is determined by their thermal conductivity, k, relative to the thermal conductivity of the fluid that they are within.[96] With a larger thermal conductivity, energy received from the hot side of a conducting particle will be more efficiently transferred to the cold side. This effectively 'warms' the relatively cold gas molecules, thus minimising the local temperature gradient, and hence decreases the effect of thermophoresis (Figure 1.7).

The other factor which affects the particles' response to the thermophoretic force is the particle diameter. Larger particles have more area in which they can be bombarded by gas molecules. Hence, large particles will be repelled more strongly from a hot surface

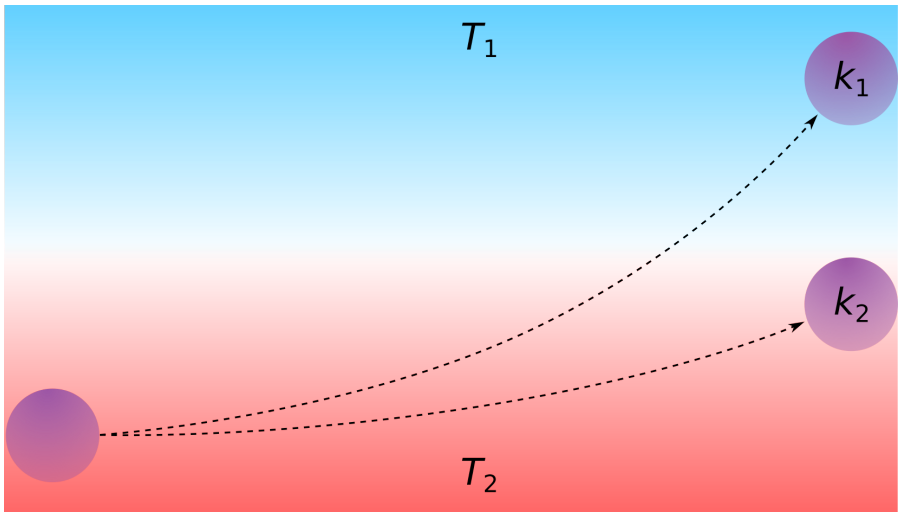

Figure 1.7: A particle experiencing the thermophorectic force in a temperature gradient, where $T_1 < T_2$, and $k_1 < k_2$.

than smaller particles.[95] This can be beneficial in CVD, as the large solid particles formed by an unwanted homogeneous reaction in the gas phase can be repelled from the film, thus maintaining film uniformity and homogeneity. As small particles are less affected by thermophoresis, a large majority of the gaseous precursor molecules which enter a CVD reactor will be able to diffuse to the heated substrate, where they can react and deposit a film.

1.3.2 *Thermodynamics*

As CVD involves chemical reactions, it is important to discuss the energetics of the reaction to aid in the understanding of the driving forces for the process. Thermodynamics describes the feasibility of a reaction by considering the relative energetic states of the system before and after the reaction occurs. A reaction is considered to be thermodynamically viable if the overall change in Gibb's free energy for the reaction (ΔG_r) is negative, i.e. the products are in a more

stable state than the reactants. The molar Gibb's free energy (G) at a pressure P is given by:

$$G = G° + RT \ln P \tag{1.14}$$

where $G°$ is the Gibb's free energy at 1 atm pressure, R is the gas constant (8.314 $J \cdot mol^{-1} \cdot K^{-1}$),[90] and T is the temperature.

However, the molar free energy of a pure gas is equal to its chemical potential:

$$G = \mu \tag{1.15}$$

where μ is the chemical potential at pressure P. Thus, Equation 1.14 can be written as:

$$\mu = \mu° + RT \ln P \tag{1.16}$$

where $\mu°$ is the chemical potential at 1 atm pressure.[97]

Consider a typical CVD deposition between two gaseous precursors (A + B), resulting in a solid film (C) and a gaseous by-product (D):

$$A_{gas} + B_{gas} \rightarrow C_{solid} + D_{gas} \tag{1.17}$$

The initial molar free energy is given by:

$$G^i_m = X^i_A \mu^i_A + X^i_B \mu^i_B + X^i_C \mu^i_C + X^i_D \mu^i_D \tag{1.18}$$

where X_n^i is the initial molar fraction of species n, and μ_n^i is the initial chemical potential of species n. However, in the initial state, C and D are not present, hence $X_C^i = X_D^i = 0$. Therefore, Equation 1.19 can be simplified to:

$$G_m^i = X_A^i \mu_A^i + X_B^i \mu_B^i \tag{1.19}$$

As the reaction proceeds, X_A^i and X_B^i will decrease and X_C^i and X_D^i will increase. At equilibrium, assuming that not all of the reactants react to form the products, the final molar free energy is given by:

$$G_m^f = X_A^f \mu_A^f + X_B^f \mu_B^f + X_C^f \mu_C^f + X_D^f \mu_D^f \tag{1.20}$$

where X_n^f is the final molar fraction of species n, and μ_n^f is the final chemical potential of species n. The overall change in Gibb's free energy is given by the following equation:

$$\Delta G_r = G_m^f - G_m^i \tag{1.21}$$

If ΔG_r is negative, the products are stable with respect to the reactants, making the reaction thermodynamically viable. Equation 1.21 can also be written as follows:

$$\Delta G_r = \sum \Delta G_f(\text{products}) - \sum \Delta G_f(\text{reactants}) \tag{1.22}$$

where $\Delta G_f(\text{products})$ is the free energy of formation of the products, and $\Delta G_f(\text{reactants})$ is the free energy of formation of the reactants. Note that the free energy of formation is not constant,

but depends on variables such as temperature, pressure, types of reactant, and molar ratios of reactants.[98]

The chemical potential of C increases from $\mu_C^i = -\infty$ to μ_C^f, which is the chemical potential of the solid at equilibrium. This is a destabilisation of C, since a species with a more negative chemical potential has a higher thermodynamic stability.[99] For the reaction to proceed and for deposition to occur, the chemical potential of C in the gas phase should be higher than the chemical potential of C in the solid phase. Therefore, considering only the initial state and the final state, the driving force is for etching, rather than deposition.

In order for the reaction to occur, the partial pressure of C in the gas phase (P_C^{gas}) should be higher than the equilibrium vapour pressure of C in the solid phase ($P_C^{v.p.}$).[97,100]

This is described by the supersaturation ratio α, given by the following equation:

$$\alpha = \frac{P_C^{gas}}{P_C^{v.p.}} \tag{1.23}$$

When $\alpha < 1$, etching is thermodynamically favourable. When $\alpha > 1$, deposition is thermodynamically favourable. When $\alpha = 1$, neither net etching nor net deposition will occur.

In summary, deposition will only become energetically viable when the reaction proceeds to a significant degree, so that the partial pressure of gaseous C becomes relatively high, making it metastable or supersaturated with respect to solid C.

However, even if a reaction is thermodynamically viable, and has a large negative change in Gibb's free energy, it may still happen at such a slow rate that it is not observed. While thermodynamics explains which state a system prefers to be in, kinetics explains the rate at which a system will change from one state into another.[92]

1.3.3 *Kinetics*

CVD is a complicated, non-equilibrium process, which involves homogenous gas-phase reactions, heterogenous reactions upon the substrate and film surface, and adsorption and desorption of various reactants and products. The film growth rates are a factor of several variables, including substrate temperature, reactor pressure, and types and concentrations of precursors.[101] Since there are so many factors to consider, CVD processes can be difficult to reproduce in different laboratories with subtle changes in reactor setups and deposition parameters.[102] Consequently, the kinetics of a CVD system can be challenging to measure.[89] However, reasonable assumptions can be made to sufficiently model the kinetics of CVD. Despite the many concurrent reactions, the slowest will determine the overall growth rate of the film. Depending on the substrate temperature, three growth rate regimes are possible.

At low temperatures, the process is limited by the kinetics of the surface chemical reactions. The relatively low energy supplied to the molecules will mean that the reactions will occur slowly. In this regime, the growth rates increase exponentially with temperature, according to the Arrhenius relationship:

$$\text{Growth rate} \propto \exp(-\mathrm{E_A}/\mathrm{RT}) \tag{1.24}$$

where $\mathrm{E_A}$ is the activation energy of the reaction.

At high temperatures, the process is limited by the rate at which diffusion can occur through the boundary layer. The higher temperatures means that the molecules can react faster, so the limitation is the rate at which fresh reactant molecules can be

supplied to the growing film. This is determined by Fick's first law of diffusion:

$$F = -D\frac{dC}{dx} \tag{1.25}$$

where F is the flux across a plane perpendicular to the direction of diffusion, x is the distance, D is the diffusivity, and C is the concentration of the diffusing species. In this regime, the growth rates are less dependant on temperature.

At very high temperatures, the growth rates decrease again due to a simultaneous increase in the rate of etching of the films. The high temperatures also cause a depletion in the reactants due to gaseous homogenous side-reactions, resulting in particulate formation. These particles experience a higher thermophoretic force and hence are less likely to reach the surface and react. The different growth regimes are plotted in Figure 1.8.[86,101,103,104] Typically, CVD is performed in the mass transport limited regime.

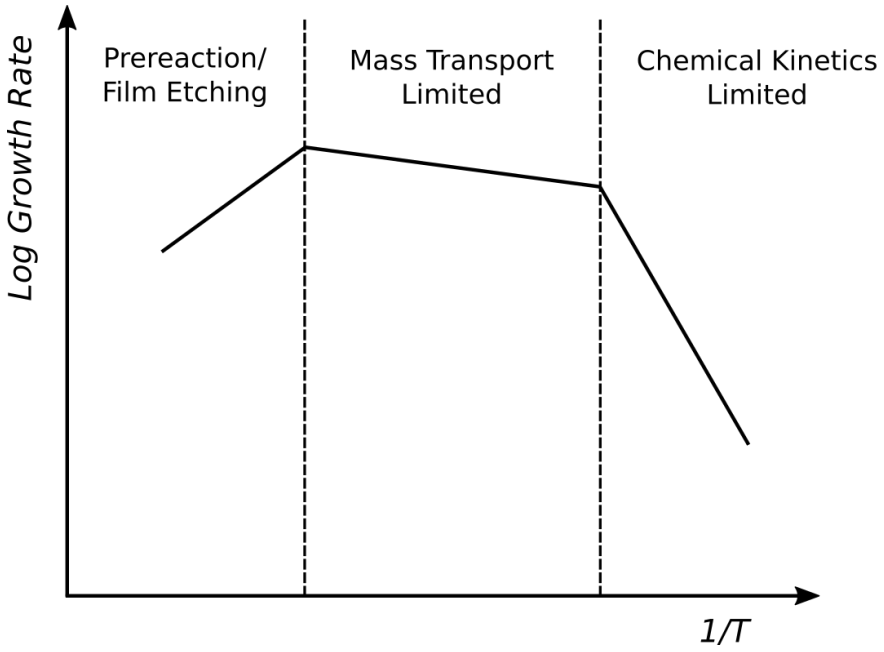

Figure 1.8: Film growth rate regimes at different temperatures.

The pressure of the system also has a large impact on the kinetics. From relatively high atmospheric pressure down to intermediate pressures (i.e., when Kn is small), gas phase reactions are prevalent. Additionally, the boundary layer is present and thick enough to present a significant obstacle for incoming reactant molecules.

At lower pressures, gas phase collisions decrease in frequency, and gas phase reactions become less significant. At very low pressures, mass transport is no longer significant. Instead, growth rates are controlled mainly by the temperature and the kinetics of the chemical reactions. Therefore, the reaction is mass transport limited for atmospheric pressure CVD, and chemical kinetics limited for low pressure CVD.[86,101]

1.3.4 *Deposition Mechanism and Film Growth*

Upon contacting the heated surface of the substrate, precursor molecules will undergo a heterogeneous reaction, whereby they thermally decompose and adsorb to the substrate, as depicted in Figure 1.9.

The heated substrate provides the adsorbed precursor atoms with energy, allowing them to rearrange *via* surface diffusion. Thus, the atoms can find the lowest energy vacant sites upon the surface. The resultant film growth can usually be categorised as either epitaxial growth, polycrystalline growth, or amorphous growth.

Epitaxial growth occurs upon the surfaces of single crystals, and is when the atoms coat the entire substrate surface in a single monolayer before forming subsequent layers (Figure 1.10a). The lowest energy site an incoming atom can find upon a single crystal substrate will be one that continues the substrate's crystal strucutre. Hence, the film will grow with the same crystal structure as the

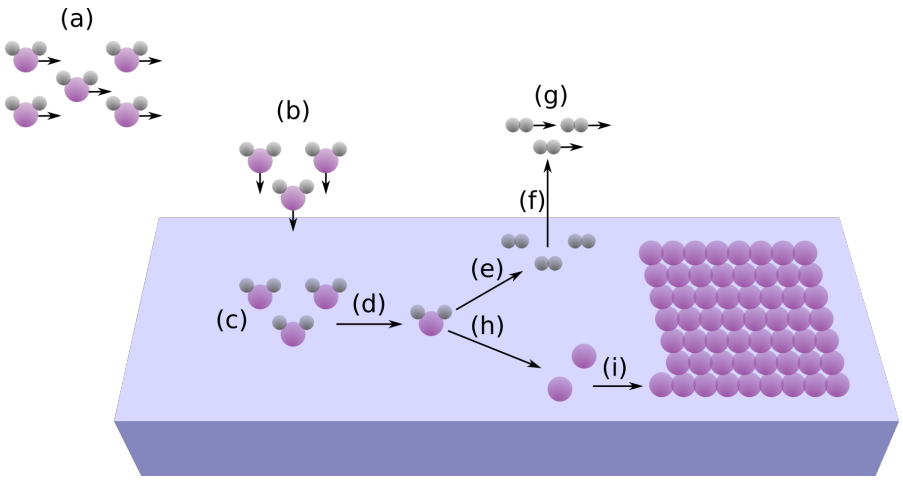

Figure 1.9: The heterogeneous CVD-type deposition and growth of a thin film, illustrating: (a) arrival of precursor molecules, transported by the carrier gas, (b) diffusion of precursor molecules to the substrate surface, (c) adsorption of precursor molecules to the substrate surface, (d) surface diffusion of precursor molecules, (e) thermal degradation of precursor molecules and surface diffusion of by-products, (f) desorption of by-products, (g) removal of by-products, transported by the carrier gas, (h) thermal degradation of precursor molecules and surface diffusion of the film component atoms or ions, (i) aggregation and film formation.

substrate. In order for this to occur, lattice mismatch between the substrate and the film must be minimised. In other words, the unit cells must have similar dimensions. A high lattice mismatch will result in strain and the formation of defects such as dislocations, which reduces the stability and the adhesion of the film. Epitaxial growth is aided by high temperatures and low growth rates, which allow the atoms time to arrange in a layer-by-layer fashion.[105]

Polycrystalline growth is enabled by the formation of 'islands' which grow independently at various nucleation points (Figure 1.10b). These islands coalesce to form a polycrystalline film. In this case, the crystal structure of the film is not strongly dependent on the substrate. This type of growth can occur upon substrates which are either polycrystalline or amorphous. Polycrystalline growth can also occur upon a single crystal substrate, when there is a severe lattice mismatch, leading to a high concentration of defects.[92] Furthermore,

island growth can occur if the incoming atoms interact more strongly with the other atoms in the film than they do with the atoms of the substrate.

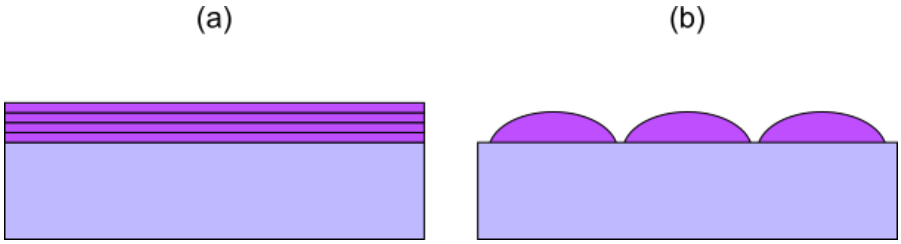

Figure 1.10: A comparison of (a) epitaxial and (b) polycrystalline film growth.

Amorphous growth occurs at low temperatures and high growth rates, which inhibit surface diffusion and prevent the growth of a crystalline film. Annleaing amorphous films can lead to the formation of crystal phases.[101]

The type of growth affects the film morphology, and therefore it must be controlled to obtain the desired properties in the resultant film.

1.3.5 *Variations of Chemical Vapour Deposition*

Many variations of CVD have been reported in the literature, each with its own advantages. However, there will also be limitations which must be taken into consideration when selecting a method for a deposition. When the same material is deposited using different techniques, the quality of the films may differ substantially.[38] Some of the most common variations of CVD are:

- Atmospheric pressure CVD (APCVD), which involves the evaporation of volatile precursors. The gaseous precursors are then transported to a heated substrate *via* a carrier gas at atmospheric pressure (101325 Pa) in order to deposit a film. APCVD is considered the conventional form of CVD.

- Low pressure CVD (LPCVD), in which CVD is done at reduced pressures. This pressure gradient increases the rate at which the precursors flow through the reaction chamber, and hence it improves the uniformity of the film and the coverage across the substrate.

- Ultrahigh vacuum CVD (UHVCVD), in which CVD is done at very low pressures, typically $<10^{-6}$ Pa. The ultrahigh vacuum tends to minimise impurities in the film.

- Plasma enhanced CVD (PECVD), in which high energy electrons generated within a plasma are used to enhance the CVD process, and allow kinetic barriers to be overcome at more ambient temperatures.

- Flame assisted CVD (FACVD), which involves the combustion of liquid or gaseous precursors prior to deposition, to enhance the deposition rates.

- Atomic layer deposition (ALD), in which alternating monolayers of two or more elements are deposited sequentially on a substrate, allowing good control over the growth process.

- Aerosol assisted CVD (AACVD), in which a solution containing the precursors is prepared, from which an aerosol mist is generated, before being transported to the substrate as in APCVD. AACVD is the technique used for this research, and it is described more thoroughly in the next section.

1.4 AEROSOL ASSISTED CHEMICAL VAPOUR DEPOSITION

AACVD involves the generation of an aerosol mist from a precursor solution, which is then transported to the heated substrate *via* a

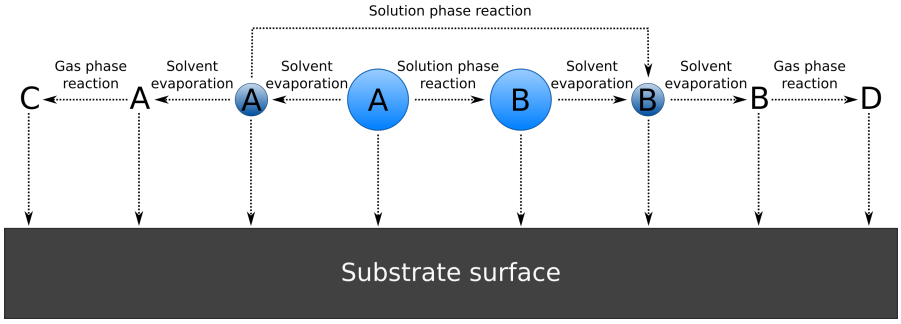

Figure 1.11: How an aerosol droplet can behave as it approches a hot surface (ignoring the thermophoretic force depicted in Figure 1.7). 'A' represents the initial film precursor, and 'B', 'C', and 'D', are all products of reactions occurring prior to deposition. After the evaporation of the solvent, deposition of the gaseous precursor will occur as shown in Figure 1.9

carrier gas. This further complicates the kinetics of AACVD, since there are several possibilities for the aerosol droplets as they approach the heated substrate surface, as shown in Figure 1.11.

The simplest case is where the solvent completely evaporates from the droplet, leaving the precursor molecules in the gas phase to adsorb to the surface as in conventional CVD. Slightly more complicated is the possibility of incomplete evaporation, whereby some of the solvent remains at the surface, resulting in the droplet impacting the surface directly. This is usually the case for the related deposition technique, spray pyrolysis, where the aerosol droplets are sprayed directly at the surface, usually at a higher velocity than in AACVD. During a spray pyrolysis deposition, there is not enough time for the droplet to evaporate completely prior to impacting the heated substrate. Generally, in AACVD, the solvent is passed more gently over the heated substrate, and is expected to evaporate before reaching the surface. Furthermore, there remains the possibility of a homogeneous solution-phase reaction between the precursors in the droplets, or a homogeneous gas phase reaction between the precursors prior to the heterogeneous deposition. In reality, it is

statistically probable that there is a combination of all of these processes occurring near the surface.

1.4.1 *Aerosol Generation*

There are three main methods used for the generation of an aerosol, also known as aerosolisation, or atomisation: electrostatic atomisation, ultrasonic aerosol generation, and pneumatic aerosol jet.[106]

Electrostatic atomisation involves applying an electric current to a spray nozzle. The electrostatic charges on the surface of the liquid result in the fragmentation of the liquid into droplets, which are carried away by a gas stream.

Ultrasonic aerosol generation is the most commonly used aerosol generation technique for laboratory AACVD processes, and is the method used for the majority of the depositions described in this thesis. A piezoelectric transducer is placed beneath the liquid. Following this, a high-frequency electric field is applied to the transducer, which causes it to produce ultrasonic vibrations. These waves pass through the liquid and form droplets at the surface.[107]

A pneumatic aerosol jet is generated by drawing the liquid into a small area, where it collides with a high-velocity stream of compressed gas, forming a fine mist of droplets. Since this method uses high-velocity flow rates, the generated aerosol can be sprayed rapidly, resulting in fast mass transport rates. For this reason, this aerosol generation technique was used for the scale-up depositions described in Section 6.4.2.

1.4.2 *Droplet Evaporation*

For an uncharged droplet, the change in the diameter, d, of the droplet over a time, t, is determined by the following equation:

$$d^2 = d_o^2 - 8t\frac{C_A D}{C_p}\ln\left[\frac{1 - x_{A\infty}}{1 - x_{As}}\right] \tag{1.26}$$

where d_o is the initial droplet diameter at time $t = 0$, C_A is the molar concentration of species A in the vapour phase, C_p is the molar conncetration of species A in the liquid phase, D is the binary diffusivity of vapour A in gas B, $x_{A\infty}$ is the mole fraction of species A far from the droplet, and x_{As} is the mole fraction of species A at the droplet surface.[106,108]

Additionally, the droplet diameter can be used to estimate the characteristic time for the droplets to evaporate, using the following equation:

$$\tau_{sat} = \frac{1}{2\pi d D_v N_\infty} \tag{1.27}$$

where τ_{sat} is the characteristic time to saturate a gas with the vapour from evaporating droplets, D_v is the diffusivity of the vapour, and N_∞ is the number of droplets per unit volume.[106]

According to Equation 1.27, the time required to saturate a gas is inversely proportional to the size and concentration of the droplets. Large droplets, or a high concentration of droplets will result in saturation of the gas before the droplets are able to fully evaporate. For this reason, smaller droplets are preferable.[106]

If the droplet is charged, the charge density on the surface will increase as the droplet shrinks. This will continue until the Rayleigh

limit is reached. At this point, the repulsive electrostatic force will overcome the attractive surface tension, and the droplet will fragment into smaller droplets. This continues until the droplet fully evaporates.[109] Therefore, charged droplets will evaporate faster than uncharged droplets.

1.4.3 *Advantages and Disadvantages*

The AACVD method has several important advantages over APCVD. First and foremost, AACVD eliminates the requirement for the precursors to be highly volatile. This is because AACVD precursors simply need to be soluble in a suitable solvent from which an aerosol mist can be generated. For this reason, AACVD opens up a wide range of non-volatile precursors which can be used for a CVD-type deposition.

Secondly, the AACVD reactor setup has a simpler design in comparison to APCVD. In order to transport the precursors to the reactor, the precursor solution is nebulized, rather than heated. Additionally, the piping does not need to be heated in order to prevent condensation. Depositions can also be performed in a open atmosphere. For these reasons, depositions can be performed at relatively low cost.[110]

Another advantage is that the surface morphology of the as-deposited films can be controlled, by varying the deposition conditions, such as substrate, precursor, deposition temperature, and solvent used for the precursor solution.[111] This can allow for simple tuning of morphology-related properties, such as conductivity and absorbance.

Additionally, AACVD is usually performed using a single source, in which the precursors undergo a significant amount of molecular

mixing in solution, prior to the deposition. This allows for easy control of stoichiometry during the synthesis of multicomponent materials.[86]

However, despite the benefits of AACVD, there are drawbacks which have prevented its implementation as an industrial deposition technique. Firstly, the film growth rates are typically low (*ca.* 10s of nm min^{-1}).[112] AACVD depositions can take 10s of minutes, which is unsuitable for large-scale depositions, which would generally need to occur within approximately 20 seconds. Another limitation of AACVD is that large quantities of solvent would be used for large-scale depositions, which is an additional hazard in an industrial environment. For this reason, powerful vapour extraction and solvent recycling systems would need to be implemented alongside the deposition apparatus.

The numerous advantages of AACVD make it a desirable technique to be potentially used for industrial-scale thin film depositions, as long as the limitations can be overcome.

1.5 PROJECT AIMS

There are two aims to the research presented in this thesis. The first is the discovery of alternative, sustainable TCO materials. This will be achieved *via* AACVD of inexpensive precursors — in particular, zinc-based materials, due to the low cost and low toxicity of zinc. The films will be fully characterised and optimised to achieve the best possible properties.

The second aim is the scale-up of AACVD. The advantages of this technique make it attractive for commercial applications, and hence the feasibility of scale-up will be investigated by examining the

transportation of the aerosol prior to deposition, and by attempting to increase the film growth rates.

2

EXPERIMENTAL AND CHARACTERISATION METHODS

2.1 INTRODUCTION

This chapter will summarise how AACVD is used to deposit thin film coatings. Additionally, the theory behind any analysis techniques is discussed. This is done to aid in the understanding of any data obtained whilst characterising the films.

All chemicals used for the work described in this thesis were used as bought, without any further purification.

2.2 AEROSOL ASSISTED CHEMICAL VAPOUR DEPOSITION

The typical set up for an AACVD deposition is shown in Figure 2.1.

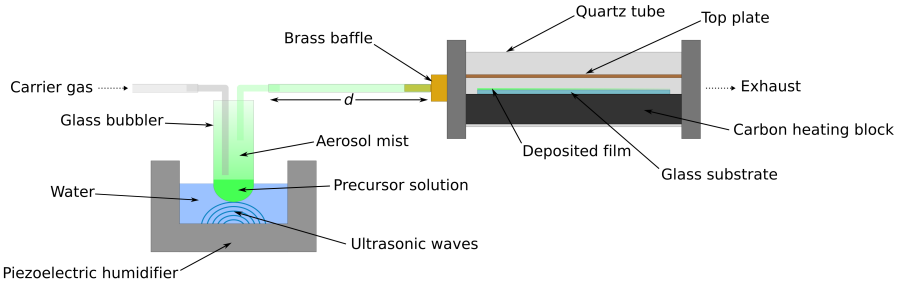

Figure 2.1: Experimental set up of a laboratory scale AACVD deposition.

The substrates used for depositions were 3.2 mm thick float glass plates, precoated with a 50 nm silicon dioide [SiO_2] barrier layer, supplied by Pilkington NSG. The barrier layer was necessary to prevent the migration of ions between the film and the substrate at high temperatures, which can cause a deterioration of the electrical

properties.[113,114] The glass was cut to an area of 10 x 4.5 cm^2. Prior to the deposition, a substrate would first be cleaned in a base bath consisting of KOH (500 g) dissolved in H_2O (1 L) and isopropyl alcohol (IPA) (6 L). After this, the substrate was cleaned using soap and water, acetone, and IPA. When the substrate was clean, it was loaded into the reactor, upon a carbon heating block.

A brass top plate was suspended approximately 8 mm above the glass substrate, lying parallel to maintain laminar flow of the aerosol. This allowed for the deposition of a more continuous, uniform film.

When the substrate and top plate were loaded, the reactor was sealed, and the graphite block was then heated to the deposition temperature.

A precursor solution was prepared by adding all precursors to an appropriate solvent within a glass bubbler, and stirring using a magnetic follower. When all solids were fully dissolved, the bubbler was clamped so that it was partially submerged in a 'Liquifog' piezo ultrasonic atomizer from Johnson Matthey, which uses an operating frequency of 1.6 MHz. The humidifier was then switched on to generate an aerosol mist of the precursor solution within the bubbler.

A carrier gas was used to transport the aerosol mist to the reactor at a gas flow rate of 1 L min^{-1}, through a brass baffle which initiates a laminar flow, to the heated substrate where the film deposited. All exhaust was vented into a fume cupboard.

After approximately 30–40 minutes, when the bubbler was completely empty, the humidifier was switched off, and the reactor was allowed to cool to below 100 °C, under a continuous flow of the carrier gas. When the reactor was cool enough, the substrate was removed for further analysis and characterisation.

Table 2.1: Deposition conditions for all of the films described in this thesis, which were successfully deposited *via* AACVD.

Film	Deposition Temperature /°C	Precursors
AZO	450	$Zn(acac)_2$ + $AlCl_3$
GZO	450	$Zn(acac)_2$ + $GaCl_3$
IZO	450	$Zn(acac)_2$ + $InCl_3$
AGZO	450	$Zn(acac)_2$ + $AlCl_3$ + $GaCl_3$
IGZO	450	$Zn(acac)_2$ + $GaCl_3$ + $InCl_3$
AIZO	450	$Zn(acac)_2$ + $AlCl_3$ + $InCl_3$
SZO	450	$Zn(acac)_2$ + $Si(OC_2H_5)_4$
FSZO	450	$Zn(acac)_2$ + NH_4F + $Si(OC_2H_5)_4$
FTO	550	$^nBuSnCl_3$ + NH_4F

2.3 CHARACTERISATION TECHNIQUES

Considering the fact that macroscopic properties are often determined by a material's structure on the local, nanoscopic, and microscopic scale, it is crucial to thoroughly analyse a material using appropriate techniques, to understand the origin of its functional properties.

2.3.1 *X-Ray Diffraction*

Chemically identical materials can exist as different crystal structures. A common example of this is the photocatalytically active material titanium dioxide [TiO_2], which has several naturally occurring forms. The two most common of these are rutile and anatase. Although they are both built from TiO_2, the unit cells have different coordination structures and thus different chemical bonding which results in highly dissimilar ionization potentials and electron affinities.[115] These varying electronic structures are what cause the discrepancy in

the photoactivity of the two otherwise chemically indistinguishable phases.[116,117] This shows how a variation in the crystal structure can affect the macroscopic properties of the material.

The crystal structure of a material can be ascertained using X-ray diffraction (XRD) techniques.

2.3.1.1 *Miller planes*

The crystal structure of a material is determined by its long range order on the atomic level, whereby an effectively infinite repetition of the unit cell in three dimensions results in periodic atomic planes known as Miller planes.[118]

Families of Miller planes are designated by the Miller indices, h, k, and l, which are integers that correspond to the lattice parameters a, b, and c, respectively. For cubic crystal structures with lattice parameter a, the interplanar spacing for a particular Miller plane (hkl) is given by:

$$d_{hkl} = \frac{a}{\sqrt{h^2 + k^2 + l^2}} \tag{2.1}$$

By scanning through different angles with respect to the incident radiation, various Miller planes in a crystal structure will cause diffraction. Different Miller planes will be present for different crystal structures, which leads to a "fingerprint" XRD pattern for each crystal structure.

2.3.1.2 *Bragg's law*

The interplanar distance, d_{hkl}, is on the order of 10^{-10} m, which corresponds to the wavelength of X-ray radiation.[119] For this reason, X-rays are used to probe the crystal structure of a material. When a beam of X-rays is directed onto a surface at an angle θ, the

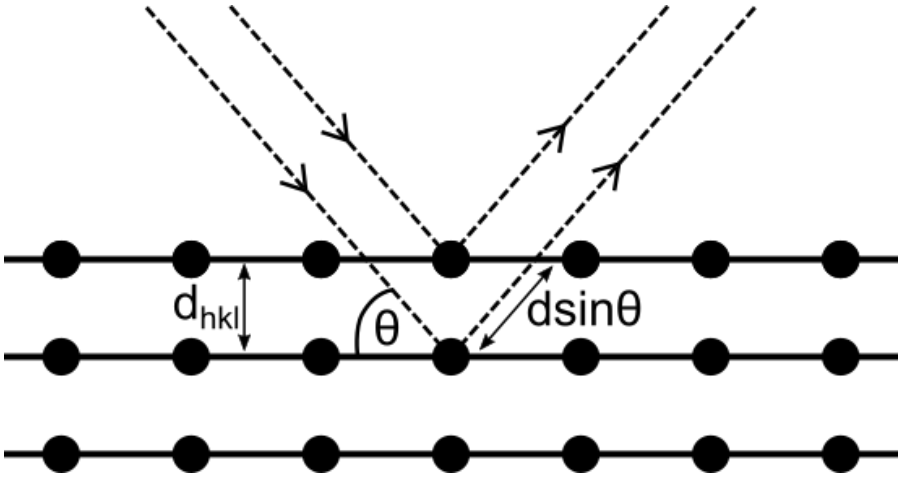

Figure 2.2: Schematic showing the origin of Bragg's law. The lower X-ray photon has travelled an additional distance of $2d_{hkl}\sin\theta$ in comparison to the upper photon.

photons are scattered by the electron clouds of the atoms. At certain angles, constructive interference between reflected photons originating from different crystal planes will result in a high intensity peak. This occurs when the Bragg equation is satisfied:

$$n\lambda = 2d_{hkl}\sin\theta \tag{2.2}$$

where n is the order of the reflection (usually set to 1), and λ is the wavelength of the incident photon. The origin of Bragg's law is summarised in Figure 2.2.

2.3.1.3 *Crystallite diameter*

In a polycrystalline material such as the films described in this thesis, the crystal quality can be quantified by examining the crystallite diameter. Larger crystallite growth typically indicates higher quality crystallinity. The crystallite diameter can be determined from the

broadening of the peaks in an XRD pattern, using the Scherrer equation:

$$D = \frac{k\lambda}{\beta \cos\theta} \tag{2.3}$$

where D is the crystallite diameter, k is the Scherrer constant, $lambda$ is the wavelength of the incident X-rays, β is the full-width at half maximum (FWHM) in radians, and θ is the Bragg diffraction angle in radians.[120–122]

2.3.1.4 *Equipment*

XRD patterns were recorded using a Bruker D8 Discover X-ray diffractometer using monochromatic Cu $K\alpha_1$ and $K\alpha_2$ radiation of wavelengths 1.54056 and 1.54439 Å respectively, emitted in an intensity ratio of 2:1 with a voltage of 40 kV and a current of 40 mA. The incident beam angle was in a grazing set up at 1° and data was collected between 10° and 66° 2θ with a step size of 0.05° at 2 seconds per step. Lattice parameters were calculated from the XRD data using GSAS and EXPGUI software.[123,124]

2.3.2 *X-Ray Photoelectron Spectroscopy*

The elemental composition of a solid sample can be determined by irradiating the surface with X-rays of a known energy to liberate electrons from the surface. These electrons are then detected and measured in counts per second (CPS). Their kinetic energy is determined, from which the binding energy can be calculated. This is known as X-ray photoelectron spectroscopy (XPS).

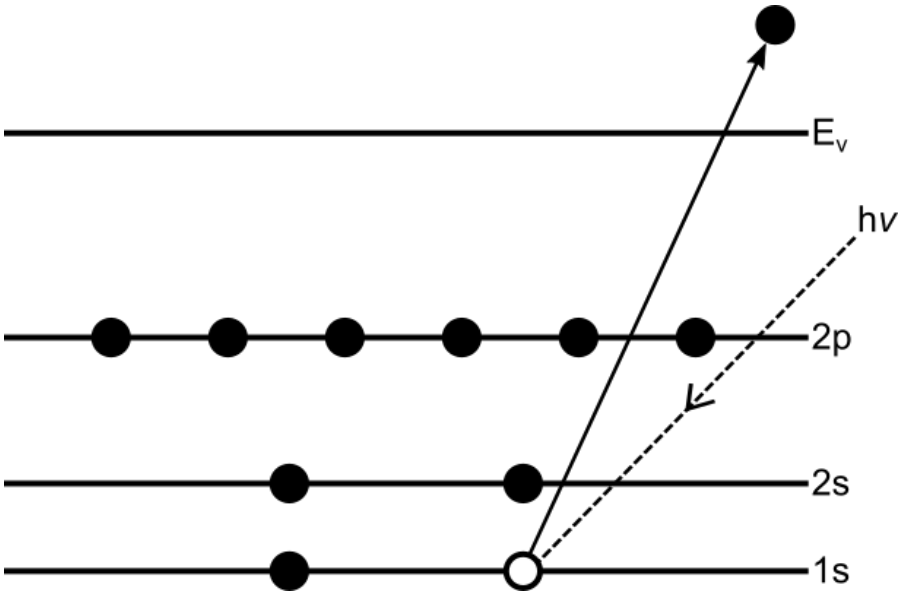

Figure 2.3: Schematic representation of X-ray photoelectron spectroscopy. The incident X-ray photon excites a core electron past the vacuum level (E_V), thus liberating it from the nucleus it is bound to.

2.3.2.1 *Binding Energy*

Since the energy of the irradiating X-rays is known, the kinetic energy of the emitted electrons is related to the binding energy of the electron to the atom or ion it is bound to. The binding energy of an electron depends on the element of the atom it is bound to, the oxidation state of that atom, and its environment, taking into account any local bonding. The binding energy is given by:

$$\mathrm{BE} = \mathrm{h}\nu - \mathrm{KE} - \phi \tag{2.4}$$

where BE is the binding energy, h is Plank's constant, ν is the wavelength of the incident X-rays, KE is the kinetic energy of the emitted electrons, and ϕ is the work function of the electrons.

Since the X-rays interact with the electron clouds of the elements, heavier elements are more sensitive to XPS than lighter elements. For this reason, relative sensitivity factors are used to scale the peaks,

allowing them to be used to accurately quantify the elements in the sample.

XPS is a surface technique, which means it can only probe the uppermost few nanometres. This is because the liberated electrons from deeper within the bulk of the sample will be re-absorbed before they can be detected. In order to obtain data from the bulk of the material, the sample can be etched, by bombarding it with an ion beam.

2.3.2.2 *Equipment*

XPS was done using a Thermo Scientic K-alpha spectrometer with mono-chromated $K\alpha$ radiation, a dual beam charge compensation system and constant pass energy of 50 eV, with a spot size of 400 μm. Data was fitted using CasaXPS software.

2.3.3 *Scanning Electron Microscopy*

High resolution images of a surface morphology can be obtained through scanning electron microscopy (SEM), with much greater magnification and resolution than is possible using optical microscopy. It is achieved by focusing a beam of high energy electrons onto the surface of a sample. These electrons can undergo elastic or inelastic collisions with the sample. Elastic collisions are where they collide with the nucleus of an atom and are backscattered without a significant transfer of energy. Backscattered electrons typically have energy values from 50 eV to the operating energy of the electron beam. Inelastic collisions are where the electrons from the beam collide with the sample nuclei or sample electrons and transfer some of their kinetic energy to the sample. This transfer of energy can result in the ejection of secondary

electrons from the surface. The secondary electrons typically have energy values of 0–50 eV. Since secondary electrons are low energy in comparison to backscattered electrons, they can be directed towards the detector using a positively charged grid.

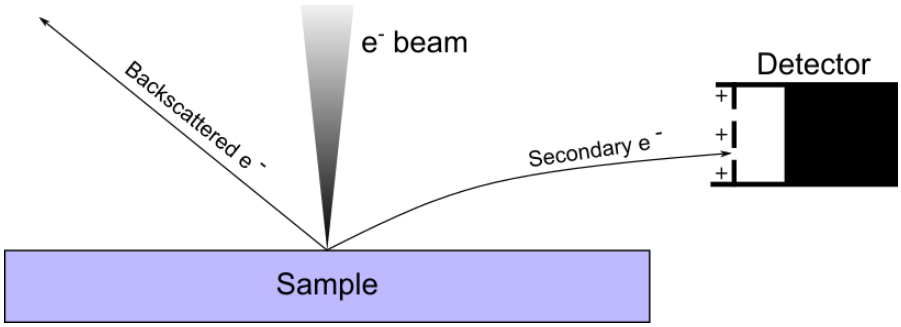

Figure 2.4: Schematic representation of scanning electron microscopy.

The number of secondary electrons is related to the topography of the sample. As the beam position is known, the resulting image is a distribution map, with each pixel corresponding to the intensity of the signal of the detected secondary electrons. The surface morphology of a film can vary substantially, depending on its composition, and on deposition conditions.

2.3.3.1 *Equipment*

Samples were sputtered with gold for 30 seconds to improve their conductivity. This was done to prevent sample charging, which can have a detrimental effect on the quality of the images recorded. The surface morphologies were analysed by viewing the films from a top-down perspective, and the film thicknesses were determined by viewing the films from a side-on perspective. Ideally, the thickness measurements should be calibrated by measuring against a standard of a known thickness.

SEM images were obtained using a JEOL JSM-6301F Field Emission SEM at an acceleration voltage of 5 kV.

2.3.4 *UV/Vis Spectroscopy*

UV/Vis spectroscopy is a technique that analyses the optical properties of a sample. This is done by shining visible, ultraviolet (UV), and near infrared (NIR) light at the sample, scanning through a range of wavelengths.

When light passes from one medium to one with a different refractive index, some of the light is scattered. The reflectivity (R) represents the fraction of the incident light which is scattered, and is given by:

$$\mathrm{R} = \frac{\mathrm{I_R}}{\mathrm{I_o}} \tag{2.5}$$

where $\mathrm{I_R}$ is the intensity of the reflected light, and $\mathrm{I_o}$ is the intensity of the incident light.[125]

The light that enters the new medium without being reflected can be absorbed. The amount of light that is absorbed is dependant upon the spacing between energy levels in the sample. If these spacings correspond to the incident light wavelength, then this wavelength will be absorbed, resulting in the promotion of an electron.[126]

Alternatively, light can be transmitted through the medium. The transmitted intensity ($\mathrm{I_T}$) is given by:

$$\mathrm{I_T} = \mathrm{I_o}(1 - \mathrm{R})^2 \mathrm{e}^{-\beta \mathrm{l}} \tag{2.6}$$

where $\mathrm{I_T}$ is the intensity of the transmitted light, β is the absorption coefficient, and l is the sample thickness.[125]

The overall intensity of the incident beam (I_o) is related to the intensity of the light that is transmitted (I_T), absorbed (I_A), or reflected (I_R) from the sample:

$$I_o = I_T + I_A + I_R \tag{2.7}$$

For TCO applications, it is important to analyse transmittance in the visible part of the spectrum in particular. This range is approximately 400-700 nm.[127]

2.3.4.1 *Equipment*

UV/Vis spectra were taken using a Perkin Elmer Fourier Transform Lambda 950 UV/Vis spectrometer over a range of 250–2500 nm, in both transmission and reflectance modes.

2.3.5 *Electrical Conductivity Measurements*

As explained in Section 1.2.1, band theory can be used as a model to explain the intricacies behind electrical conductivity. In classical terms, delocalised electrons or holes, both of which can be regarded as point charges, respond to an externally applied electric field, resulting in a net flow of charge.

2.3.5.1 *Hall Effect*

If a magnetic field is applied perpendicular to the direction of the current, the electron flux will experience a force known as the Lorentz force. This deflects electrons, and causes them to build up against one side of the conductor. This phenomenon is known as the Hall effect.[128] The result of this is a potential difference, known as the Hall voltage, perpendicular to the direction of the current (see Figure 2.5).

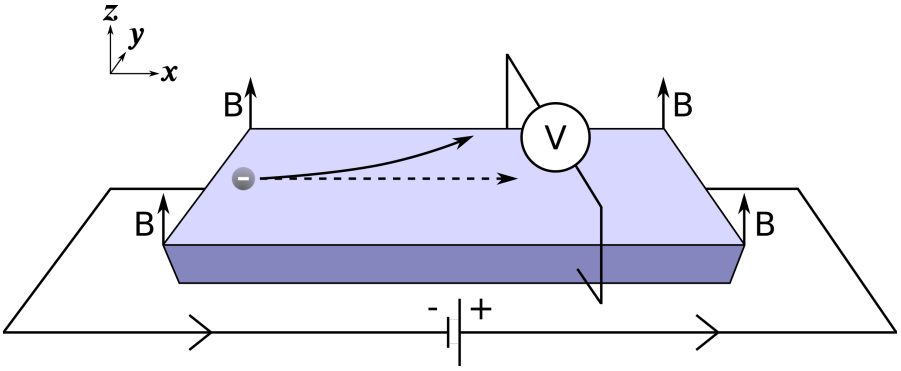

Figure 2.5: Schematic showing an electron responding the the Lorentz force, resulting in the Hall effect.

The Hall effect can be probed to determine the electrical properties of a semiconductor. The Hall coefficient, R_H, is given by:

$$R_H = \frac{E_y}{j_x B_z} \tag{2.8}$$

where E_y is the magnitude of the electric field in the *y* direction, induced due to the Hall voltage. This induced electric field is perpendicular to the current density j_x, which is defined as the electric current in the *x* direction, per unit of cross section. B_z is the magnitude of the applied magnetic field in the *z* direction.[6]

The Hall coefficient can be related to the quantity of charge carriers by the following equation:

$$R_H = -\frac{r_H}{Ne} \tag{2.9}$$

where r_H is the Hall coefficient scattering factor, N is the charge carrier concentration, and e is the charge on an electron. r_H is assumed to be unity,[104] and so Equation 2.9 can be simplified to:

$$R_H = -\frac{1}{Ne} \tag{2.10}$$

The sign of the Hall voltage determines the type of semiconductor (*n*-type or *p*-type).[92] However, it is important that the sample is homogeneous, as non-uniformity can falsely indicate a *p*-type Hall coefficient for a sample that is evidently an *n*-type semiconductor.[129]

The magnitude of the Hall voltage is proportional to the resistivity, ρ, and the charge carrier mobility, μ, as shown by the following equation:

$$R_H = \rho\mu \tag{2.11}$$

2.3.5.2 *Van der Pauw Technique*

The method by which the Hall effect is measured is known as the van der Pauw technique.[130] This method involves measuring the current through the sample. Following this, the current is measured whilst applying a perpendicular magnetic field of a known strength. Finally, the current is measured again with the magnetic field in the opposite direction. This technique exploits the Hall effect and can be used to calculate the resistivity, the charge carrier concentration, the charge carrier mobility, and the doping type (*n*-type or *p*-type).

The advantage of the van der Pauw technique is that it can accurately determine the electrical properties of a sample of any arbitrary shape, as long as the sample is two dimensional (i.e. its thickness is significantly less than its width), there are no holes in the sample, and the contacts are placed at the perimeter.

2.3.5.3 *Equipment*

Samples were cut to 1 cm^2 squares, and then a small amount of silver paint was applied to each corner to create contacts. An Ecopia HMS-3000 was used to obtain the Hall measurements, *via* the van der

Pauw technique. Measurements were taken using a 0.58 T permanent magnet, and a current of 1 μA.

Part II

RESULTS AND DISCUSSION

3

ALUMINIUM-, GALLIUM- AND INDIUM-DOPED ZINC OXIDE THIN FILMS DEPOSITED *VIA* AACVD

This chapter focuses on the effect that the group 13 elements (aluminium, gallium and indium) have when doped into thin films of zinc oxide. The films were deposited *via* AACVD, with the dopant concentrations varied in order to find the optimum optoelectronic properties. The films were first doped individually with aluminium, gallium or indium, with varying dopant concentrations to optimise the functional properties. Following this, the films were co-doped, whereby two dopants were used simultaneously. Finally, a solvent study was performed to determine the extent of control over surface morphology.

3.1 INTRODUCTION

ZnO has potential as an alternative TCO material. It can be made at a low cost due to the high abundance of naturally occurring zinc-containing minerals, and it has a relatively low toxicity compared to indium and tin. Additionally, it has a wide, direct band gap, resulting in high optical transparency. Undoped ZnO usually has low conductivity, granted by the presence of inherent defects, as described in Section 1.2.5. However, there are many dopants for ZnO which are known to improve its electrical properties. The most commonly investigated dopants for ZnO are the group 13 metals — in particular, aluminium, gallium and indium.

Aluminium-doped zinc oxide (AZO), gallium-doped zinc oxide (GZO), and indium-doped zinc oxide (IZO) have all been synthesised previously by various techniques, including magnetron sputtering,[131–143] molecular beam epitaxy,[144–146] pulsed laser deposition,[71,147–154] sol-gel synthesis,[155–161] atomic layer deposition,[162–168] spray pyrolysis,[15,169–175] atmospheric pressure chemical vapour deposition,[176–181] low pressure chemical vapour deposition,[182–185] and aerosol assisted chemical vapour deposition.[186–193]

Various precursors have been used in the literature for the deposition of ZnO thin films. Two of the most commonly used precursors are dimethyl zinc [$ZnMe_2$] and diethyl zinc [$ZnEt_2$]. These compounds have been used to prepare high quality ZnO films with excellent TCO properties.[168,178,179,190,194] However, these precursors are expensive and highly pyrophoric.[191] This makes their usage dangerous and non-trivial, which is not ideal for commercial applications.

The zinc precursor used in this work was zinc acetylacetonate [$Zn(acac)_2$]. This compound is relatively inexpensive, air-stable and non-toxic. However, depositions using $Zn(acac)_2$ are more likely to result in carbon contamination in the films.[185]

3.2 DOPANT STUDY

3.2.1 *Experimental*

The equipment for AACVD was set up as described in Section 2.2. The glass substrate was heated to 450 °C.

A typical precursor solution was made by dissolving zinc acetylacetonate monohydrate [$Zn(acac)_2{\cdot}H_2O$] (0.5 g)

in methanol [MeOH] (20 mL), with a dopant quantity of aluminium/gallium/indium trichloride [Al/Ga/$InCl_3$]. Acetic acid (20 drops) was added to aid the solubility of the $Zn(acac)_2$ in MeOH. Nitrogen [N_2] was used as the carrier gas, with a flow rate of 1 L min^{-1}. An undoped ZnO film was also deposited to compare the effects of the dopants.

3.2.2 *Film Synthesis*

Aluminium-, gallium-, and indium-doped ZnO thin films were synthesised, based on the following reactions:

$$Zn(acac)_{2\,(g)} + xAlCl_{3\,(g)} \xrightarrow{\Delta} Al_xZn_{1-x}O_{(s)}$$
$$Zn(acac)_{2\,(g)} + xGaCl_{3\,(g)} \xrightarrow{\Delta} Ga_xZn_{1-x}O_{(s)}$$
$$Zn(acac)_{2\,(g)} + xInCl_{3\,(g)} \xrightarrow{\Delta} In_xZn_{1-x}O_{(s)}$$

Each deposition was repeated at least three times. No significant difference was observed between depositions, indicating the deposition of each film was reproducible. The films were handled and stored in air and showed no degradation in quality or properties after 12 months. All of the as-deposited films were of high quality, and showed good adhesion to the glass substrates. The films passed the Scotch tape test, and resisted being scratched with a steel scalpel.

The films displayed interference patterns when observed at an angle. These patterns are the result of constructive and destructive interference between visible photons which have been reflected from the air-film boundary and the film-substrate boundary.[10,190] This indicated that the films had a non-uniform thickness, with some regions of the films being similar to the wavelength of light.[195,196] This is to be expected, as a result of the side-on deposition method. The film will be thicker nearest to the baffle. The region

closest to the baffle consistently showed the highest quality films in terms of coverage and uniformity, so this was the region that was characterised. The film thicknesses were determined by side-on SEM. They varied and did not show a significant trend. The average film thickness was 1.8 μm. (Table 3.1).

3.2.3 *Crystal Structure*

All of the as-deposited films displayed a wurtzite ZnO crystal structure. No secondary phases corresponding to Al_2O_3, Ga_2O_3, In_2O_3, or any ternary Zn-M-O (M = Al, Ga, In) compound were observed by XRD (Table 3.1).

Table 3.1: Structural properties of AZO, GZO, and IZO films deposited *via* AACVD. The film thicknesses were determined by side-on SEM, and have an error of ± 0.1 μm.

Film	Crystallite diameter /nm	Preferred orientation	Unit cell volume /Å^3	Film thickness /μm
5 mol% AZO	76	(002)	47.673(5)	1.0
10 mol% AZO	72	(002)	47.649(8)	1.2
15 mol% AZO	62	(002)	47.620(8)	2.0
20 mol% AZO	64	(002)	47.69(1)	1.0
5 mol% GZO	73	(002)	47.65(7)	3.8
10 mol% GZO	69	(002)	47.573(3)	2.0
15 mol% GZO	61	(002)	47.473(8)	1.9
20 mol% GZO	63	(002)	47.520(8)	2.2
5 mol% IZO	47	(100), (101)	48.015(6)	0.8
10 mol% IZO	52	(100), (101)	47.544(6)	2.0
15 mol% IZO	48	(100), (101)	47.811(9)	2.4
20 mol% IZO	45	(100), (101)	47.578(9)	1.5

Figure 3.1 shows the XRD patterns for the AZO films, compared to an undoped ZnO film deposited in the same conditions, as well as a powder ZnO sample taken from ICSD #82028.

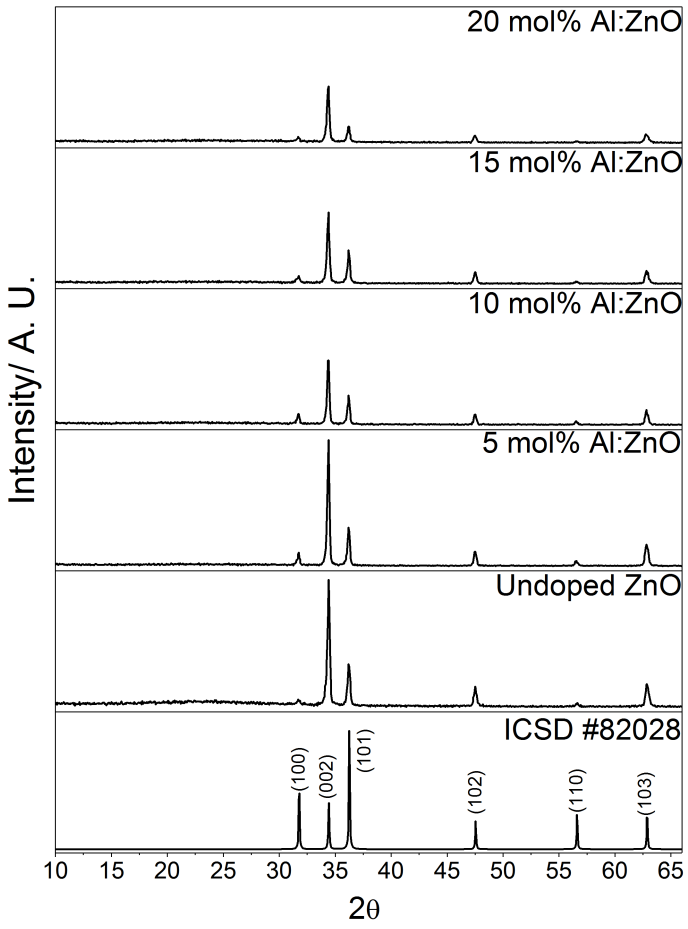

Figure 3.1: X-ray diffraction patterns of the AZO films deposited *via* AACVD. An undoped ZnO film also deposited *via* AACVD is included for reference, as well as a diffraction pattern of ZnO from ICSD #82028.

In a thin film, preferred orientation is often observed in the XRD data. This is because films grow to minimise their surface energy, and hence there will be preferential growth in the crystal plane with the lowest surface free energy. In wurtzite ZnO, the (002) plane is the most stable.[190,192,197] For this reason, preferrential growth in the (002) is commonly reported for ZnO thin films.[189] The stability of the (002) plane often results in columnar grain growth, due to

the packing of crystallites along the *c*-axis, perpendicular to the substrate surface.[187,198]

The undoped ZnO film showed a preferred orientation in the (002) plane, as is typical with ZnO films. The incorporation of aluminium did not affect the preferred orientation, and the AZO films continued to display a prominent (002) peak.

The intensity of the peaks decreased as the concentration of aluminium was increased in solution. This could be due to the aluminium causing a degradation in the crystallinity of the ZnO, resulting in less intense X-ray reflections. This is also demonstrated in the decreasing crystallite diameters, which are attributed to crystal quality in polycrystalline materials. This is to be expected, since the ionic radius of 4 co-ordinate Al^{3+} (0.53 Å) is smaller than the ionic radius of 4 co-ordinate Zn^{2+} (0.74 Å).s[199–201] Hence, substitutional doping of Al^{3+} onto the Zn^{2+} sites will lead to a small amount of strain within the unit cell, which can result in crystallographic defects such as dislocations, self-interstitials, or point defects.

The XRD patterns of the GZO films were very similar to those of the AZO films (Figure 3.2). They showed a preferred orientation in the (002) crystal plane, even at high dopant concentrations. They also showed a reduction in peak intensity and crystallite diameter at higher dopant concentrations, indicating a degradation in the crystal quality. Compared to the rest of the group 13 metals, the ionic radius of 4 co-ordinate Ga^{3+} (0.62 Å) is closest to that of 4 co-ordinate Zn^{2+} (0.74 Å).[154] This means that gallium should have have the smallest effect on the crystallinity of the ZnO. However, the observed loss of peak intensity was almost identical for both AZO and GZO.

The XRD patterns of the IZO films did not show preferred orientation in the (002) direction like the AZO and GZO films (Figure 3.3). Instead, the use of indium as a dopant seemed to promote

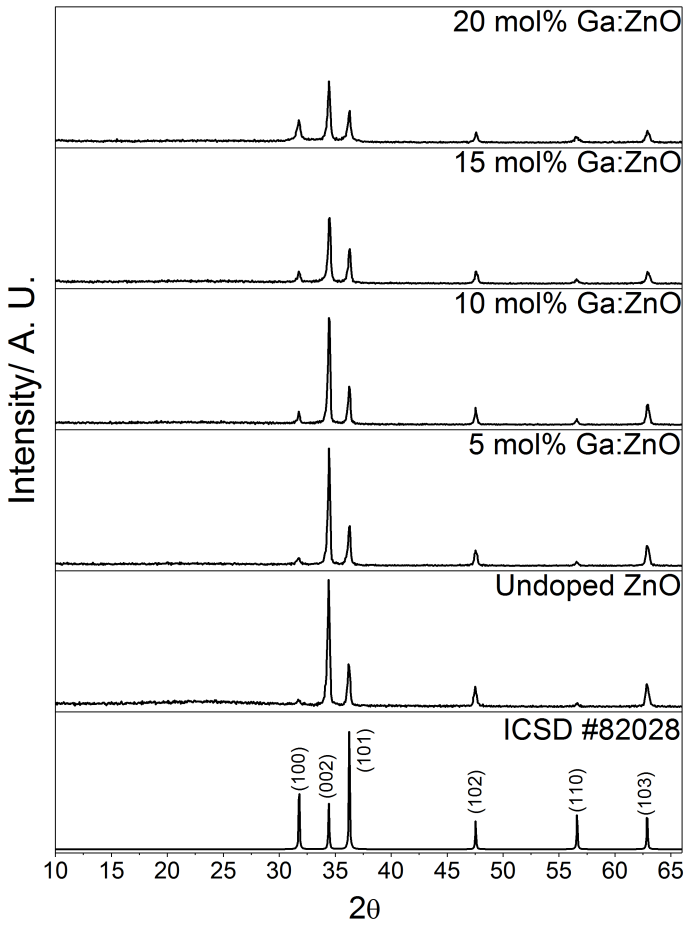

Figure 3.2: X-ray diffraction patterns of the GZO films deposited *via* AACVD. An undoped ZnO film also deposited *via* AACVD is included for reference, as well as a diffraction pattern of ZnO from ICSD #82028.

growth in the (100) and (101) planes. This phenomenon has been observed many times in IZO films grown by spray pyrolysis — a technique closely related to AACVD.[169,170,173,175,202–204] Goyal *et al.* explained that the change in preferred orientation observed in IZO films is due to the In^{3+} cations providing a different type of nucleation centre for ZnO gowth.[204]

The IZO films also showed a reduction in peak intensity as the dopant concentration was increased. Again, this indicated a loss of

crystallinity. However, the loss of crystallinity was more extreme in the case of IZO in comparison to AZO and GZO. The IZO diffraction peaks were even less intense at high dopant concentrations, and the crystallite diameters were significantly smaller. When 20 mol% indium was used in the precursor solution, the resultant film showed significant peak broadening, and a complete loss of intensity of the (002), (102), and (103) peaks. The reason that indium had a more detrimental effect on the ZnO crystal structure compared to aluminium and gallium is that 4 co-ordinate In^{3+} has an ionic radius (0.81 Å) larger than that of 4 co-ordinate Zn^{2+} (0.74 Å).[205–207] Moreover, the In–O bond length (2.10 Å) is longer than the Zn–O bond length (1.97 Å).[207] Consequently, the substitution of Zn^{2+} for In^{3+} will introduce more strain into the lattice, resulting in an increase in the disorder in the structure.

The incorporation of the dopants into the ZnO structure can be confirmed by calculating the unit cell volumes. This was done by refining the XRD data to determine the lattice parameters. The two main ways to do this are Rietveld refinement and Le Bail refinement. The Rietveld method begins with an idealised model of a known structure. It then changes the model by refining various parameters through a least squares refinement, until the simulated XRD pattern closely matches the observed pattern.[208,209] The Le Bail method does not start with a model structure. Instead, the peak intensities are initially fit arbitrarily.[210] Because the peak intensities are not refined as they are in Rietveld refinement, the calculations are much faster. The Le Bail method is better for crystalline thin film samples which show unusual peak intensities due to the effects of preferred orientation. Consequently, the Le Bail method was used for all of the refinement in this work. More detail about XRD refinement is presented in the appendix (Section A.1)

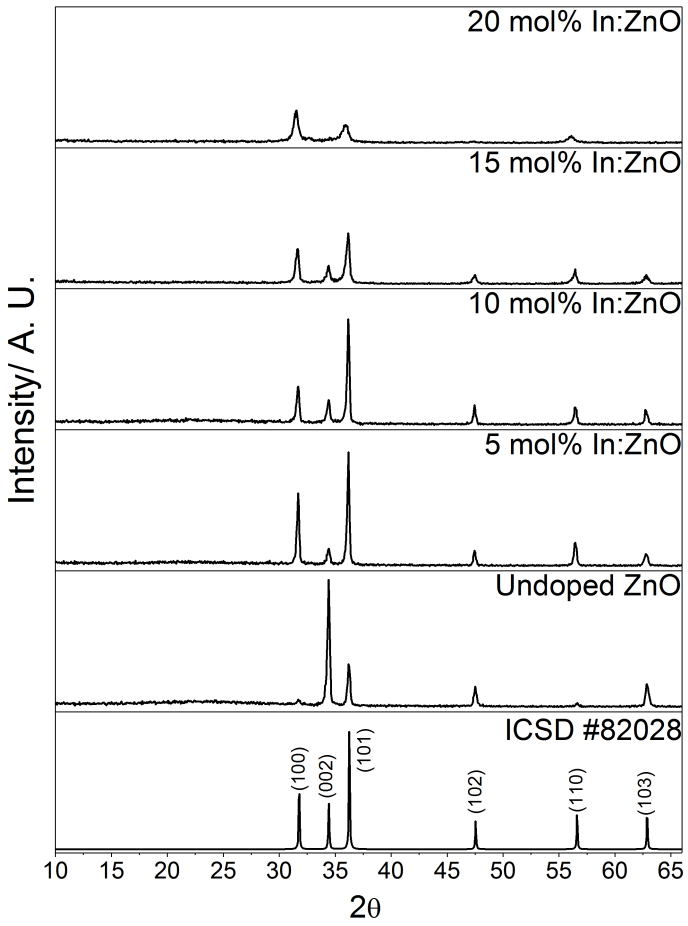

Figure 3.3: X-ray diffraction patterns of the IZO films deposited *via* AACVD. An undoped ZnO film also deposited *via* AACVD is included for reference, as well as a diffraction pattern of ZnO from ICSD #82028.

The general trend observed for the AZO and the GZO films was an initial decrease in unit cell volume (Table 3.1). This is because the dopants initially subsititute for Zn^{2+}. Since the dopants have smaller ionic radii in comparison to Zn^{2+}, the result is a contraction in the unit cell. However, at higher dopant concentrations, there was an eventual increase in unit cell volume again. The reason for this is that, at high concentrations, the dopants began to occupy interstitial sites as well as substitutional sites.[211] The IZO films showed less of a trend,

due to the larger ionic radius of In^{3+}. Interestingly, the 5 mol% IZO film had the largest unit cell volume out of any of the as-deposited films. Higher concentrations of indium appeared to result in a slightly smaller unit cell volume. This could be explained by the indium introducing more disorder into the crystal structure than aluminium and gallium, and hence the extracted unit cell volumes for the IZO films were less reliable due to the poorer quality XRD data obtained.

3.2.4 *Elemental Analysis*

The elemental compositions of the films were determined using XPS. The films were etched, so that the compositions of the surfaces and the bulks of the films could be determined. Carbon was observed both at the surfaces and within the bulks of the films, indicating carbon contamination. This was due to the thermal breakdown of $Zn(acac)_2$ — a process which is less efficient than the decomposition of other organozinc precursors such as $ZnMe_2$ and $ZnEt_2$. Hence, carbon species were trapped during film growth. Adventitious carbon was used to calibrate the data, with a binding energy of 285.0 eV for the carbon 1s peaks.[212,213]

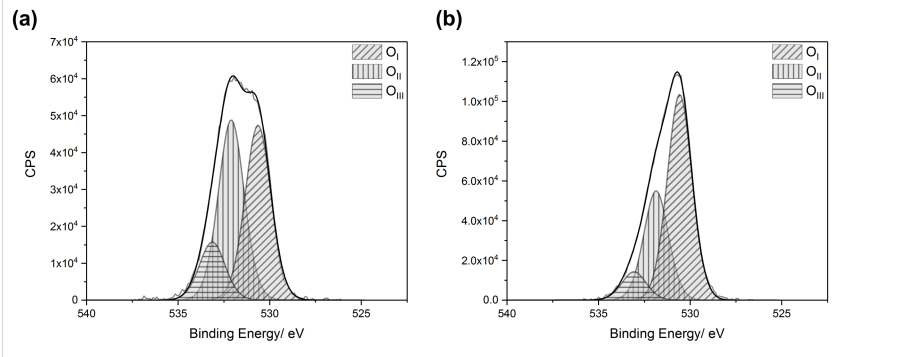

Figure 3.4: XPS spectra for the 10 mol% AZO film deposited *via* AACVD, showing typical oxygen 2p peaks (a) at the film surface, and (b) in the bulk of the film.

All of the 2p and 3d peaks scanned were deconvoluted using CasaXPS, to find that they each consisted of two separate peaks. The peak splitting is a result of spin-orbit coupling, whereby the spin of an electron interacts with the magnetic field generated by its motion.[214–217] This causes the 2p orbital to split into a $2p_{1/2}$ orbital and a $2p_{3/2}$ orbital. The $2p_{1/2}$ orbital is lower in energy than the $2p_{3/2}$ orbital, so more energy is required to liberate an electron from the $2p_{1/2}$ orbital. Hence, the $2p_{1/2}$ peak is at a higher binding energy than the $2p_{3/2}$ peak in the XPS spectrum. Similarly, the 3d orbital is split into a lower energy $3d_{3/2}$ orbital and a higher energy $3d_{5/2}$ orbital. The 2p orbitals were examined for zinc, oxygen and aluminium. Since gallium and indium are larger than aluminium, the 2p orbitals are more shielded than the 3d orbitals. Thus, it is easier to liberate an electron from the gallium or indium 3d orbitals than it is from the 2p orbitals. For this reason, these orbitals were probed using XPS.

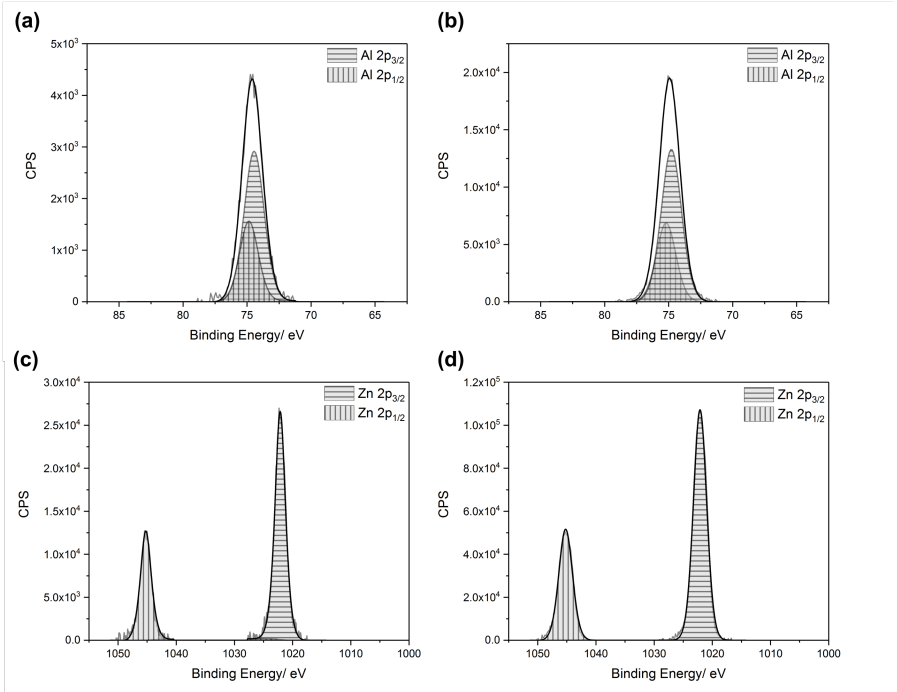

Figure 3.5: XPS spectra for the 10 mol% AZO film deposited *via* AACVD, showing the (a) aluminium 2p peaks at the film surface, (b) aluminium 2p peaks in the bulk of the film, (c) zinc 2p peaks at the film surface, and (d) zinc 2p peaks in the bulk of the film.

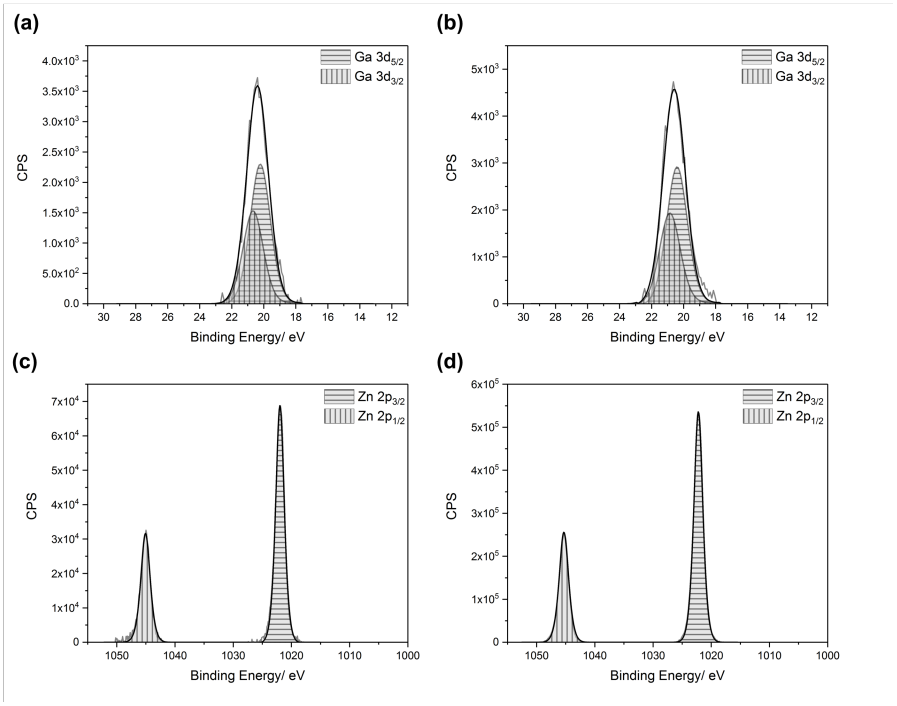

Figure 3.6: XPS spectra for the 10 mol% GZO film deposited *via* AACVD, showing the (a) gallium 3d peaks at the film surface, (b) gallium 3d peaks in the bulk of the film, (c) zinc 2p peaks at the film surface, and (d) zinc 2p peaks in the bulk of the film.

The oxygen 2p peak for the films could be deconvoluted into three separate peaks, O_I, O_{II}, and O_{III}, with binding energies of 530.0 eV (± 0.2 eV), 531.6 eV (± 0.2 eV), and 532.6 eV (± 0.2 eV), respectively (Figure 3.4). The O_I peak, which was the most intense, can be attributed to the O^{2-} ions in ZnO.[154] The O_{II} peak can be attributed to O^{2-} ions located in oxygen deficient regions in ZnO, and thus relates to the concentration of oxygen vacancies.[154,182,218–220] The O_{III} peak can be attributed to surface bound oxygen species, such as O_2^-, $-CO_3$, and H_2O.[199,204] In the bulks of the films, the relative intensities of the O_{II} and O_{III} peaks diminished significantly. This indicates that surface bound impurities were mostly removed during the etching process. It also suggests that the concentration of oxygen vacancies in the bulks of the film was lower than at the surfaces. Wong *et al.* observed that there was a higher concentration of oxygen vacancies at the surfaces of their ZnO nanowires, deposited *via* CVD.[221] They explained this by calculating

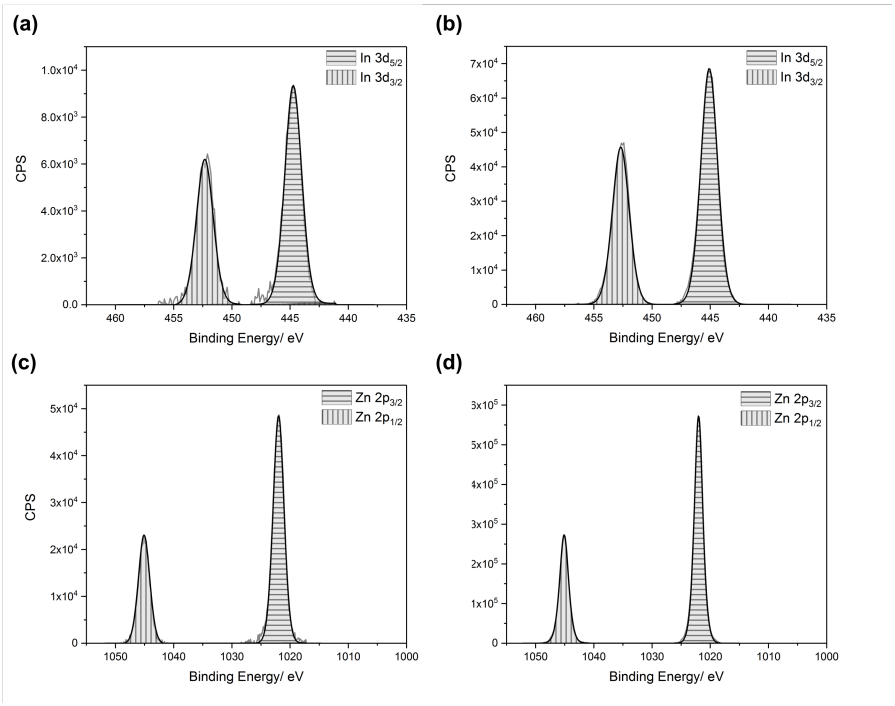

Figure 3.7: XPS spectra for the 10 mol% IZO film deposited *via* AACVD, showing the (a) indium 3d peaks at the film surface, (b) indium 3d peaks in the bulk of the film, (c) zinc 2p peaks at the film surface, and (d) zinc 2p peaks in the bulk of the film.

that the V_O formation energy is lower near the surface than it is in the bulk. This was confirmed by Deng *et al.*, who also found that V_O migration in ZnO is energetically favourable in the direction from the bulk to the surface.[222] V_O defects migrate *via* a kick-out process, whereby a nearest neighbour O^{2-} ion jumps into the V_O site, leaving a vacancy behind.[70,223] Carrasco *et al.* stated that there is a low diffusion barrier for V_O defects in ZnO.[224]

The zinc 2p peaks consistently had a splitting of 23.1 eV, and peak positions of 1021.3 eV ($\pm$ 0.2 eV) and 1044.4 eV ($\pm$ 0.2 eV) for the $2p_{3/2}$ and $2p_{1/2}$, respectively (Figures 3.5c, 3.5d, 3.6c, 3.6d, 3.7c, and 3.7d). All of this corresponds to Zn^{2+} in ZnO.[189,199] This is further evidence that no Zn-M-O phases formed.

The aluminium 2p peaks had a splitting of 0.41 eV, which is typical of aluminium.[225–227] The position of the aluminum $2p_{3/2}$ and $2p_{1/2}$ peaks were consistently found at binding energies of 75.1 eV ($\pm$ 0.2 eV) and

75.5 eV (± 0.2 eV), respectively, which can be assigned to Al^{3+} (Figure 3.5a and 3.5b).[201] The characteristic peak for metallic aluminium at 72.8 eV was not observed at the surfaces or within the bulks of the films.[228,229]

The gallium 3d peaks all had a splitting of 0.45 eV, which is the splitting that is usually seen for this peak (Figures 3.6a and 3.6b).[230–232] In addition, the gallium $3d_{5/2}$ and $3d_{3/2}$ peak positions were consistently 20.0 eV (± 0.2 eV) and 20.4 eV (± 0.2 eV) respectively, which is typical of Ga^{3+}.[233,234] The characteristic peak for metallic gallum at 18.7 eV was not observed at the surfaces or within the bulks of the films.[235,236]

Finally, the indium 3d peaks had a splitting of 7.6 eV. This is typical for indium 3d (Figures 3.7a and 3.7b).[237,238] The position of the indium $3d_{5/2}$ and $3d_{3/2}$ peaks were consistently 444.9 eV (± 0.2 eV) and 452.5 eV (± 0.2 eV), respectively, which is what is usually observed for In^{3+}.[239,240] The characteristic peak of metallic indium at 444.0 eV was not observed at the surfaces or within the bulks of the films.[241,242]

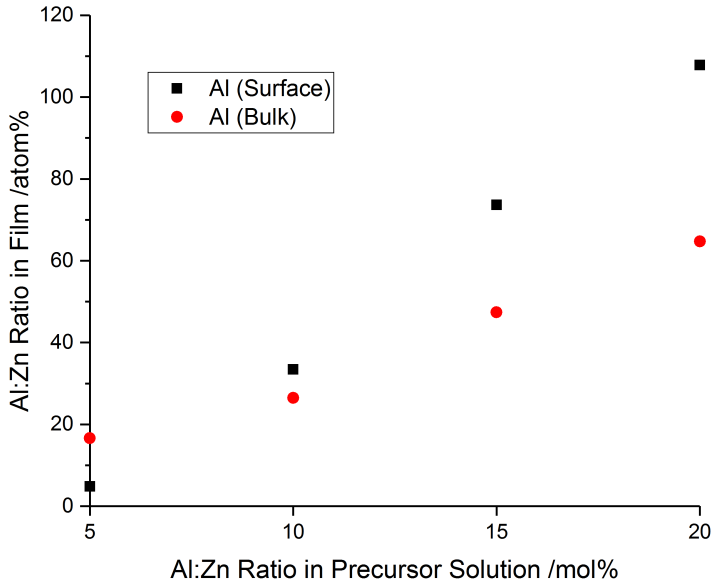

Figure 3.8: Al:Zn ratios at the surfaces and in the bulks of the AZO films deposited *via* AACVD, as determined by XPS.

The concentration of Al^{3+} incorporated into the films was higher than the concentration in the initial precursor solution (Figure 3.8). This indicates that the amount of Al^{3+} in the film was strongly dependant on the amount in solution. Increasing the concentration of aluminium in solution led to an increase in surface segregation of the dopant. This is a phenomenon which has been observed previously, and is due to the dopant segregating to the grain boundaries, and forming oxide bonds.[159] It is the result of the dopant reaching its solubility limit in the film.[173,243] There is a significant amount of surface segregation for high aluminium concentrations. This is due to the small ionic radius of Al^{3+}. The high deposition temperatures provided the Al^{3+} with sufficient energy to diffuse through the lattice.[167,244] Usually, dopant segregation increases at high dopant concentrations.[199] The oxide phases that form in the grain boundaries are insulating, and typically lead to a deterioration in the electrical properties of the film.[201,245]

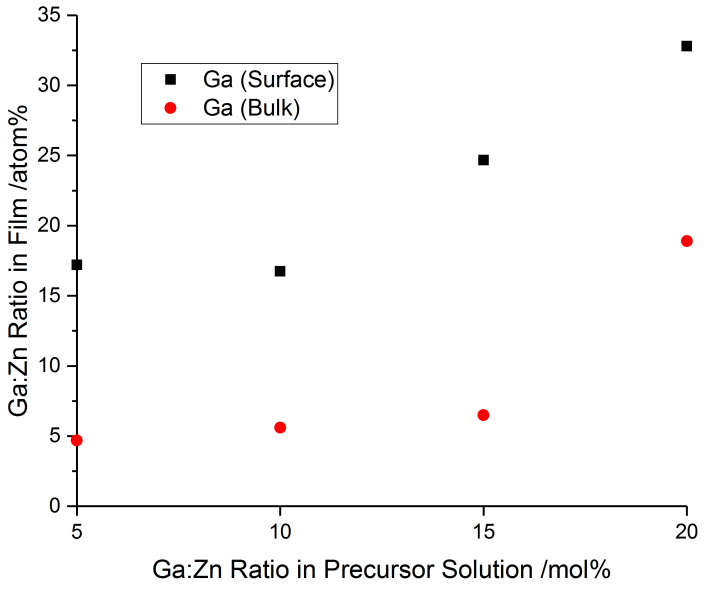

Figure 3.9: Ga:Zn ratios at the surfaces and in the bulks of the GZO films deposited *via* AACVD, as determined by XPS.

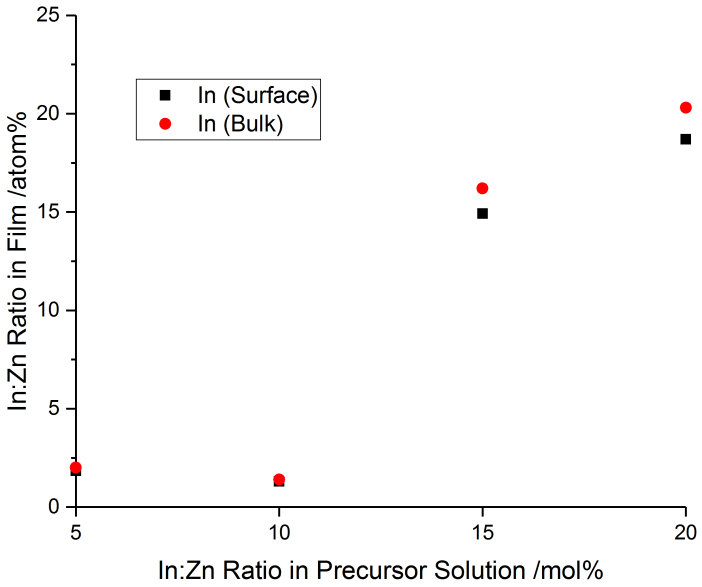

Figure 3.10: In:Zn ratios at the surfaces and in the bulks of the IZO films deposited *via* AACVD, as determined by XPS.

The concentration of Ga^{3+} in the GZO films also increased as the amount in solution was increased (Figure 3.9). However, the trend was not as strong as it was for the AZO films. The gallium in the films was also surface segregated. However, unlike the AZO films, the amount of surface gallium compared to bulk gallium did not change significantly with dopant concentration.

For the IZO films, low concentrations of the dopant did not appear to influence the amount of In^{3+} in the film (Figure 3.10). Only upon doping with 15 mol% indium in solution, was there a significant increase in dopant concentration in the film. Additionally, the IZO films had the lowest amount of surface segregation. This is most likely a result of In^{3+} being the only dopant used with a radius that is larger than that of Zn^{2+}. For this reason, there is a high energy barrier for In^{3+} to diffuse through the lattice, making it difficult for In to segregate to the surface.

3.2.5 *Surface Morphology*

The thicknesses of the films were determined by side-on SEM (Table 3.1). Top-down SEM was used to examine the morphologies of the undoped ZnO film and the 10 mol% doped films.

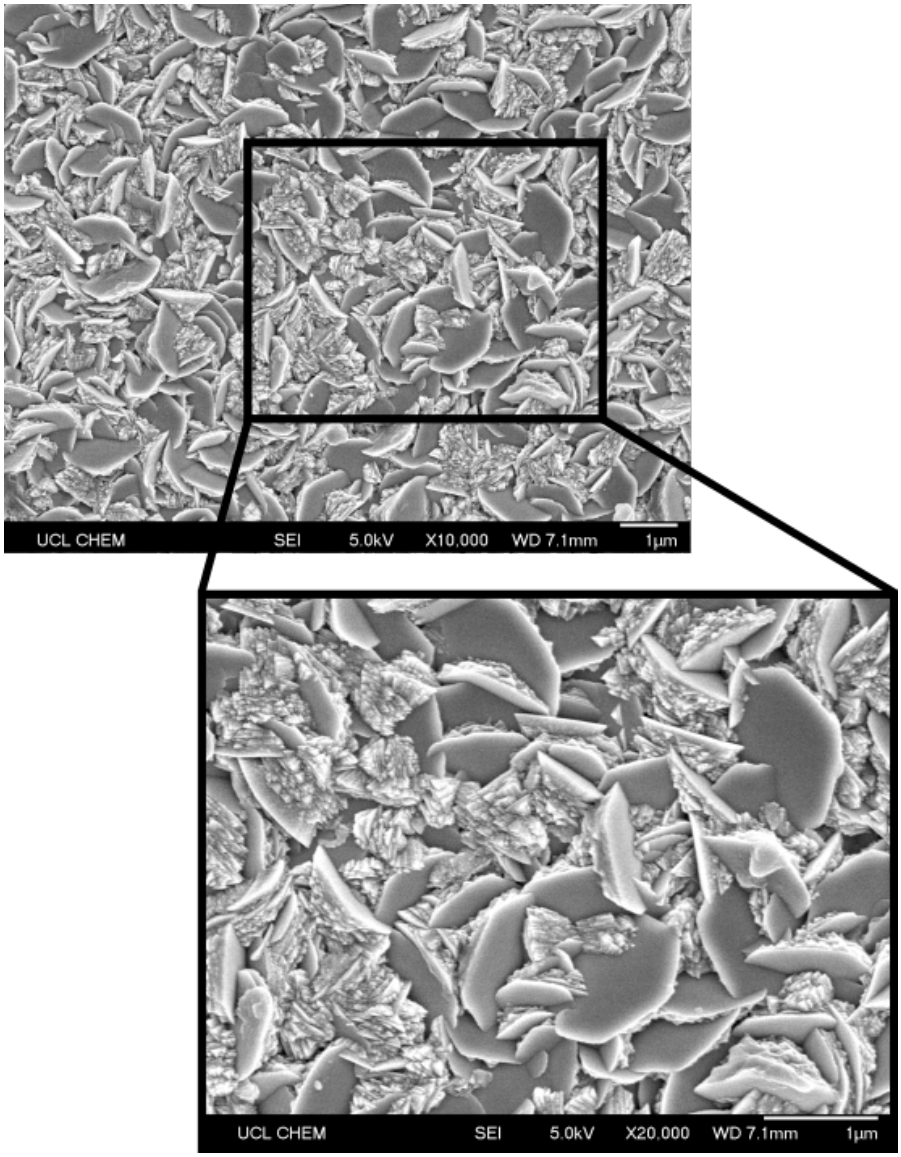

Figure 3.11: SEM images of undoped ZnO film deposited *via* AACVD.

The undoped ZnO film had a grain structure which consisted of interlocking plates (Figure 3.11). These plates were hexagonal in shape, and appeared to be randomly oriented, although many faced upwards, away from the substrate. This is a result of columnar growth,

as indicated by the preferred orientation in the (002) direction, observed in the crystal structure. Additionally, the underside of the hexagonal grains appears to show a rougher, layered morphology. The grains were approximately 1 μm in diameter.

Although the grains were similar in diameter, the grains of the 10 mol% AZO film were not a well-defined hexagonal shape like the grains in the undoped ZnO film (Figure 3.12a). Instead, the plates appeared to have been etched around the edges. It is possible that the aluminium prevented the formation of the clearly defined hexagons. The layered grain structure is still visible, however, and the grains are interlocked in the same way as the undoped film.

The grains in the 10 mol% GZO film were more hexagonal in shape compared to the AZO film (Figure 3.12b). However, they were still not as well-defined as the undoped film, and also appeared to be etched. The grains had holes in the surfaces, revealing the interiors of the grains.

The surface morphology differed significantly for the 10 mol% IZO film (Figure 3.12c). Hexagonal grains were not visible. Instead, the film consisted of a denser structure. Additionally, needle-like formations can be seen scattered across the surface. This is representative of the different preferred orientation observed for the IZO films, in the (100) and (101) directions. Preferred orientation in these directions has led to a more random distribution of crystallites, and is caused by the dopant providing an alternate pathway for precursor decomposition and film growth.[190]

It is apparent that the surface morphology varied significantly, depending on whether aluminium, gallium, or indium was used in the precursor solution. Hence, the morphology was highly dopant-dependant. Different dopants seemed to result in different growth mechanisms, causing different grain structures. This is

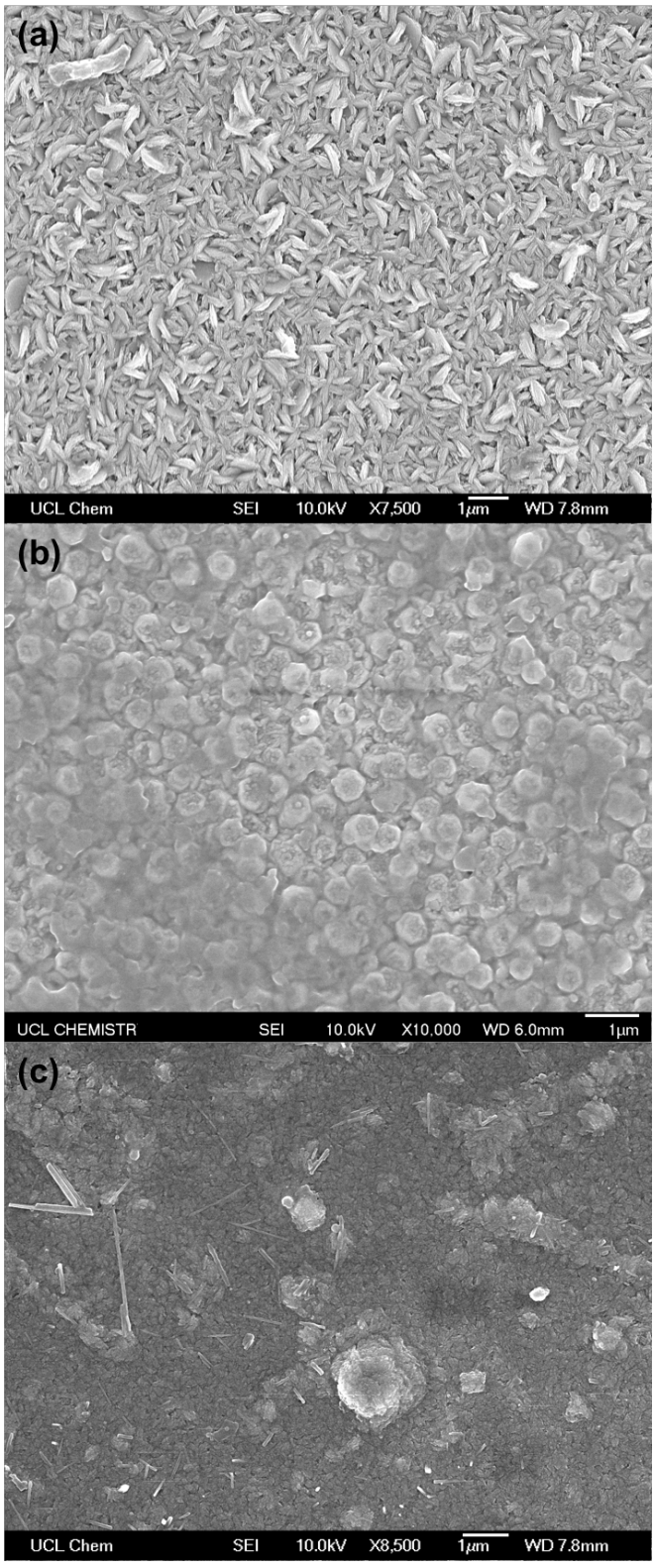

Figure 3.12: SEM images of 10 mol% (a) AZO, (b) GZO, and (c) IZO films deposited *via* AACVD.

significant, as optical properties and electrical properties are often related to the surface morphology of the film.

3.2.6 *Optical Properties*

All of the as-deposited films displayed a high transparency in the visible part of the spectrum (400–700 nm), with many showing >80% (Table 3.2) — exceeding the required limit for commercial applications.

Table 3.2: Optical properties of AZO, GZO, and IZO films deposited *via* AACVD.

Film	$T_{\lambda 400\text{-}700}$ /%	Band gap /eV ($\pm$ 0.01eV)
5 mol% AZO	79	3.25
10 mol% AZO	83	3.30
15 mol% AZO	84	3.50
20 mol% AZO	79	3.32
5 mol% GZO	81	3.28
10 mol% GZO	83	3.31
15 mol% GZO	84	3.37
20 mol% GZO	76	3.33
5 mol% IZO	75	3.30
10 mol% IZO	78	3.33
15 mol% IZO	83	3.33
20 mol% IZO	74	3.10

For each film, the transmittance tended to decrease at longer wavelengths, which indicated a greater absorption of infrared light in comparison to visible light. The trend observed for each dopant was an increase in transmittance with dopant concentration until 15 mol% dopant was used. At 20 mol%, the transmittance decreased again. This can be seen by looking at the UV/Vis spectra (Figures 3.13, 3.14, and 3.15).

The films with the highest transmittance in the visible part of the spectrum were 15 mol% AZO and 15 mol% GZO. These films were not

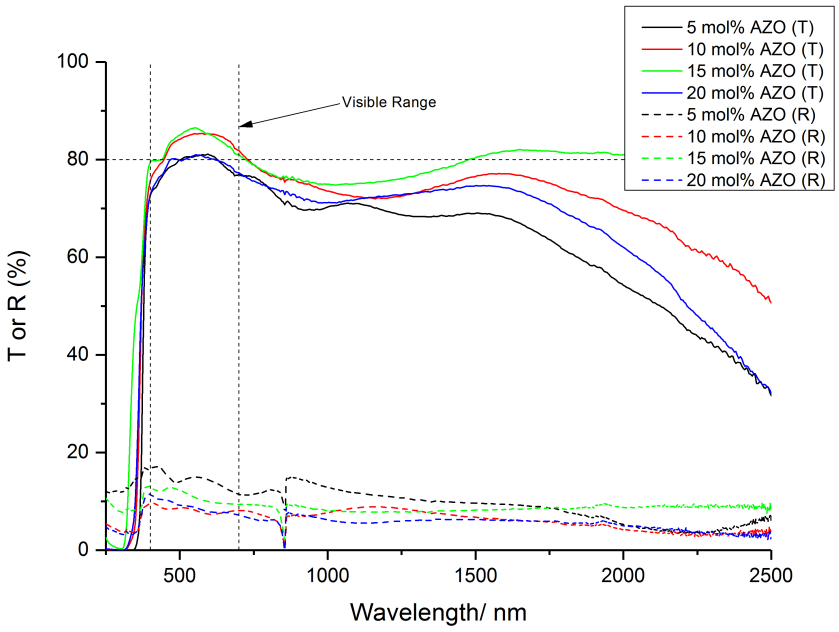

Figure 3.13: Transmission-reflectance spectra for AZO films deposited *via* AACVD.

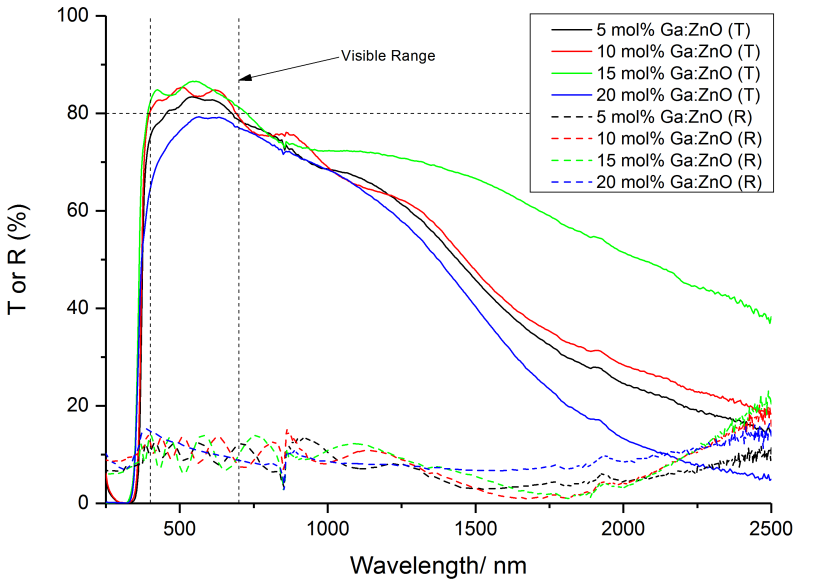

Figure 3.14: Transmission-reflectance spectra for GZO films deposited *via* AACVD.

the thinnest of the deposited films. Their thickness was close to the average thickness, and so the reason for their high transparency is not thickness-related. It could be due to a combination of factors,

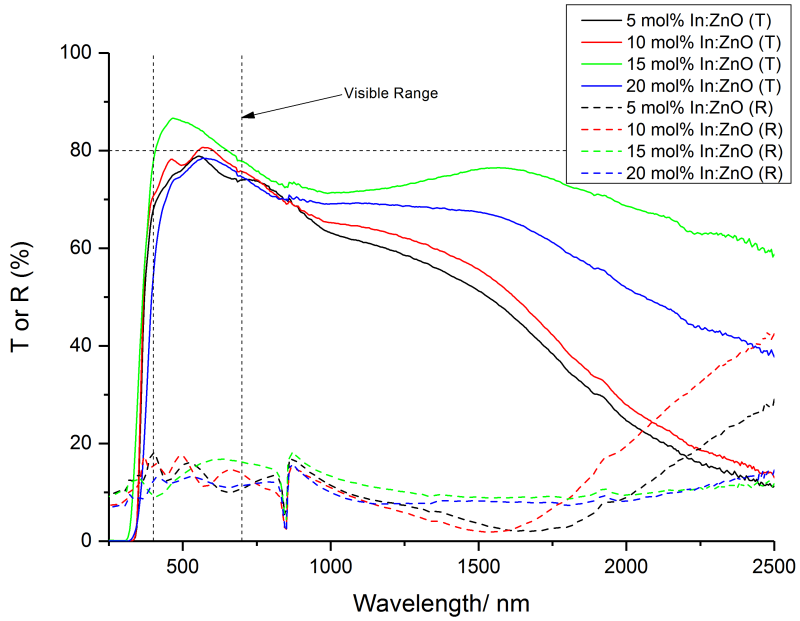

Figure 3.15: Transmission-reflectance spectra for IZO films deposited *via* AACVD.

including the fact that these films possessed the widest band gaps (Table 3.2). This would result in more higher energy visible photons able to pass through the material without being absorbed and exciting an electron. Another reason for their high transparency could be due to the film morphology. If they were slightly less textured, it could result in less scattered light. By examining Figures 3.1 and 3.2, it can be seen that the (002) peaks on the XRD patterns for the 15 mol% AZO and 15 mol% GZO films are less pronounced relative to the (100) and (101) peaks, compared to the patterns for films at lower concentrations. This indicates a reduction in preferred orientation, and thus a reduction in the film texture.[198,246] Therefore, the low carrier concentration and low texture of the film could be reasons for the observed high transparency.

The reflectance of the films did not vary much, and remained low (<20%) across the range of wavelengths scanned. This means that the films would not be appropriate for low emissivity coatings, which

require high IR reflectance in order to act as transparent, thermally insulating window coatings for buildings.[38,247]

The transmission-reflection data for each film was used to generate Tauc plots, from which the band gaps were calculated. The undoped ZnO film had a band gap of 3.16 eV. For each dopant used, there was an initial increase in the band gap, due to the Burstein-Moss effect, as described in Section 1.2.2.1. The BM effect seemed to become less pronounced with increasing dopant size. At high dopant concentrations, the band gap was observed to decrease again, due to the band gap narrowing effect, as described in Section 1.2.2.2.

Overall, the films displayed high transparency. The transparency could potentially be improved further, by using anti-reflection coatings.[248,249] Thus, all of the as-deposited films have the potential to exceed the requirement for 80% transmittance in the visible part of the spectrum.

3.2.7 *Electrical Properties*

The resistivity, carrier concentration, and carrier mobility were obtained using the van der Pauw technique, and are summarised in Table 3.3. The undoped ZnO film was too resistive to measure any electrical properties. All of the doped films displayed *n*-type conductivity, with electrons as the majority charge carriers.

Regardless of the dopant used, the resistivity of the films followed the same trend. The resistivity initially decreased until it reached a minimum when 10 mol% dopant was used in the precursor solution. At higher dopant concentrations, the resistivity increased again. The initial decrease in resistivity is due to the dopant elements introducing charge carriers into the conduction band. The eventual increase in resistivity at high dopant concentrations is due to the

Table 3.3: Electrical properties of AZO, GZO, and IZO films deposited *via* AACVD.

Film	Resistivity $\times 10^{-2}$ /Ω·cm	Carrier concentration $\times 10^{19}$ /cm^{-3}	Mobility /cm^2/V·s
5 mol% AZO	0.8	9.7	8.1
10 mol% AZO	0.5	14.0	9.0
15 mol% AZO	1.1	12.1	4.7
20 mol% AZO	3.5	11.4	1.6
5 mol% GZO	3.0	2.1	9.7
10 mol% GZO	1.3	6.9	7.1
15 mol% GZO	2.0	3.2	10.1
20 mol% GZO	3.3	2.8	6.6
5 mol% IZO	1.8	11.7	3.0
10 mol% IZO	1.7	7.3	5.1
15 mol% IZO	2.1	6.9	4.3
20 mol% IZO	22.0	2.4	1.2

decrease in electron mobility. This could be caused by a combination of factors. One cause is the reduction in crystal quality. The loss of long-range crystal order, as indicated by the XRD patterns (Figures 3.1, 3.2, and 3.3), prevents electrons from passing through the film as easily as they would in a perfect crystal structure. Additionally, there will be an increase in scattering of the electrons by the charged dopant sites, also known as impurity scattering, due to the high concentration of charged dopant sites in the films.

Bazzani *et al.* investigated the effects on the band structure when ZnO is doped with aluminium.[250] They determined that at high dopant concentration, when interstitial aluminium (Al_I) begins to form, additional localised energy levels appear in the band gap. These energy levels have strong aluminium and oxygen components and are almost dispersionless. This indicates that there is a poor overlap between the interstitial aluminium and the oxygen.[5] Bazzani *et al.* concluded that these energy levels result in large effective masses and low electron mobilities, in contrast to substitutional

aluminium. Hence, this could be a further reason for the increase in resistivity at high dopant concentrations.

The GZO films generally displayed the highest mobilities. This is to be expected, for the reasons described in Section 3.2.3. Of the three dopants, Ga^{3+} is closest to Zn^{2+} in terms of ionic radius. This means that the substitution of Ga^{3+} for Zn^{2+} should result in less lattice distortion compared to when Al^{3+} and In^{3+} are used. The preservation of the crystal structure will provide better pathways for the charge carriers, and hence their mobility will be higher.

The charge carrier concentrations for the AZO, GZO, and IZO films are on the order of 10^{19}–10^{20} cm^{-3}. Noh *et al.* calculated that the maximum *n*-type doping limit for AZO is in the range 10^{19}–10^{21} cm^{-3}, in typical growth conditions.[251] This limit is due to the interactions between the positively charged donors (Al_{Zn}) and the negatively charged compensating defects, the zinc vacancies (V_{Zn}). Therefore, the charge carrier concentrations for these films lie within the maximum doping limit described by these calculations. The AZO films displayed the highest charge carrier concentrations, because the AZO films had the highest levels of dopant incorporation, as shown by the XPS data (Figure 3.8). The maximum charge carrier concentration was observed for the 10 mol% AZO film, at 1.4×10^{20} cm^{-3}.

The electrical properties of these films are comparable to other reports of doped ZnO thin films deposited under similar conditions.

Kuprenaite *et al.* deposited AZO onto a glass substrate *via* AACVD at a deposition temperature of 400 °C, and obtained a much poorer resistivity of 2.83 Ω·cm. They used $[Zn(thd)_2]$ and $[Al(thd)_3]$ in 1,2-dimethoxyethane as their precursor solution and a N_2 + O_2 mixture as their carrier gas. Oxygen vacancies have a higher formation energy in oxygen-rich conditions.[72] Hence, the use of oxygen as a carrier gas may have been partially responsible for their

higher resistivity, as it would result in a lower concentration of oxygen vacancies. The carrier gas used for the work described in this chapter was N_2. This should provide an oxygen-poor environment, and hence promote the formation of oxygen vacancies. Nickel *et al.* determined that the incorporation of N_2 can result in defects in ZnO by forming an N_2O molecule, or by breaking a Zn–O bond.[252] This introduces localised states into the band gap, which, for a *p*-type semiconductor, can trap holes and lower the doping efficiency. However, for an *n*-type semiconductor, like the films described in this work, the effect would be negligible. Therefore, N_2 is preferable as a carrier gas for *n*-type ZnO.

Both Bhachu *et al.* and Ponja *et al.* deposited AZO films onto glass substrates *via* AACVD at a deposition temperature of 450 °C.[189,190] They achieved improved resistivities (8.35×10^{-4} Ω·cm and 2.15×10^{-3} Ω·cm, respectively); however, in each case, the precursors used were diethyl zinc and trimethyl aluminium [$AlMe_3$]. Both of these are highly pyrophoric, which made the synthesis procedure non-trivial and dangerous. The films deposited in this work used much safer, more air-stable precursors, which is preferable for commercial applications.

Chen *et al.* investigated the effect of gallium concentration on GZO films deposited on glass substrates *via* AACVD at a deposition temperature of 450 °C.[192] They also used $Zn(acac)_2$ as their zinc precursor, however they used $Ga(acac)_3$ as their gallium precursor. Additionally, they used three times the quantity of MeOH, compared to the amount used for the depositions in this work, resulting in a solution with a much lower concentration of precursors. They achieved a minimum resistivity value of 2.3×10^{-3} Ω·cm for a gallium concentration of 5.7 atom%. This which was higher than the minimum resistivity value obtained for the GZO films in this work.

Chen *et al.* also investigated the effect of deposition temperature and deposition time on GZO films deposited *via* AACVD on glass substrates.[191] They deposited four films at 450 °C, with deposition times of 45 mins, 65 mins, 90 mins, and 135 mins. The film deposited at 45 mins, which was most similar to the films deposited in this work (which had a deposition time of 30–40 minutes), had a resistivity of 2.08×10^{-1} Ω·cm. This is much higher than the minimum resisitivity obtained for the GZO films in this work. The films deposited with longer deposition times had lower resistivities, achieving a minimum value of 8.89×10^{-3} Ω·cm. The prolonged deposition time resulted in an increase in the film thicknesses and allowed the grains to grow larger in size, thus reducing grain boundary scattering. However, the long deposition times are not ideal for commercial applications, in which films would need to be deposited in approximately 20–30 seconds.

Nolan *et al.* deposited IZO films onto glass substrates *via* AACVD at a deposition temperature of 425 °C.[188] They used zinc acetate [$Zn(O_2CCH_3)_2$] and $InCl_3$ as their precursors, and achieved a minimum resistivity of 7.2×10^{-2} Ω·cm. Again, this is higher than the minimum resistivity value obtained for the IZO films deposited in this work. They used simple glass slides as their substrates. The lack of a barrier layer may have resulted in ions leeching between the film and the substrate, resulting in slightly poorer electrical properties.

Table 3.4: Optolectronic properties of common industrial standard TCO materials.[45,112]

Film	Resistivity $\times 10^{-4}$ /Ω·cm	Carrier concentration $\times 10^{20}$ /cm^{-3}	Mobility /cm^2/V·s	$T_{\lambda 400\text{-}700}$ /%
TEC^{TM}8	5.2	5.3	28	82
TEC^{TM}15	5.3	5.6	21	83
Asahi U^{TM}	8.8	2.2	32	–

Overall, the films possess electrical properties that are suitable for some TCO applications. Additionally, the films show improvements over several recent attempts in the literature to deposit AZO, GZO and IZO films using similar conditions. This is especially promising, considering the ease of deposition, due to the safe, air-stable precursors. However, the minimum resistivity achieved ($5 \times 10^{-3}\ \Omega$·cm for 10 mol% AZO) is not quite low enough for most commercial applications (Table 3.4).

3.3 CO-DOPANT STUDY

Co-doping allows the benefits of multiple dopants to be exploited simultaneously. Co-doped ZnO films are less common than individually doped films. Aluminium/gallium co-doped ZnO (AGZO),[140,151,174,253–259] gallium/indium co-doped ZnO (IGZO),[78,218–220,260–263] and aluminium/indium co-doped ZnO (AIZO)[264–268] have been synthesised previously. However, thin films of these materials had not been deposited *via* AACVD prior to this work.

Aluminium is the third most abundant element in the Earth's crust.[269] As a result, it is relatively cheap in comparison to gallium and indium, who rank 35th and 68th respectively, in terms of abundance in the Earth's crust. Furthermore, in comparison to the other group 13 elements, aluminium is relatively non-toxic.[185] This is preferable for commercial usage, where large quantities would be required. However, the high reactivity of aluminium may result in unwanted side reactions during film growth.[254]

Gallium, on the other hand, is a relatively stable dopant element, and as such, it reduces the potential for unwanted side reactions during film growth, compared to other dopants.[220,257] Nomoto *et al.*

found that, after exposing AZO and GZO films to humid environments for long periods of time, the AZO films showed a more dramatic increase in resistivity, indicating that the GZO films are more stable towards humidity.[270] On top of this, Ga^{3+} typically results in less lattice distortion and crystal defects when doped into ZnO, as its radius is similar to that of Zn^{2+}.[271]

Using indium as the only dopant for ZnO typically results in the most lattice distortion, compared to Al^{3+} and Ga^{3+}, because In^{3+} has the largest ionic radius. However, the use of indium as a co-dopant with aluminium or gallium is thought to minimise ZnO crystal defects, as there would be one dopant with a larger radius than Zn^{2+}, and one with a smaller radius.[218] This should aid transport properties. Thus, co-doping is a method whereby the strengths of one dopant can compensate for the weaknesses of another.

3.3.1 *Experimental*

As the 10 mol% individually doped films showed the best optoelectronic properties compared to other dopant concentrations, the total dopant concentration for the co-doped films was kept at 10 mol%.

The film deposition conditions were maintained, using the same conditions as before, except two dopant precursors were used for each deposition. 5 mol% of each dopant, relative to zinc, was used in the precursor solution.

3.3.2 *Film Synthesis*

Aluminium/gallium, gallium/indium, and aluminium/indium co-doped ZnO thin films were synthesised, based on the following reactions:

$$\mathrm{Zn(acac)_{2\,(g)} + \mathit{x}AlCl_{3\,(g)} + \mathit{y}GaCl_{3\,(g)} \xrightarrow{\Delta} Al_{\mathit{x}}Ga_{\mathit{y}}Zn_{1-\mathit{x}-\mathit{y}}O_{\,(s)}}$$
$$\mathrm{Zn(acac)_{2\,(g)} + \mathit{x}GaCl_{3\,(g)} + \mathit{y}InCl_{3\,(g)} \xrightarrow{\Delta} Ga_{\mathit{x}}In_{\mathit{y}}Zn_{1-\mathit{x}-\mathit{y}}O_{\,(s)}}$$
$$\mathrm{Zn(acac)_{2\,(g)} + \mathit{x}AlCl_{3\,(g)} + \mathit{y}InCl_{3\,(g)} \xrightarrow{\Delta} Al_{\mathit{x}}In_{\mathit{y}}Zn_{1-\mathit{x}-\mathit{y}}O_{\,(s)}}$$

All of the as-deposited films were of high quality. They were robust, and showed good adhesion to the glass substrates. The films were handled and stored in air and showed no degradation in quality or properties after 12 months. The films passed the Scotch tape test, and resisted being scratched with a steel scalpel.

Visually, the films appeared the same as the individually doped films. The films were transparent, with visible interference patterns when viewed at an angle. The region closest to the baffle inlet showed the highest quality films in terms of coverage and uniformity, so this was the region that was characterised.

3.3.3 *Crystal Structure*

All of the as-deposited films consisted of pure wurtzite ZnO, with no secondary phases observable by XRD (Figure 3.16).

The AGZO film displayed preferred orientation in the (002) plane, analogous to the individually doped AZO and GZO films (Figures 3.1 and 3.2). Additionally, the peaks for this film were very sharp, indicating high quality crystal growth. Conversely, the IGZO film displayed preferred orientation in the (100) and (101) planes, which was analogous to the individually doped IZO films (Figure 3.3).

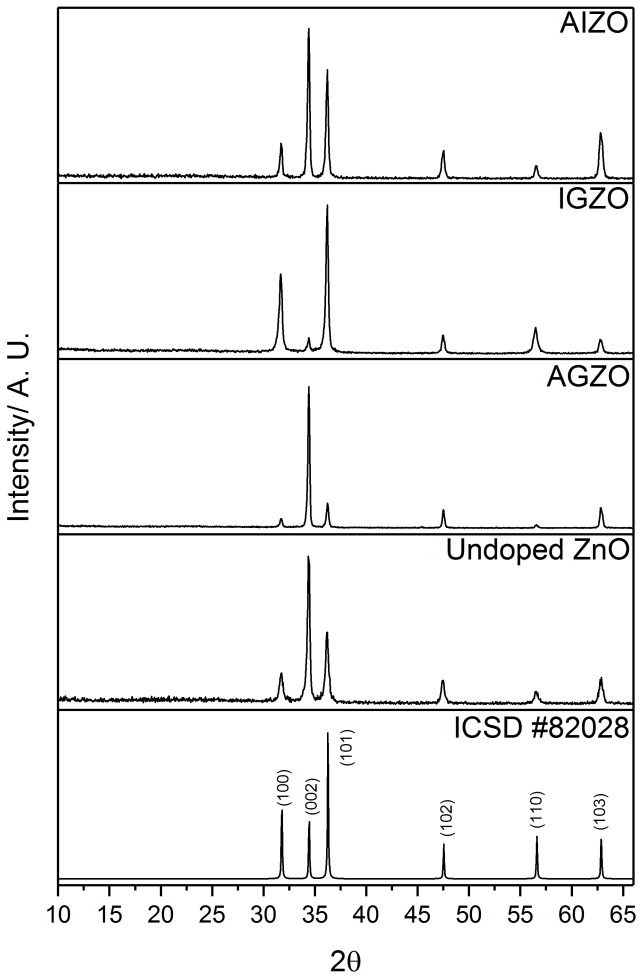

Figure 3.16: X-ray diffraction patterns of AGZO, IGZO, and AIZO films deposited *via* AACVD. An undoped ZnO film also deposited *via* AACVD is included for reference, as well as a diffraction pattern of ZnO from ICSD #82028.

The preferred orientation of the AIZO film appeared to be an amalgamation of the AGZO and IGZO films, with preferred growth in both the (002) and the (101) directions. Again, a slight peak broadening was observed for this film, in comparison to the AGZO film. Teehan *et al.* deposited AIZO films *via* magnetron sputtering.[265] They observed that an increase in indium concentration led to peak broadening, and a reduction in peak intensity. They attributed this to the larger ionic radius of In^{3+}.

From these results, it seems evident that the incorporation of Al^{3+} into ZnO promoted growth in the (002) direction, whereas In^{3+} promoted growth in the (101) direction. Ga^{3+} seems to have had less of an effect over preferred orientation.

The crystallite diameters were 81 nm, 60 nm, and 76 nm for the AGZO, IGZO, and AIZO films, respectively. AGZO had the largest crystallites, indicating high quality crystal growth,. This implies that the incorporation of In^{3+} led to a deterioration in crystallinity, due to its large radius. The small crystallites of the IGZO film is likely due to the fact that this film used the two largest dopants in tandem, which would result in the most lattice distortion in comparison to other dopant combinations. Nguyen *et al.* noted the presence of indium resulted in a deterioration in crystal quality for their IGZO film deposited *via* magnetron sputtering.[218]

3.3.4 *Elemental Analysis*

Just as with the individually doped films, carbon was observed both at the surfaces and within the bulks of the films. This was due to the inefficient thermal decomposition of $Zn(acac)_2$.

When scanning the zinc 2p regions of the films, Zn^{2+} was the only oxidation state observed. The oxygen 2p peaks of each film could be deconvoluted into three oxygen environments — O_I, O_{II}, and O_{III}, corresponding to O^{2-} in ZnO, O^{2-} in oxygen deficient regions, and surface bound oxygen impurities, respectively. Following the same trend as the individually doped analogues, the relative intensities of the O_{II} and O_{III} peaks decreased within the bulks of the films.

The presence of each dopant was confirmed in each film. The dopant concentration at the surfaces of the films and within the bulks are shown in Table 3.5. The dopants were slightly surface

segregated. However, for aluminium and gallium, the amount of surface segregation was significantly less than the individually doped AZO and GZO films (Figures 3.8 and 3.9).

Table 3.5: Dopant concentrations at the film surfaces and within the bulks of AGZO, IGZO, and AIZO films deposited *via* AACVD. The values are given in atom%.

	Surface concentration			Bulk concentration		
Dopant / Film	Al	Ga	In	Al	Ga	In
AGZO	9.6	4.2	–	9.0	4.9	–
IGZO	–	8.7	0.9	–	6.3	0.8
AIZO	4.2	–	1.8	2.1	–	1.0

The binding energies of the aluminium 2p, gallium 3d, and indium 3d peaks in each film corresponded to Al^{3+}, Ga^{3+}, and In^{3+}, respectively. Just as for the individually doped films, no metallic aluminium, gallium, or indium was observed, nor were there any alternative environments corresponding to any other secondary phases. Another observation that can be made from the XPS data is that there seemed to be a preferential incorporation of the lighter dopant element in each co-doped film.

3.3.5 *Surface Morphology*

Just as with the individually doped films, the surface morphologies of the co-doped films were shown to be highly dopant-dependent (Figure 3.17).

The grains of the AGZO film were randomly shaped. They were mostly oriented with their surfaces facing upwards, away from the substrate. The grains of this film were generally smooth, with very few morphological imperfections, such as cracks and pinhole defects.

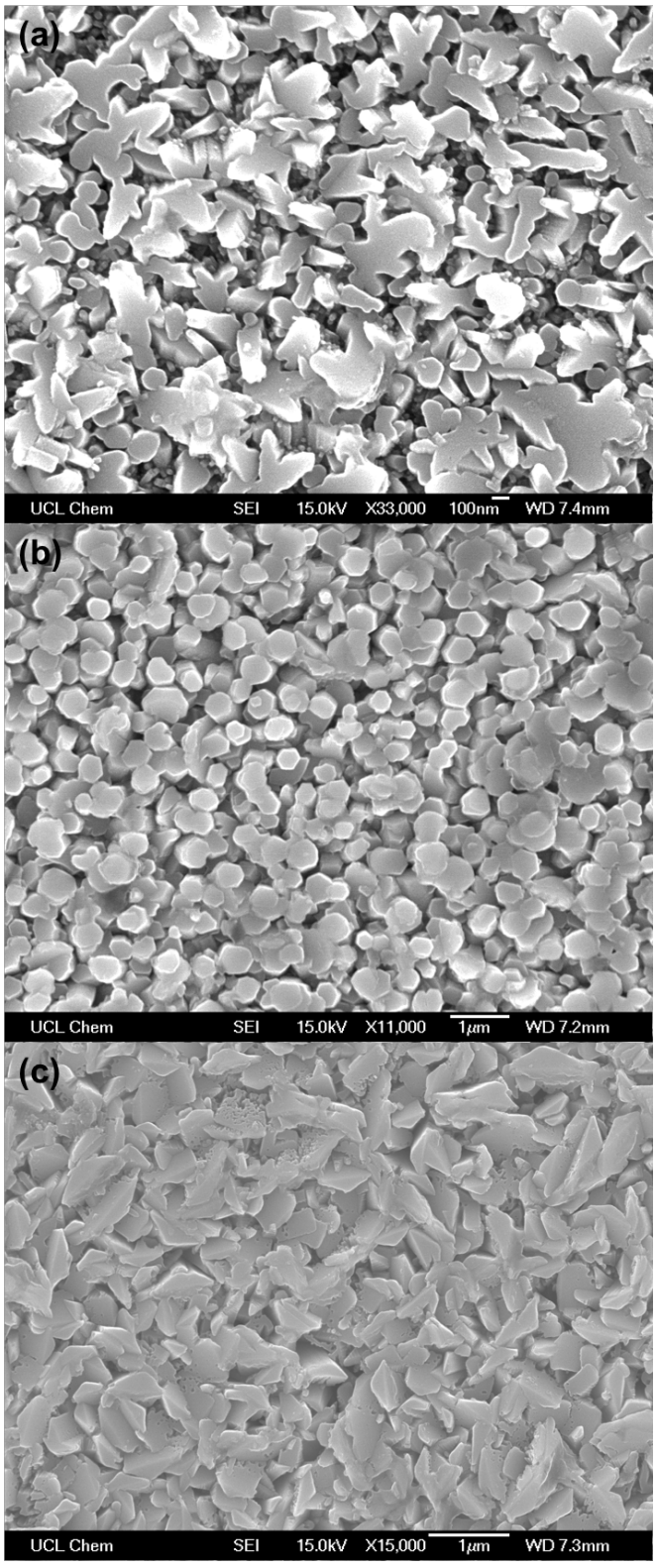

Figure 3.17: SEM images of (a) AGZO, (b) IGZO, and (c) AIZO films deposited *via* AACVD.

All of the grains of the IGZO film were more hexagonal in shape. Again, they grew in a columnar fashion, with the upper surfaces of the grains facing away from the substrate. These grains were also relatively smooth, and had few morphological imperfections. This morphology is similar to IGZO nanorods, synthesised by Lim *et al.* using a hydrothermal technique.[220]

The grains of the AIZO film were similar to the AGZO film, in terms of both grain shape and grain size. However, the AIZO grains were less columnar in nature, and appeared to be more randomly oriented. Moreover, there were many pinhole defects observed across the film.

The fact that the AIZO film possessed the poorest quality morphological structure indicates that the presence of Ga^{3+} in the film aided columnar growth and resulted in smooth grains with relatively few defects. This is likely due to Ga^{3+} having a similar ionic radius to Zn^{2+}, thus allowing for good quality crystal growth with minimal disorder in the structure.

By comparing the morphology of the IGZO film to the morphology of the 10 mol% GZO film (Figure 3.12b), noticable similarities can be seen. The grain size, the hexagonal grain shape, as well as the columnar growth mechanism are all common features on each film. This suggests that gallium had a greater influence over the growth mechanism than indium. Chen *et al.* reported that the segregation of gallium at grain boundaries resulted in a suppression of grain growth, such that the grains cannot coalesce.[192] This could explain why the grains of the GZO and the IGZO film appeared more columnar in nature. Furthermore, the AGZO and AIZO films had a very similar morphology, which indicates that aluminium also had a greater influence over the growth mechanism than indium. The main difference between the AGZO and AIZO morphologies was that the AIZO film had more cracks and pinhole defects, which suggests

that the use of indium was detrimental towards grain growth. This is likely because In^{3+} was the only dopant with a radius larger than Zn^{2+}, resulting in a relatively high concentration of crystal defects, leading to poorer crystal growth.

3.3.6 *Optical Properties*

The average transmittance of the co-doped films was slightly lower than the transmittance of the 10 mol% single doped analogues, suggesting that co-doping had a detrimental impact on visible light transmission. (Figure 3.18).

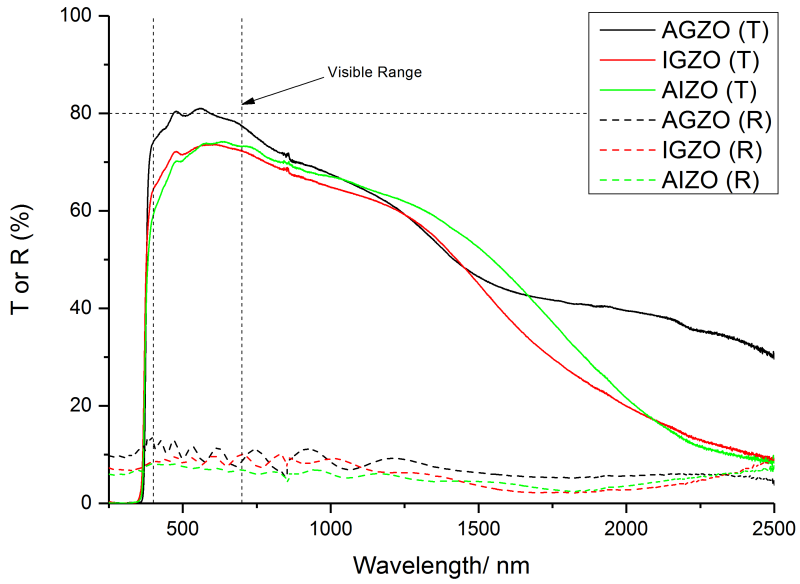

Figure 3.18: Transmission-reflectance spectra for co-doped films deposited *via* AACVD.

The film with the highest transmittance was the AGZO film. The IGZO film and the AIZO film were both very similar in terms of transmittance. This suggests that the incorporation of In^{3+} into the films resulted in an increase in absorbance, thus reducing the transmittance.

The reason for this absorbance is likely due to In^{3+} introducing disorder into the structure due to its large radius. The disorder introduced localised states near the conduction band minimum. The band tail of these states is known as the Urbach energy.[272–276] The additional states that arose due to the structural disorder resulted in an increase in absorption. Generally, the more disorder that is present in the structure, the greater the Urbach tail width. The use of any dopant will cause some disorder in the structure; however, as In^{3+} is the only dopant from this work with a radius larger than that of Zn^{2+}, it resulted in the greatest amount of disorder. This explains the reduction in visible transmittance for the films which contain In^{3+}.

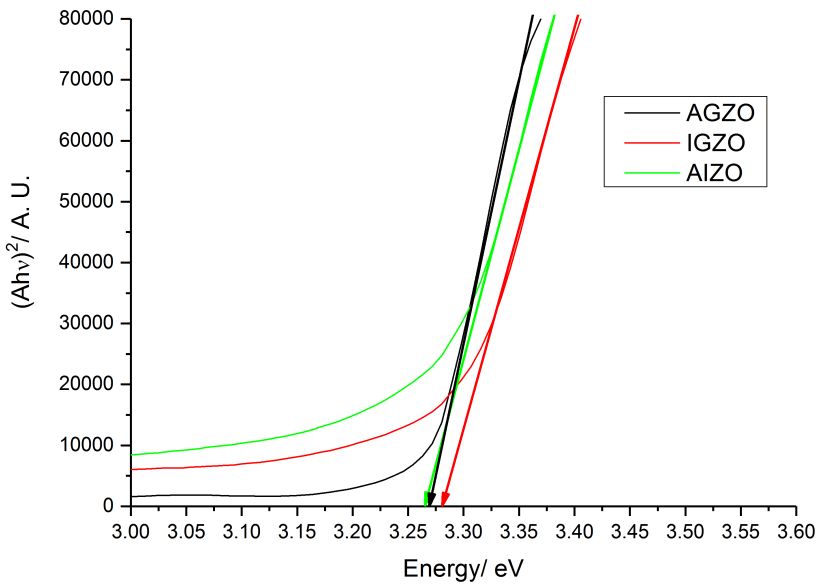

Figure 3.19: Tauc plots for co-doped films deposited *via* AACVD.

The transmission-reflectance data was used to generate Tauc plots (Figure 3.19). These plots confirm the disorder introduced into the structure due the presence of indium. The Urbach energy typically manifests itself as a long wavelength absorption tail added to the main absorption edge.[273] The Urbach tails for the IGZO and AIZO films were higher in terms of absorbance than the AGZO film. The

Tauc plots also revealed that the optical band gaps of the films were not dopant-dependant, and remained constant at 3.27–3.28 eV. This is similar to the band gaps of the 10 mol% AZO, GZO, and IZO films (Table 3.2). The undoped ZnO film deposited in the same conditions yielded a band gap of 3.16 eV. Hence, the co-doped films resulted in a widening of the band gap. This was due to the Burstein-Moss effect.

3.3.7 *Electrical Properties*

The electrical properties of the co-doped films are summarised in Table 3.6. They are similar to those of the 10 mol% individually doped films. However, they did not show any improvement in terms of resistivity.

Table 3.6: Electrical properties of co-doped films deposited *via* AACVD.

Film	Resistivity $\times 10^{-2}$ /Ω·cm	Carrier concentration $\times 10^{19}$ /cm^{-3}	Mobility /cm^2/V·s
AGZO	1.3	10.3	7.9
IGZO	2.1	6.8	3.3
AIZO	1.6	8.2	6.8

The AGZO film had the lowest resistivity and the highest mobility of the co-doped films. This indicates that the presence of In^{3+} resulted in more lattice distortion, resulting in poorer transport properties. The AIZO film was close to the AGZO film in terms of mobility, which suggests that the presence of Al^{3+} partially compensated for the lattice distortion caused by In^{3+}. This was due to Al^{3+} having a smaller ionic radius than Zn^{2+}, whereas In^{3+} has a larger radius.

One issue that is often a limiting factor for the electrical properties is the film morphology. In order to investigate the effect of the solvent on the film morphology, a solvent study was performed, to see if the electrical properties could be improved further.

3.4 SOLVENT STUDY

Morphological control is a desireable feature for a deposition process, as different applications may require different morphology-related properties. For example, for certain solar cell applications, the grains should be textured, with a high surface roughness, in order to scatter and trap visible photons for improved absorbance.[38,277,278] For TCO applications, the grains should be large and well-connected to provide good pathways for conducting electrons, and to prevent grain boundary scattering.[256,262,279] This is because smaller grains will result in a larger amount of grain boundaries, and hence an increase in grain boundary scattering. Grain boundary scattering can be caused by chemisorbed oxygen at the boundaries, which acts as an electron trap.[142,153] It can also be caused by a build up of charge at the boundaries, caused by the discontinuity presented by grain boundaries, particularly in a polycrystalline film.[280]

In samples where the mean-free path of the carriers is smaller than the grain size, grain boundary scattering generally makes a smaller contribution to the carrier mobility, compared to other scattering mechanisms, such as impurity scattering.[16,281] Having said this, it is important to note that grain boundary scattering has a more profound effect on ZnO-based TCOs than it does on ITO.[282] Ellmer *et al.* reported that for ITO films, grain boundary scattering was not observed at carrier concentrations on the order of 10^{18} cm^{-3}, but for AZO films, the carrier mobility was still limited by grain boundary scattering at carrier concentrations on the order of 10^{20} cm^{-3}. This is because AZO films have a significantly higher concentration of carrier traps at the grain boundaries, compared to ITO (3×10^{13} cm^{-2} and 1.5×10^{12} cm^{-2}, respectively).[283,284] Therefore, it is important to be able to

control the grain structure of ZnO-based TCOs, in order to optimise the optoelectronic properties.

A major advantage of AACVD is that morphological control over the as-deposited films is easily achievable, simply by varying the solvent used to make up the precursor solution.[45,110] In order to investigate the way that the morphology affects the optoelectronic properties of the films, the most conductive film from the dopant study (10 mol% AZO) was selected for further experiments.

3.4.1 *Experimental*

The film depositions were repeated with the same conditions as before, except for the solvent used to make up the precursor solution. The additional solvents used for this study were toluene, tetrahydrofuran (THF), n-hexane, cyclohexane, and ethyl acetate.

Due to the low solubility of $Zn(acac)_2$, MeOH was also used in each case, in a 1:1 mixture with another solvent (Table 3.7). The total volume of solvent used for each deposition was kept at 20 mL.

Table 3.7: Solvent combinations used for solvent study.

Solvent 1 (10 mL)	Solvent 2 (10 mL)	Polarity of solvent 2[285]	Viscosity of solvent 2[285] /cP
MeOH	MeOH	76.2	0.60
MeOH	Toluene	9.9	0.59
MeOH	Tetrahydrofuran	21.0	0.55
MeOH	n-Hexane	0.9	0.31
MeOH	Cyclohexane	0.6	0.98
MeOH	Ethyl Acetate	23.0	0.46

3.4.2 *Film Synthesis*

MeOH has one of the highest polarities of any organic solvent.[285] Many of the solvents used for this study had a relatively low polarity (Table 3.7), which led to partial immiscibility of some of the solvents with MeOH. For this reason, a phase separation was often observed in the precursor solution prior to deposition. However, this did not appear to affect the deposition, as the process of generating the aerosol using ultrasonic vibrations was enough to continually mix the solution, to avoid any inhomogeneity in the solution. In each case, the entire precursor solution was transported to the reactor, without any solvent left behind.

All of the as-deposited films were of high quality, and showed good adhesion to the glass substrates. The films were handled and stored in air and showed no degradation in quality or properties after 12 months. The films passed the Scotch tape test, and resisted being scratched with a steel scalpel. Visually, the films appeared the same as those deposited in the dopant study. Interference patterns were visible when the film was viewed at an angle. Again, the region closest to the baffle showed the highest quality films in terms of coverage and uniformity, so this is the region that was characterised.

3.4.3 *Crystal Structure*

The only crystal phase observed in the XRD data was wurtzite ZnO (Figure 3.20). No secondary phases were detected.

The preferred orientation of the films remained in the (002) direction, regardless of the solvent used. However, the peak intensities varied. The XRD pattern for the film grown using only MeOH had the sharpest, most intense peaks, indicating a high

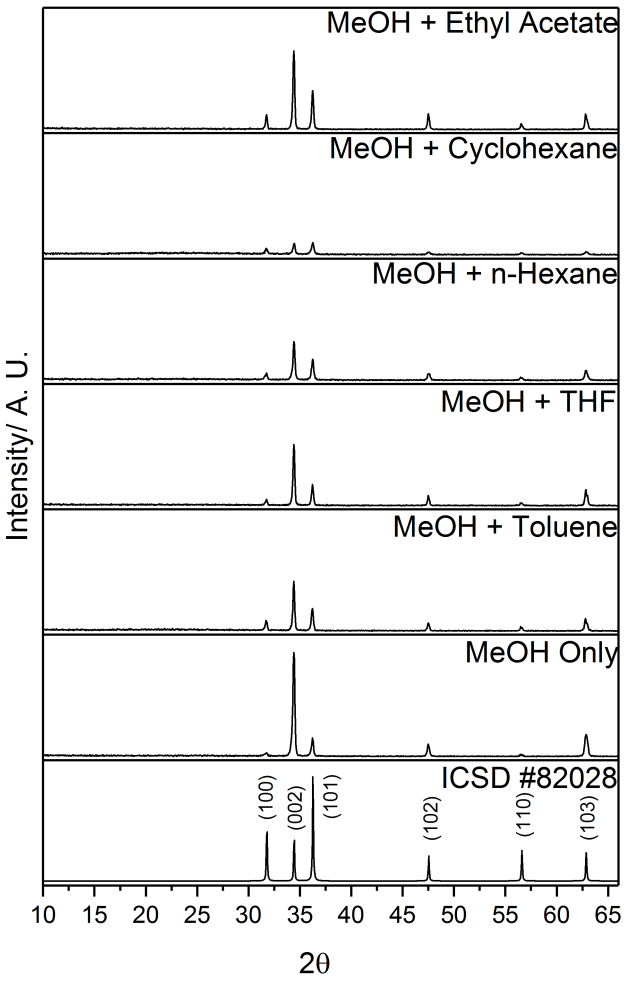

Figure 3.20: X-ray diffraction patterns of 10 mol% AZO films deposited *via* AACVD using different solvents. A diffraction pattern of ZnO from ICSD #82028 is also included for reference.

degree of crystallinity. The films deposited using toluene, THF, and ethyl acetate led to an increase in crystallite diameter, and thus an improvement in crystallinity. The XRD pattern for the film grown using MeOH and cyclohexane had the peaks with the lowest intensity. This is partially due to the fact that this film was thinner than the other films (0.4 μm *vs.* 1 ± 0.2 μm) (Table 3.8), and may also be due to the fact that it had poorer crystallinity. The peaks for this film were also slightly broadened, which is reflected in the relatively small crystallite diameter.[255,286,287] This is evident when looking at the SEM

image for this film, which also shows the smaller grain size. (Figure 3.22e).

The solvent mixture which resulted in the most crystalline film (other than when only MeOH was used) was MeOH and ethyl acetate. Compared to the other solvent mixtures, the XRD pattern for this film had the sharpest, most intense peaks, which indicate a high quality crystal structure, with relatively few defects. This film also possessed some of the largest crystallites. This is desirable, as crystal defects are typically detrimental towards the carrier mobility.[193]

Table 3.8: Structural properties of 10 mol% AZO deposited using different solvents. The film thicknesses were determined by side-on SEM, and have an error of $\pm$ 0.1 μm.

Solvent	Crystallite diameter /nm	Preferred orientation	Film thickness /μm
MeOH only	72	(002)	1.2
MeOH and toluene	92	(002)	1.0
MeOH and THF	85	(002)	1.0
MeOH and n-hexane	76	(002)	0.8
MeOH and cyclohexane	62	(002)	0.4
MeOH and ethyl acetate	85	(002)	1.2

3.4.4 *Elemental Analysis*

Carbon was observed at the surfaces of the films, and within the bulks, due to the inefficient breakdown of $Zn(acac)_2$. The carbon peaks varied in intensity for the films deposited using different solvents, indicating that the solvent was also thermally degrading and contributing towards carbon contamination. The film with the most carbon contamination was the film deposited using ethyl acetate. Kafizas *et al.* have previously reported that ethyl acetate can

cause significant carbon contamination in thin films deposited *via* APCVD, when used in large quantities.[288–290]

The binding energies of the zinc 2p and aluminium 2p peaks were all similar to the AZO films described earlier in the chapter. These peaks corresponded to Zn^{2+} and Al^{3+}, respectively. No peaks indicating the presence of metallic aluminium were observed.

The concentration of Al^{3+} at the surfaces of the films and within the bulks varied with the solvent used to make up the precursor solution (Figure 3.21).

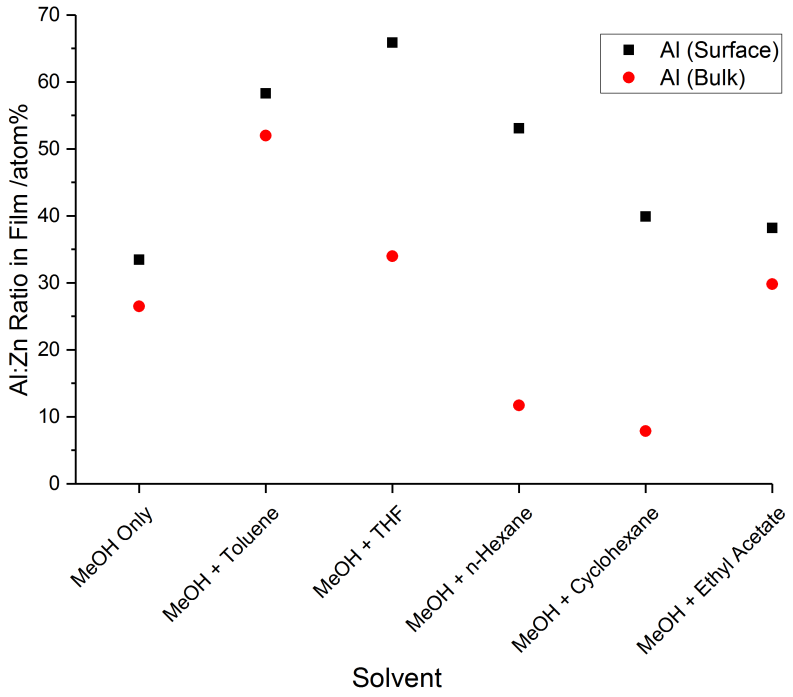

Figure 3.21: Al:Zn ratios at the surfaces and in the bulks of the AZO films deposited *via* AACVD using different solvents, as determined by XPS.

The use of MeOH and toluene resulted in an increase in the incorporation of Al^{3+}, both at the surface and within the bulk. When THF was used, the concentration of Al^{3+} in the bulk was similar to when MeOH was the only solvent, but the concentration at the surface increased significantly. This indicates that there was an increase

in the concentration of Al_2O_3 segregated to the grain boundaries. Because this is an insulating phase, it should result in a deterioration in the electrical properties of the film. When n-hexane or cyclohexane were used, the amount of Al^{3+} incorporated into the film was reduced, whereas the amount segregated at the surface increased. The low Al^{3+} concentration in the films will result in a lower carrier concentration. Coupled with the high concentration of insulating Al_2O_3, these films should display poor electrical properties. Finally, the film deposited using MeOH and ethyl acetate appeared to be very similar to the film deposited using MeOH only.

The discrepancies between the surface and bulk concentrations for the films deposited using different solvents may be due to the variation in the precursor solubility in the different solvents. Both n-hexane and cyclohexane possess the lowest polarities of any of the solvents used (Table 3.7). This would have led to immiscibility with the MeOH, which may explain the relatively low concentration of Al^{3+} in the bulks of these films.

3.4.5 *Surface Morphology*

The morphologies of the different films varied significantly, depending on the solvent used to make up the precursor solution (Figure 3.22). None of the films consisted of the well-defined hexagonal grains that were visible for the undoped ZnO film (Figure 3.11). The grain shapes and sizes appeared to be strongly dependent on the solvent.

The films deposited using MeOH and THF (Figure 3.22c), MeOH and n-hexane (Figure 3.22d), and MeOH and ethyl acetate (Figure 3.22f) had the largest grains. Additionally, the growth of these films appeared to be more columnar in nature, with the surfaces of the

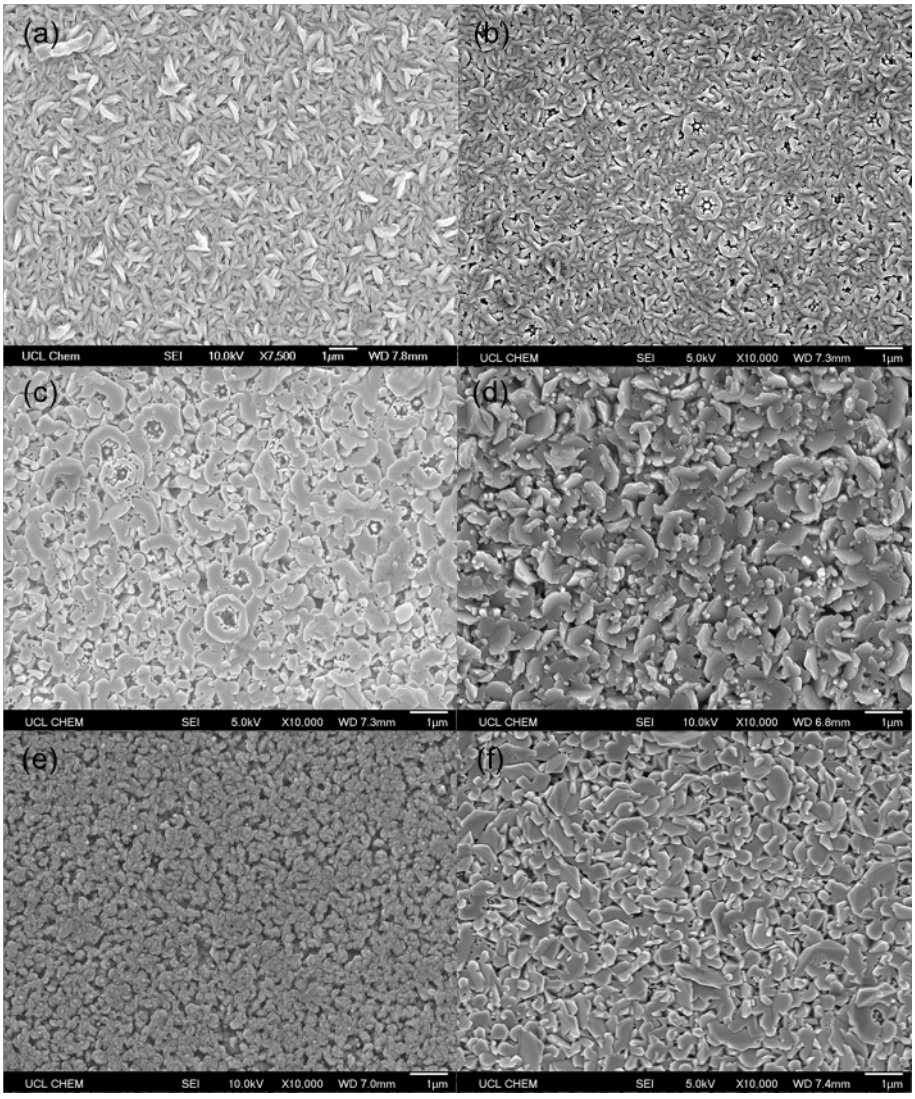

Figure 3.22: SEM images of 10 mol% AZO deposited *via* AACVD using (a) MeOH only, (b) MeOH and toluene, (c) MeOH and tetrahydrofuran, (d) MeOH and n-hexane, (e) MeOH and cyclohexane, and (f) MeOH and ethyl acetate as the solvents used to make up the precursor solution.

grains generally facing upwards, away from the substrate. Notably, of the solvents used, THF and ethyl acetate both had the highest polarities after MeOH, which led to higher miscibility with MeOH. This indicates that the superior miscibility between the solvents and MeOH resulted in improved grain growth. On top of this, THF, n-hexane, and ethyl acetate had the lowest viscocities of the solvents used, which suggests that the use of a solvent with a lower viscosity also resulted in improved grain growth. The reason for this could

be that the aerosol can be generated more easily and consistently from a low-viscosity solution than it can from a high-viscosity solution.[106] Wang *et al.* measured the droplet sizes of different aerosols generated using an ultrasonic nebulizer.[291] They found that the mean droplet size was directly proportional to the viscosity of the solution. Decreasing the viscosity led to a decrease in the mean droplet size. They also determined that this led to an increased spray volume rate. Thus, with a lower viscosity solution, there will be a more rapid, continuous supply of precursors to the substrate, resulting in improved growth mechanics.

This is in contrast to the films deposited using MeOH only (Figure 3.22a), MeOH and toluene (Figure 3.22b) and MeOH and cyclohexane (Figure 3.22e), which had smaller, more randomly-oriented grains. The film deposited using MeOH and toluene was very similar to the film deposited using MeOH only. This could be due to the fact that toluene had a very similar viscosity to MeOH, which means the aerosols generated from the two precursor solutions would be very similar. Cyclohexane had the lowest polarity and highest viscosity of all the solvents used. This led to poor miscibility with MeOH, and a relatively viscous solution. As a result, the film deposited using MeOH and cyclohexane had the smallest grains (<100 nm). On top of this, there were large gaps between many of the grains. This morphology suggests that this film would have the poorest electrical properties, due to a large amount of grain boundary scattering, and poor pathways for charge carriers.

As stated previously, for TCO applications, it is preferable to have large, well-connected grains to provide good pathways for charge carriers. This is particularly important for ZnO-based TCOs which possess a high concentration of carrier traps at the grain boundaries.[283,284] Thus, of the different solvent combinations used,

the most promising were MeOH and THF, MeOH and n-hexane, and in particular, MeOH and ethyl acetate. The film deposited using MeOH and ethyl acetate not only had relatively large grains, but it does not appear to have the pinhole defects and smaller crystallites amongst the grains, both of which were present in the other films. Factoring in the high quality crystal structure of the film deposited using MeOH and ethyl acetate, it is likely that this film will show improved carrier mobilities.

3.4.6 *Optical Properties*

The transmission-reflectance plots for the films generally showed high transmittance and low reflectance across the wavelengths scanned (Figure 3.23). However, all of the films that used a solvent mixture showed a lower transmittance in the visible part of the spectrum, compared to the film deposited using MeOH only. This could be due to an increase in carbon contamination from the different solvents. Carbon contamination can be a cause of a visible darkening in thin films.[187,292]

It is worth noting that MeOH has the lowest boiling point of any of the solvents used for this study.[285] This could indicate that MeOH is more likely to evaporate prior to reaching the substrate surface, compared to the other solvents. Hence, it is possible that MeOH will be transported away by the carrier gas, and passed through the exhaust before it has a chance to contaminate the film with carbon.

Hassan *et al.* found that, for their indium oxide films deposited *via* AACVD, the use of toluene as the solvent for their precursor solution resulted in an increase in carbon contamination, compared to the films deposited from a solution using MeOH.[293] Similarly, Kafizas *et al.* have reported that ethyl acetate can cause significant carbon

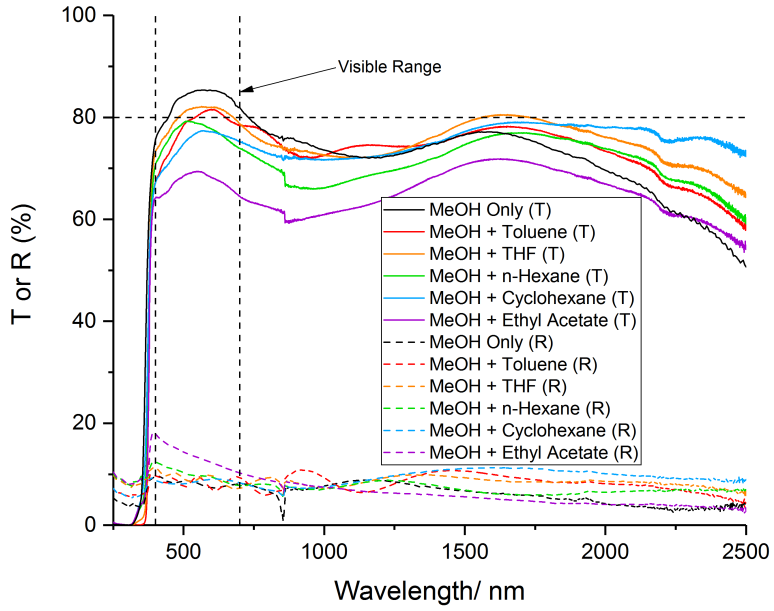

Figure 3.23: Transmission-reflectance spectra for 10 mol% AZO deposited *via* AACVD using different solvents.

contamination in thin films deposited *via* APCVD, when used in large quantities.[288–290] However, their depositions used <0.01 moles of ethyl acetate. For the depositions in this section, over 10 times the amount of ethyl acetate was used, which makes it probable that there will be a significant amount of carbon contamination. This could explain the fact that the film deposited using MeOH and ethyl acetate displayed the lowest transmittance (only ~65-70% transmittance across the visible part of the spectrum) compared to the films deposited using other solvents.

3.4.7 *Electrical Properties*

The electrical properties of the films varied considerably. The addition of toluene or THF to the precursor solution resulted in an decrease in carrier mobility by over an order of magnitude, compared to when only MeOH was used (Table 3.9). This resulted in a significant

increase in resistivity. The reason for this change was likely due to an increase in both crystallographic and morphological defects in the films. The deterioration of electron pathways detrimentally affected the electrical properties of these films.

Table 3.9: Electrical properties of 10 mol% AZO films deposited *via* AACVD using different solvents.

Solvent	Resistivity $\times 10^{-2}$ /Ω·cm	Carrier concentration $\times 10^{19}$ /cm^{-3}	Mobility /cm^2/V·s
MeOH only	0.5	14.0	9.0
MeOH and toluene	27.2	7.1	0.3
MeOH and THF	44.2	5.3	0.3
MeOH and n-hexane	N/A	N/A	N/A
MeOH and cyclohexane	N/A	N/A	N/A
MeOH and ethyl acetate	0.2	9.7	13.3

This effect was even more extreme for the films deposited using MeOH and n-hexane and MeOH and cyclohexane, both of which were too resistive to give any electrical properties *via* the van der Pauw method.

The use of MeOH and ethyl acetate resulted in an improvement in the electron mobility, leading to a 60% reduction in resistivity, compared to when only MeOH was used. This is due to the high quality crystallinity, as shown in its XRD pattern (Figure 3.20), and its relatively large, smooth grain structure (Figure 3.22f).

Therefore, it has been shown that the electrical properties of the film can be considerably improved through morphological control, simply by varying the solvent used to make up the precursor solution.

3.5 CONCLUSIONS

AACVD was used to deposit aluminium-, gallium-, and indium-doped zinc oxide thin films on glass substrates. Dopant concentrations of

5, 10, 15, and 20 mol% were used. The films were of high quality, with good adherence to the glass substrates. Only wurtzite ZnO was detected by XRD, with no secondary phases observable. The films were highly transparent, with several >80% in the visible part of the spectrum, meeting the requirement for industrial applications. The electrical properties were comparable to other reports of doped ZnO films deposited under similar conditions. The electrical properties were particularly good, when considering the ease and low cost of the synthesis, by using safe, easy to handle precursors. The minimum resistivity achieved was 5×10^{-3} Ω·cm, for the 10 mol% AZO film.

The films were also co-doped, maintaining the total dopant concentration at 10 mol%. The co-doped films showed improved electrical properties in comparison to undoped ZnO. However the electronic properties of the co-doped films were generally poorer than the individually doped analogues. It was found that the incorporation of In^{3+} was detrimental towards the optoelectronic properties, due to the lattice distortion cause by its large radius.

Additionally, it was found that the surface morphologies of the films were highly dependent on the solvent used to make up the precursor solution. By using a 1:1 mixture of MeOH and ethyl acetate, the carrier mobility increased, leading to a 60% decrease in resistivity, down to 2×10^{-3} Ω·cm. This is a simple, elegant way to improve the electrical properties of a material, and highlights the benefits of AACVD.

4

SILICON-DOPED ZINC OXIDE THIN FILMS DEPOSITED *VIA* AACVD

This chapter focuses on the synthesis of silicon-doped zinc oxide thin films, and fluorine/silicon co-doped zinc oxide thin films. The films were synthesised *via* AACVD, with the dopant concentrations varied in order to find the optimum optoelectronic properties.

4.1 INTRODUCTION

In the previous chapter, it was established that aluminium, gallium, and indium are all effective dopants for zinc oxide. Individually doped AZO, GZO, and IZO, as well as co-doped AGZO, IGZO, and AIZO all show improved optoelectronic properties in comparison to undoped ZnO. However, there is a drawback of using these elements as dopants for ZnO. For solar cell applications, it is possible for the group 13 elements to diffuse into the amorphous silicon (a-Si) layer during device fabrication.[294,295] These elements can introduce acceptor impurities in the a-Si layer, resulting in disorder and an overall degradation of the solar cell.[296] Similarly, In^{3+} can diffuse into the emissive polymer layer of an LED, which lowers its stability and decreases its lifetime.[282,297] By using silicon as the dopant for ZnO, this degradation can theoretically be reduced.

Another benefit of using silicon is that it has the potential to act as a multielectron donor. This is beneficial, because at high dopant concentrations, there will inevitably be a high concentration

of impurity scattering centres. These will offset the electrons injected into the conduction band, by limiting the mobility. If the dopant element can donate multiple electrons, then the concentration of impurity scattering centres will be kept to a minimum, whilst simultaneously supplying a high concentration of charge carriers.

Silicon-doped ZnO (SZO) thin films have been synthesised previously by various techniques, including magnetron sputtering,[296,298,299] pulsed laser deposition,[17,300–302] sol-gel synthesis,[303–305] atomic layer deposition,[306] and spray pyrolysis.[307] However, SZO had not been synthesised *via* AACVD prior to this work.

4.2 SILICON DOPANT STUDY

4.2.1 *Experimental*

The deposition conditions from Chapter 3 were maintained for the depositions in this chapter. Tetraethyl orthosilicate (TEOS) [$Si(OC_2H_5)_4$] was used as the silicon precursor, at concentrations relative to zinc ranging from 0.2 mol% to 10 mol%. TEOS was selected as the silicon precursor due to its low cost, and its stability in air.

4.2.2 *Film Synthesis*

Silicon-doped ZnO thin films were synthesised, based on the following reaction:

$$Zn(acac)_{2\,(g)} + xSi(OC_2H_5)_{4\,(g)} \xrightarrow{\Delta} Si_xZn_{1-x}O_{\,(s)}$$

Each deposition was repeated at least three times. No significant difference was observed between depositions, indicating the deposition of each film was reproducible. The films were all of high

quality, and showed good adhesion to the glass substrates. The films passed the Scotch tape test, and resisted being scratched with a steel scalpel.

Visually, the films looked similar to the films deposited in the previous chapter. They had visible interference patterns, and again, the highest quality regions of the films in terms of coverage and uniformity were found nearest to the baffle. For this reason, these regions were characterised.

4.2.3 *Crystal Structure*

The crystal structures of the SZO films were determined using XRD (Figure 4.1). All of the as-deposited films consisted of pure-phase wurtzite. No secondary zinc silicate phases were observed by XRD, even at high dopant concentrations.

Table 4.1: Structural properties of SZO films deposited *via* AACVD. The film thicknesses were determined by side-on SEM, and have an error of $\pm$ 0.1 μm.

Solvent	Crystallite diameter /nm	Preferred orientation	Film thickness /μm
0.2 mol% SZO	70	(002)	1.0
0.5 mol% SZO	69	(002)	1.0
2 mol% SZO	55	(002)	1.0
4 mol% SZO	58	(002)	0.9
6 mol% SZO	53	(002)	1.1
8 mol% SZO	50	(002)	1.2
10 mol% SZO	52	(002)	1.0

Analogous to the AZO and GZO films from the previous chapter, the SZO films had a preferred orientation in the (002) direction. Preferred orientation along the *c*-axis has also been observed in SZO thin films prepared by a variety of other techniques.[17,298,300–302,304,306–308]

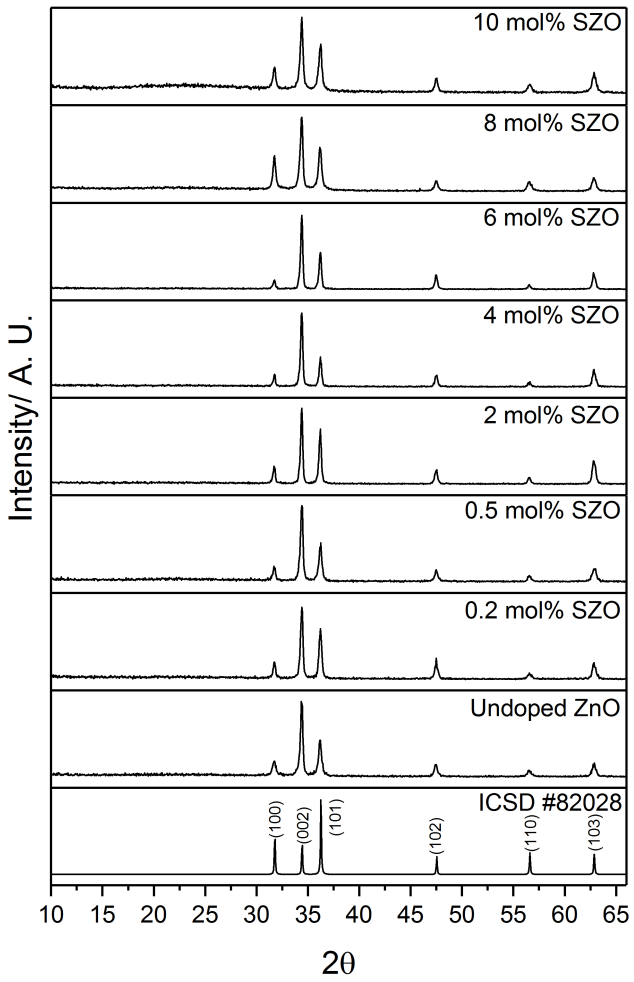

Figure 4.1: X-ray diffraction patterns of the SZO films deposited *via* AACVD. An undoped ZnO film also deposited *via* AACVD is included for reference, as well as a diffraction pattern of ZnO from ICSD #82028.

Additionally, the crystallite diameters decreased significantly with silicon concentration. This could be due to the strain experienced as a result of silicon substituting for zinc, which can be attributed to the smaller radius of the Si^{3+} ions (0.40 Å) in comparison to the radius of 4 co-ordinate Zn^{2+} (0.74 Å).[309] Jilani *et al.* deposited SZO thin films *via* magnetron sputtering and noted a decrease in XRD peak intensity at higher silicon concentrations.[308] They attributed this change to a degeneration of crystallinity with silicon doping.

Similarly, Yuan *et al.* observed a broadening of the XRD peaks with increasing silicon concentration for their SZO films deposited *via* atomic layer deposition, which they attributed to the deteriorating effect of silicon on ZnO crystal quality.[306]

Korner *et al.* calculated the electronic structure of SZO and investigated the formation energies of different substitutional silicon defects.[310] They found that the formation energy of the defect whereby silicon substitutes for O (Si_O) is very high, rendering it unlikely to be found. Their calculations showed that silicon prefers to substitute for zinc (Si_{Zn}) in the bulk, as well as at grain boundaries, due to the lower defect formation energy.

Wu *et al.* performed a deeper study, whereby they compared the formation energies of both substitutional and interstitial silicon defects.[311] They also found that the formation energy of Si_{Zn} is lower than the formation energy of Si_O, as well as the formation energies of tetrahedrally and octahedrally co-ordinated interstitial silicon ($Si_{i(tet)}$ and $Si_{i(oct)}$, respectively). Hence, increasing the concentration of silicon will result in silicon preferentially substituting for zinc. This is reflected in the contraction in the unit cell volumes (Figure 4.2).

The unit cell volumes for the films were calculated with a Le Bail refinement, using GSAS and EXPGUI. With increasing silicon concentration, the unit cell volumes of the SZO films decreased linearly, due to the smaller radius of the silicon ions in comparison to Zn^{2+}.[309] As a substitutional defect, it causes a contraction in the unit cell. The linear reduction in unit cell volume suggests that the amount of silicon incorporated into the film was strongly dependant on the initial silicon concentration used in the precursor solution. Rashidi *et al.* also noted a decrease in unit cell volume for their SZO film deposited *via* spray pyrolysis, in comparison to their undoped ZnO film deposited using the same conditions.[307]

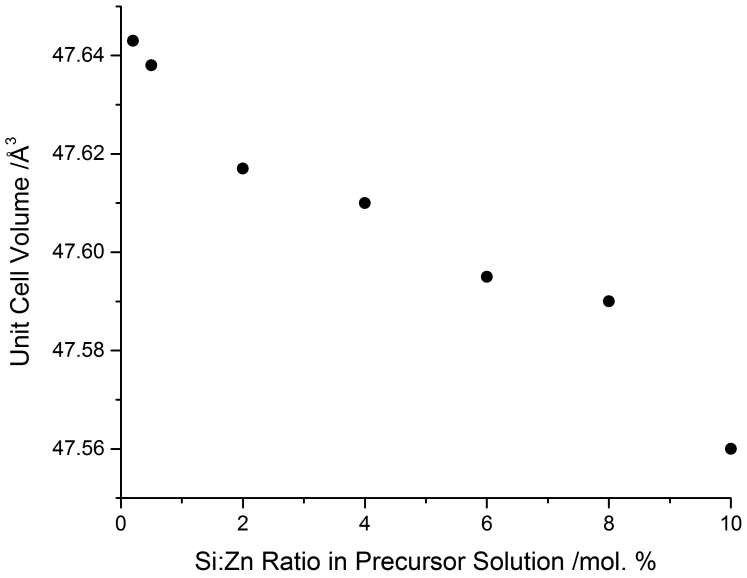

Figure 4.2: Unit cell volumes of the SZO films deposited *via* AACVD.

4.2.4 *Elemental Analysis*

Carbon contamination was observed at the surfaces of the films, and within the bulks, due to the inefficient breakdown of $Zn(acac)_2$.

The zinc 2p regions revealed the same peak splitting and binding energies observed for the zinc peaks in Chapter 3, corresponding to Zn^{2+}. This indicates that no secondary Zn-Si-O phases were formed.

The presence of silicon in the films was also confirmed by XPS. The silicon 2p peaks consistently had a splitting of 0.60 eV, which is a typical value for this orbital (Figures 4.3a and 4.3b).[312–314] The binding energies of the silicon $2p_{3/2}$ and $2p_{1/2}$ peaks were at 102.6 eV ($\pm$ 0.2 eV) and 103.2 eV ($\pm$ 0.2 eV), which corresponds to Si^{3+}.[315,316] No peaks corresponding to Si^{4+} at 104.1 eV were observed.[302,306] This indicates that the silicon was acting as a single donor, rather than a double donor, and most likely existed as Si^{3+}. Similar results have been observed previously.[17,302,306] Clatot *et al.* deposited SZO films *via* PLD.[302] They assigned the silicon 2p peak at 102.4 eV to Si^{3+}. Similarly,

Yuan *et al.* deposited SZO films *via* ALD.[306] They assigned the silicon 2p peak at 102.9 eV to Si^{3+}. They both explained the presence of this peak by the fact that silicon was acting as a single donor, rather than a double donor. In addition, no peaks corresponding to elemental silicon at 99.6 eV were observed.[317–319]

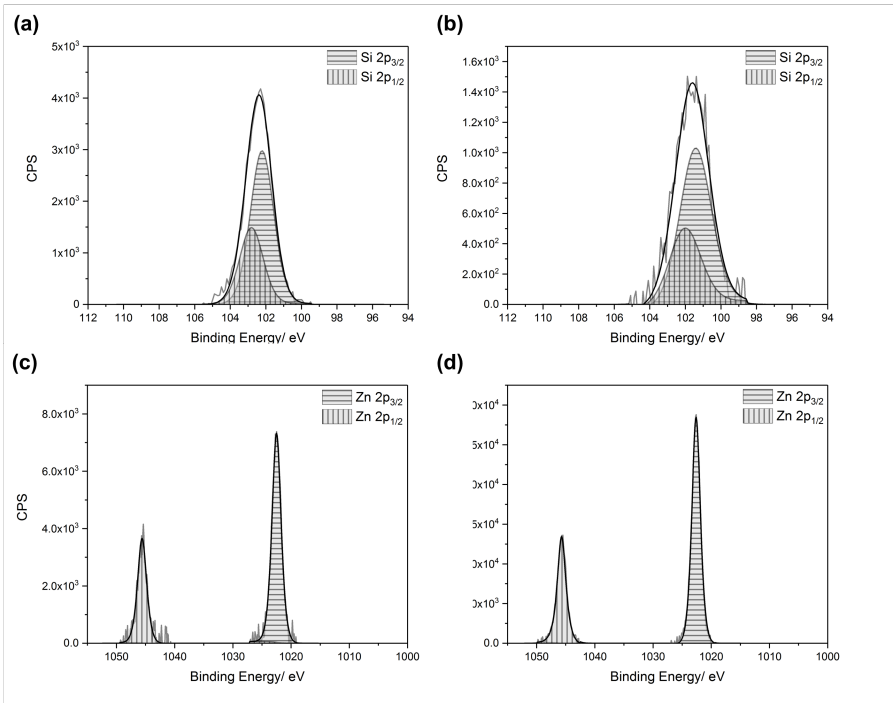

Figure 4.3: XPS spectra for the 10 mol% SZO film deposited *via* AACVD, showing the (a) silicon 2p peaks at the film surface, (b) silicon 2p peaks in the bulk of the film, (c) zinc 2p peaks at the film surface, and (d) zinc 2p peaks in the bulk of the film.

The concentration of silicon in the SZO films was highly dependant on the amount used in the precursor solution (Figure 4.4). The films were etched to compare the dopant concentration at the surfaces and in the bulks. Similar to the AZO, GZO, and IZO films of Chapter 3, the dopant is segregated towards the surface of the film. Moreover, the difference in silicon concentration between the surfaces and the bulks was more significant than the segregation observed for the AZO films. It is apparent that increasing the silicon concentration in the precursor solution only led to a minor increase in the dopant concentration in the bulk of film. However, it did lead to a significant

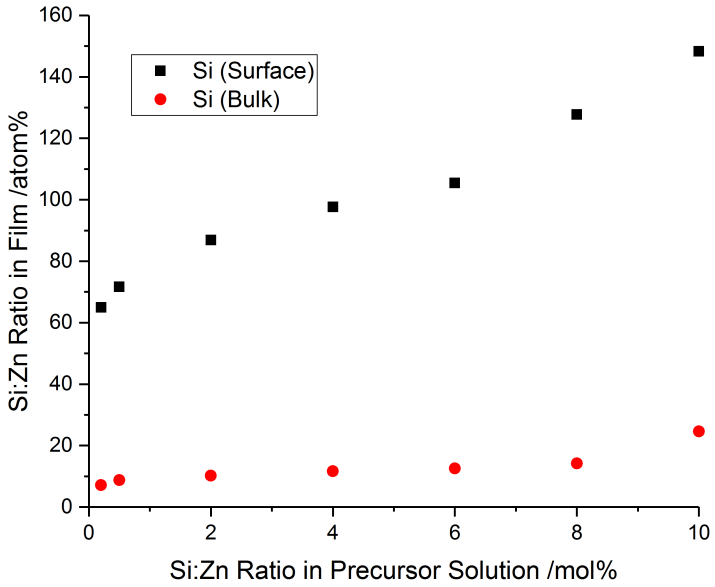

Figure 4.4: Si:Zn ratios at the surfaces and in the bulks of the SZO films deposited *via* AACVD, as determined by XPS.

increase in surface segregated silicon. The reason for this could be that silicon has an even smaller ionic raidus in comparison to aluminium, which means it should be able to diffuse through the lattice to the surface with relative ease.[303] The silicon that segregates at the grain boundaries will form SiO_2, which is electrically inactive, and as such, it causes a deterioration in the electrical properties of the films.[300,301] This secondary SiO_2 phase is amorphous and low in concentration, so it is not detectable by XRD.[17]

4.2.5 *Surface Morphology*

The morphologies of the SZO films did not vary much when the silicon concentration was increased (Figure 4.5). The largest grains were observed for the 2 mol% SZO films. Yuan *et al.* stated that high concentrations of amorphous SiO_2 at grain boundaries obstruct crystal growth and result in smaller grain sizes.[306]

The grains were approximately 1–2 μm in diameter. The films all displayed clearly-defined hexagonal plates, similar to the undoped ZnO film (Figure 3.11). The 0.5 mol% SZO film was almost indistinguishable from the undoped ZnO film, in terms of grain shape, size, and distribution. This all suggests that the silicon does not have a significant effect on the growth mechanism of the films, particularly at low silicon concentration.

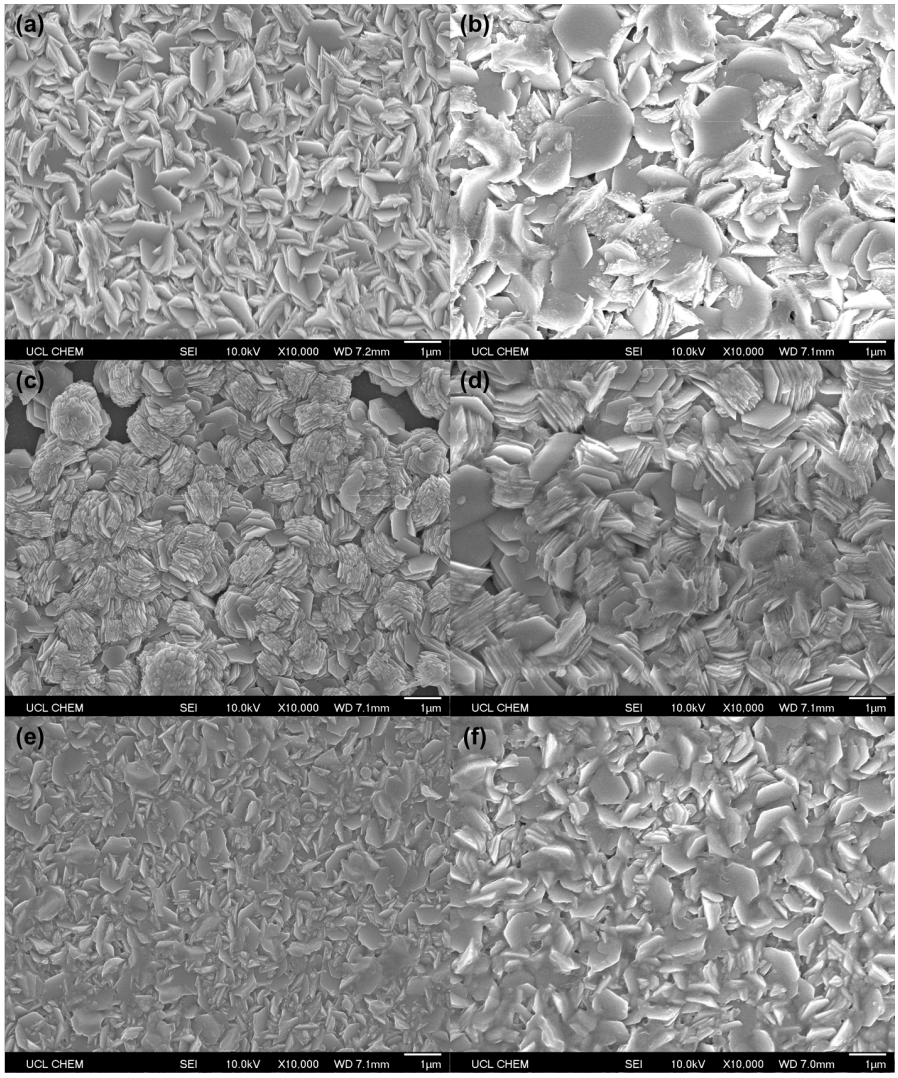

Figure 4.5: SEM images of (a) 0.5 mol%, (b) 2 mol%, (c) 4 mol%, (d) 6 mol%, (e) 8 mol%, and (f) 10 mol% SZO films deposited *via* AACVD.

The SEM images also revealed the growth mechanism of the grain structure (Figure 4.6). In the centre of several grains, smaller hexagonal layers can be seen. This indicates that, at a certain point,

the grains stop growing laterally, and instead, fresh precursor reacts and grows from the centres of the upper surface of the grains. It is a fair assumption that if these smaller surface layers had been supplied with more precursor, they would have continued to grow to another full-sized layer. However, the depletion of the precursor solution resulted in incomplete growth of some of these layers. ZnO has a hexagonal crystal structure, thus the observation of hexagonal grains indicates high quality crystallite growth.

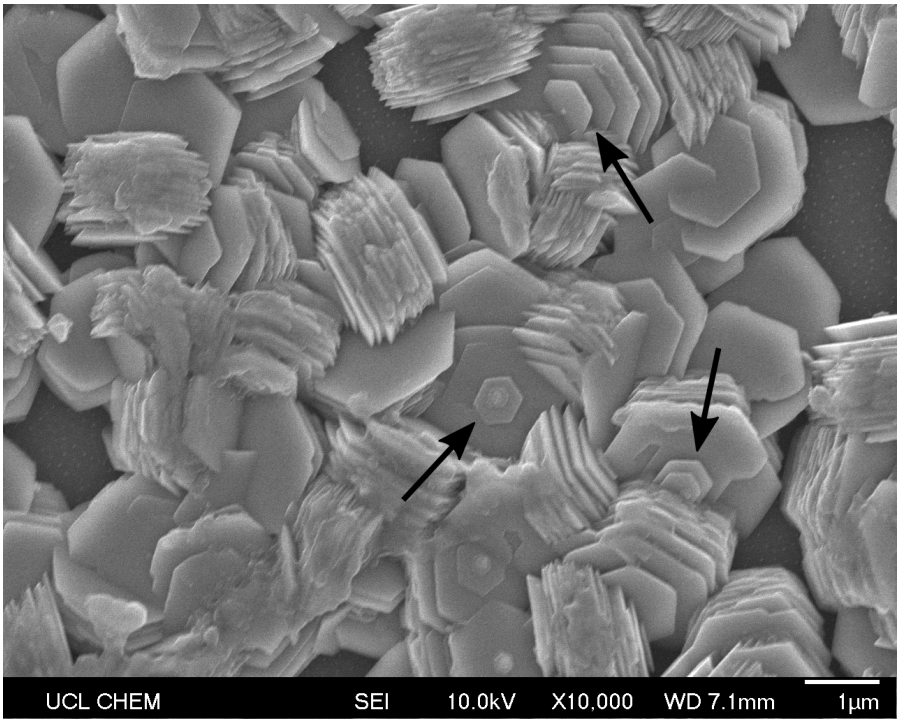

Figure 4.6: SEM image of 6 mol% SZO film deposited *via* AACVD. Arrows have been used to indicate some obvious examples of the layered, hexagonal growth mechanism.

Rashidi *et al.* deposited SZO films *via* spray pyrolysis — a technique that is closely related to AACVD.[307] Their films were also deposited using $Zn(acac)_2$ as the zinc precursor, at a deposition temperature of 450 °C. Thus, their SZO films are a fair comparison to the films described in this chapter. Their 3 mol% SZO film clearly shows a very similar hexagonal, layered grain structure. However, because the film was deposited *via* spray pyrolysis, the grains are approximately 10

times smaller than the films deposited *via* AACVD. This is a result of the shorter residence time that the precursor solution experiences prior to reaching the substrate in a spray pyrolysis deposition, in comparison to AACVD. With spray pyrolysis, the precursor solution is sprayed directly at a heated substrate, whereas in AACVD, the precursor solution is passed more gently over the substrate, which allows more time for molecular mixing, and the agglomeration of droplets. This has led to larger grain sizes, which is beneficial for TCO applications, as it will minimise grain boundary scattering and improve transport properties.

4.2.6 *Optical Properties*

All of the as-deposited SZO films were visibly transparent. The average transmittance across the visible part of the spectrum fluctuated between 72–80% (Table 4.2).

Table 4.2: Optical properties of SZO films deposited *via* AACVD.

Film	$T_{\lambda 400\text{-}700}$ /%	Band gap /eV ($\pm$ 0.01eV)
0.2 mol% SZO	75	3.19
0.5 mol% SZO	72	3.18
2 mol% SZO	73	3.19
4 mol% SZO	75	3.19
6 mol% SZO	80	3.20
8 mol% SZO	76	3.18
10 mol% SZO	77	3.09

The general trend was an increase in transmittance with silicon concentration. The outlier of this trend was the most transparent film, 6 mol% SZO, which had an average visible transmittance of 80%, thus achieving the requirement for commercial TCO applications. All of the SZO films were 1 μm thick. Hence, the variation in optical

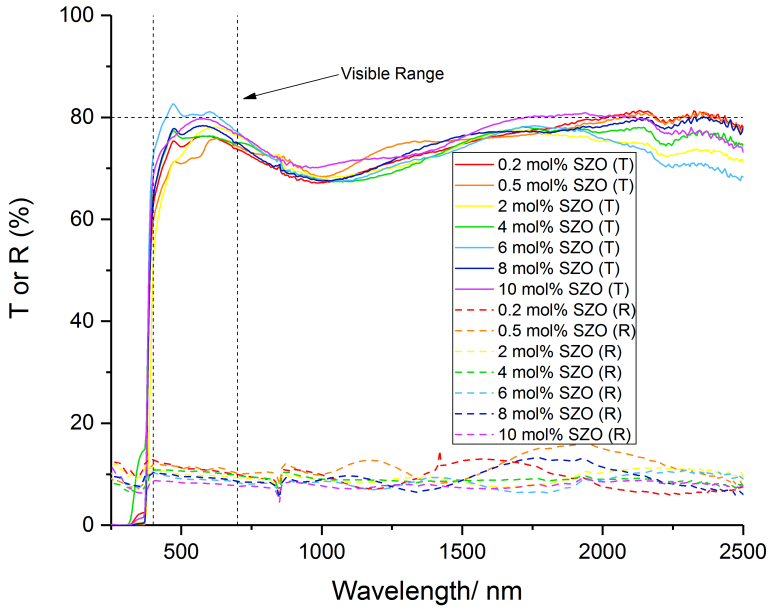

Figure 4.7: Transmission-reflectance spectra for SZO films deposited *via* AACVD.

transmittance was not due to thickness-related absorption. Instead, the reason for the higher transmittance of the 6 mol% SZO film may be due to its wider band gap.

The transmission-reflectance spectra for the SZO were fairly consistent across the scanned wavelengths (Figure 4.7). The AZO, GZO, IZO, AGZO, IGZO, and AIZO films from the previous chapter generally all showed a decrease in transmittance at longer wavelengths (Figures 3.13, 3.14, 3.15, and 3.18). Conversely, the SZO films retained their high transmittance at longer wavelengths, similar to the undoped ZnO film.

4.2.7 *Electrical Properties*

The electrical properties of the films were determined using the van der Pauw technique, and are summarised in Table 4.3. The 10 mol% SZO film was too resistive to be able to obtain any electrical

properties. This could be due to the relatively high concentration of insulating SiO_2 at the grain boundaries, which would act as an electron trap, resulting in a lower carrier concentration. Additionally, the higher incorporation of Si^{3+} could lead to an increase in impurity scattering.

Table 4.3: Electrical properties of SZO films deposited *via* AACVD.

Film	Resistivity /$\times 10^{-2}$ Ω·cm	Carrier concentration /$\times 10^{19}$ cm^{-3}	Mobility /cm^2/V·s
0.2 mol% SZO	24.0	0.4	5.9
0.5 mol% SZO	11.7	1.1	4.7
2 mol% SZO	2.1	2.5	11.9
4 mol% SZO	2.0	2.6	16.5
6 mol% SZO	2.5	1.6	15.1
8 mol% SZO	8.1	1.0	7.6
10 mol% SZO	N/A	N/A	N/A

Even with a very low concentration of silicon (0.2 mol%), the resistivity improved significantly, compared to the undoped ZnO, which was non-conductive. However, the resistivity at low silicon concentration was still quite high, on the order of 10^{-1} Ω·cm.

Analogous to the AZO, GZO, and IZO films from the previous chapter, the resistivity decreased initially, by increasing the dopant concentration in solution. This is due to silicon ions donating electrons to the conduction band.

Wu *et al.* determined that Si_{Zn} is a shallow donor, whereas the interstitial defects $Si_{i(tet)}$ and $Si_{i(oct)}$ are deep donors.[311] This was confirmed by Chowdhury *et al.*, who also found that the Si_O defect is a deep acceptor.[320] Therefore, only Si_{Zn} will provide significant charge density to the conduction band. Wu *et al.* also calculated that, for interstitial silicon, a heavier effective mass will be observed, leading to a reduction in carrier mobility. Furthermore, the presence of interstitial silicon will reduce the transmittance of the SZO.[311]

Kuznetsov *et al.* explained that at high silicon concentrations, a solubility limit will be reached for the substitutional sites, which will lead to an increase in interstital silicon, despite the higher formation energy.[300] This will cause a deterioration in electrical properties, because interstitial defects generally form donor states that are too deep in the band gap to contribute any significant electron density to the conduction band.[250] Moreover, interstitial defects act as neutral scattering centres which reduce carrier mobility. Additionally, high silicon concentrations can result in the precipitation of secondary insulating phases, such as SiO_2. This typically happens at grain boundaries, which are disordered, oxygen-rich regions. As a result, they are dominated by defects that can trap electrons.[300] The silicon that forms oxide bonds remains electrically inactive, and does not contribute electrons to the conduction band. These insulating phases are amorphous and are low in concentration, so they are not detectable by XRD.[17]

This explains the reduction in carrier concentration at higher dopant concentrations (>4 mol%). The emergence of defects and secondary phases results in electron traps. This will lead to a reduction of electrons which are free to carry charge, and consequently, to an increase in resistivity.

Rashidi *et al.* deposited SZO films *via* spray pyrolysis, using $Zn(acac)_2$ as the Zn precursor, at a deposition temperature of 450 °C.[307] They saw an increase in resistivity for their films with >3 mol% silicon in solution, which agrees with the findings in this chapter. Similarly, Kuznetsov *et al.* and Yuan *et al.* found that their electrical properties deteriorated with silicon concentrations >2 at.% for their SZO films deposited *via* pulsed layer deposition and atomic layer deposition, respectively.[300,306] Thus, the deterioration of electrical properties appears to be a common phenomenon at

relatively low silicon concentration. This is in contrast to the AZO, GZO and IZO films from the previous chapter, whereby a 10 mol% dopant concentration resulted in minimal resistivity values (Table 3.3). This is because silicon has a limited solubility in ZnO, and high concentrations will result in interstitial defects, and segregated SiO_2 at grain boundaries.[300,306,307]

4.3 CO-DOPING SILICON WITH FLUORINE

Co-doping a TCO material with fluorine to further improve the conductivity is a method which has been employed previously. Ponja *et al.* deposited thin films of doped zinc oxide *via* AACVD.[189] Their AZO film had a resistivity of 2.15 $\times 10^{-3}$ Ω·cm. However, they found that co-doping with aluminium with fluorine resulted in a decrease in resistivity, down to 1.85 $\times 10^{-3}$ Ω·cm. Similarly, Rashidi *et al.* deposited SZO and fluorine/silicon co-doped zinc oxide (FSZO) thin films *via* spray coating.[321] The optimised resistivity achieved for their SZO films was ~4.8 $\times 10^{-3}$ Ω·cm. They found that co-doping with fluorine led to a decrease in resistivity, down to ~1.5 $\times 10^{-3}$ Ω·cm. This is the only instance in the literature describing the synthesis of FSZO.

This section describes the first time that FSZO thin films have been deposited *via* AACVD.

4.3.1 *Experimental*

The deposition conditions from the previous section were maintained for the depositions in this section. Tetraethyl orthosilicate (TEOS) was used as the silicon precursor, at a concentration of 5 mol% relative to zinc. Ammonium fluoride

[NH_4F] was used as the fluorine source, with concentration ranging from 5–100 mol% relative to zinc.

4.3.2 *Film Synthesis*

Fluorine/silicon co-doped ZnO thin films were synthesised, based on the following reaction:

$$Zn(acac)_{2\,(g)} + xSi(OC_2H_5)_{4\,(g)} + yNH_4F_{\,(g)} \xrightarrow{\Delta} Si_xF_yZn_{1-x}O_{1-y\,(s)}$$

All of the as-deposited films were of high quality, and showed a high adherence to the glass substrates. The films passed the Scotch tape test, and resisted being scratched with a steel scalpel.

The films were visibly transparent, and had visible interference patterns. The highest quality regions in terms of coverage and uniformity were found nearest to the baffle. For this reason, these regions were characterised.

4.3.3 *Crystal Structure*

All of the as-deposited films consisted of pure wurtzite ZnO (Figure 4.8). No secondary phases were observed, even at high dopant concentrations.

When 5 mol% fluorine was used in the precursor solution, a preferential orientation in the (002) direction was observed. This is analogous to the AZO, GZO, and SZO films described previously. However, upon increasing the fluorine concentration, the preferential orientation shifted from the (002) direction to the (101) direction. Thus, it appears that fluorine promotes growth in the (101) direction.

This phenomenon has been observed previously. Rashidi *et al.* found that the preferred orientation of their FSZO films deposited

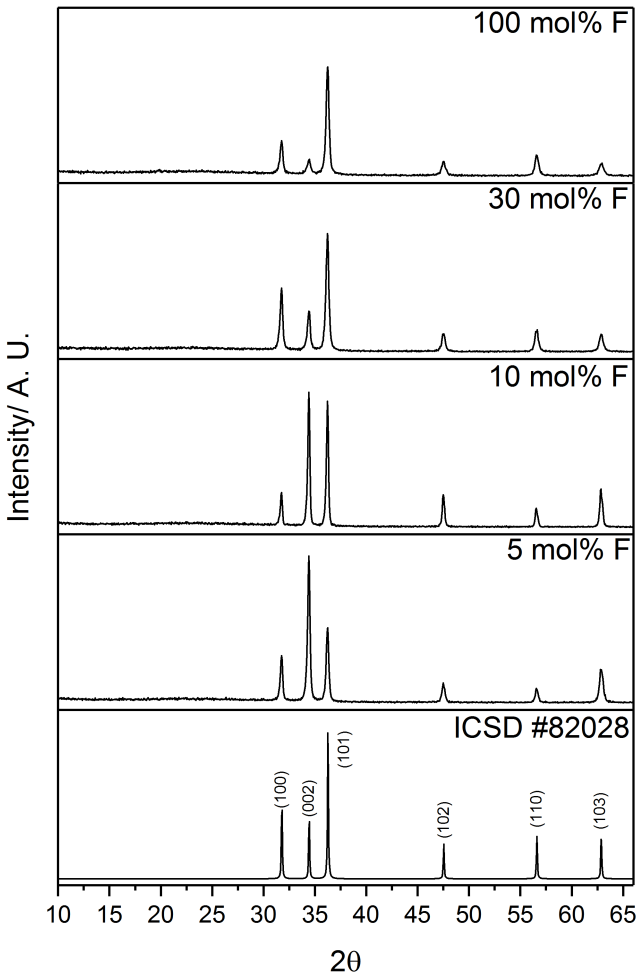

Figure 4.8: X-ray diffraction patterns of the FSZO films deposited *via* AACVD. The silicon concentration was maintained at 5 mol% relative to zinc. A diffraction pattern of ZnO from ICSD #82028 is also included for reference.

via spray pyrolysis changed from the (002) direction to the (101) direction with increasing fluorine concentration. Similarly, Ponja *et al.* observed that their AZO film deposited *via* AACVD had a typical (002) preferred orientation.[189] However, upon co-doping with fluorine, the intensity of the (002) diminished significantly, and a preferential orientation was observed in the (101) direction. Additionally, their fluorine-doped zinc oxide (FZO) film showed a strong preferred orientation in the (101) direction, with only a very low intensity (002)

peak. Olvera *et al.* also noted a significant decrease in the relative intensity of the (002) peak with increasing fluorine concentration for their FZO films deposited *via* spray pyrolysis.[322] This was also observed by Yakuphanoglu *et al.*, for their FZO films deposited *via* spray pyrolysis.[323]

Furthermore, a slight decrease in overall peak intensity can be observed at high fluorine concentration. Yakuphanoglu *et al.* observed the same trend for their FZO films, and attributed it to a deterioration in crystallinity due to fluorine incorporation.[323]

4.3.4 *Elemental Analysis*

Carbon contamination was observed at the surfaces and within the bulks of the films, due to the inefficient thermal decomposition of $Zn(acac)_2$.

The concentration of fluorine in the films was very low. For most of the films, it was below the detection limits of XPS. Only upon using 100 mol% fluorine relative to zinc, was the fluorine 1s peak observable by XPS (Figure 4.9). The peak that emerged at 685 eV can be attributed to the F–Zn bond.[324] This confirms that fluorine substituted for oxygen, in contrast to aluminium, gallium, indium, and silicon, which all substituted for zinc.

Low levels of fluorine incoporation are typically observed when fluorine is used as a dopant for SnO_2 or TiO_2.[45,112,290] However, despite the low concentration, fluorine can have a significant effect over the properties of the films. On top of this, the XPS data revealed that there had been a significant increase in the incorporation of silicon (Figure 4.10). The silicon concentration remained constant in the precursor solution at 5 mol% relative to zinc, so the visible increase in silicon

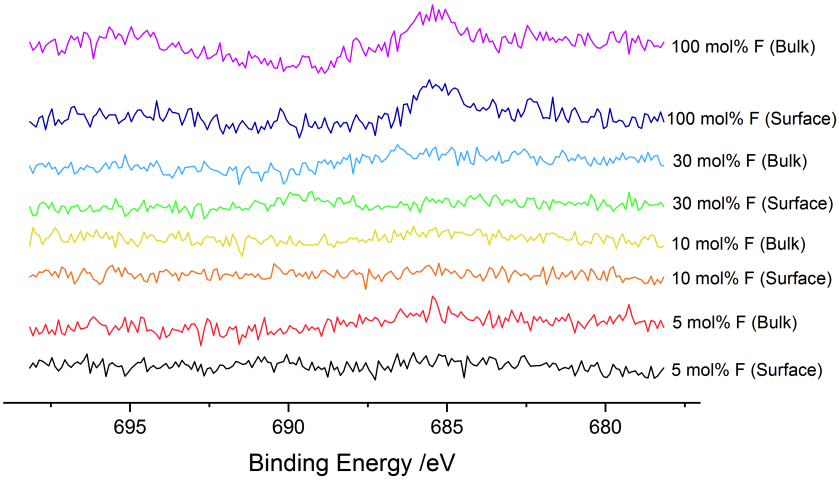

Figure 4.9: Surface and bulk XPS scans of the fluorine 1s orbital for the FSZO films deposited *via* AACVD.

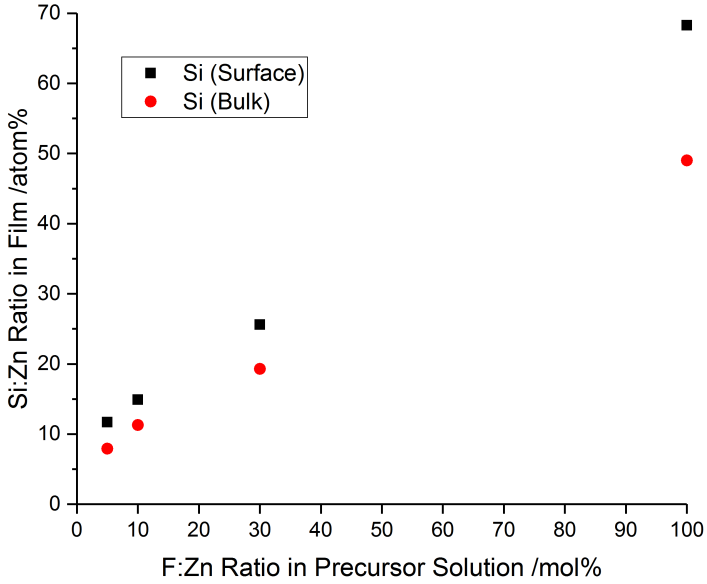

Figure 4.10: Si:Zn ratios at the surfaces and in the bulks of the FSZO films deposited *via* AACVD, as determined by XPS. Note that the Si:Zn ratio in the precursor solution remained constant at 5 mol%.

incorporation in the FSZO films was due to the increase in fluorine concentration in the precursor solution.

Rashidi *et al.* observed the same phenomenon for their FSZO films deposited *via* spray pyrolysis.[321] They reported that the formation of

SiF_6^{2-} in solution reduced the concentration of silicon oxy and silicon hydroxy species which would otherwise be free for self-condensation reactions. These reactions would result in oligomeric silicon species, which are less active for doping. Therefore, instead of acting as a dopant in its own right, fluorine modifies the solution behaviour of the silicon-containing species, to allow for more of it to be incorporated into the film.

It can be seen that co-doping with fluorine has resulted in a higher level of silicon incorporation in comparison to the SZO analogues (Figure 4.4). Additionally, it has resulted in a reduction in surface segregation.

4.3.5 *Surface Morphology*

The surface morphologies of the FSZO films appeared to be strongly dependant on the fluorine concentration (Figure 4.11). Since XPS indicated that fluorine was only present in the films at very low concentrations, the fluorine may be affecting the growth mechanism by pre-reactions in solution.

The film deposited using 5 mol% fluorine displayed a morphology that consisted of grains that, for the most part, did not have defined shapes. The typical, layered, hexagonal grains can also be seen scattered amongst these "rod-like" structures. Rashidi *et al.* also noted a changed in surface morphology for their FSZO films, compared to their SZO films deposited *via* spray pyrolysis.[321] Their SZO film consisted of a hexagonal grain structure. However, upon co-doping with fluorine, the shapes of these grains became less well-defined.

Increasing the fluorine concentration to 10 mol% resulted in more sharply-defined layered, hexagonal plates. These grains were

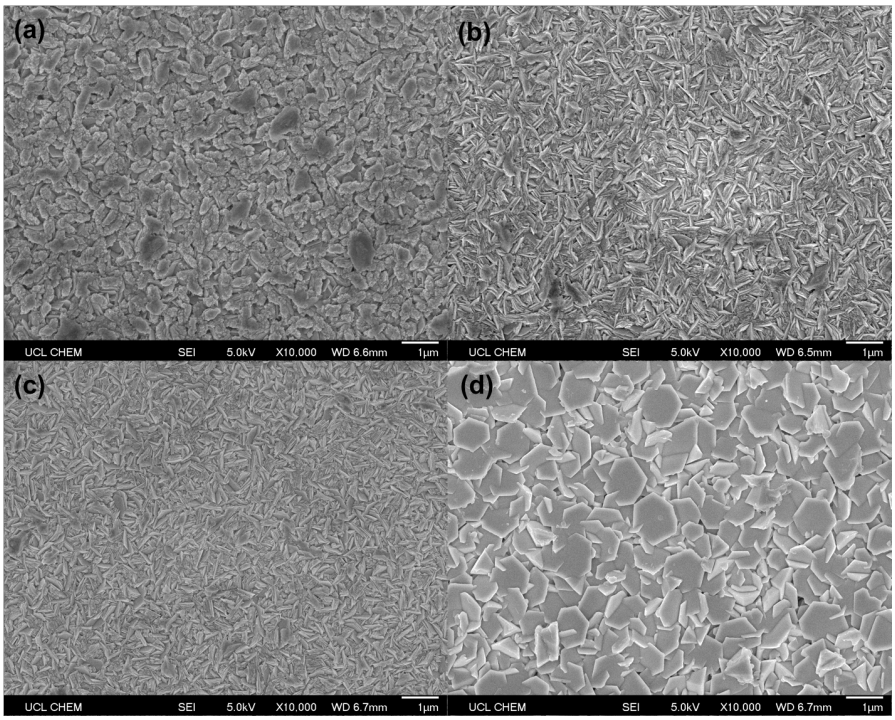

Figure 4.11: SEM images of the FSZO films deposited *via* AACVD, using (a) 5 mol%, (b) 10 mol%, (c) 30 mol%, and (d) 100 mol% fluorine. The silicon concentration was maintained at 5 mol% relative to zinc.

randomly oriented. This reflects the XRD data for this film (Figure 4.8), in which the (002) peak and the (101) are very similar in terms of intensity. This suggests that this film did not have such a preferred orientation, and that the crystallites are more randomly oriented.

The film deposited using 30 mol% fluorine had a surface morphology that was almost identical to the film deposited using 10 mol% fluorine, except that more of the surfaces of the grains are visible. This may indicate the return of preferred orientation, as shown in the XRD pattern.

The most extreme change in surface morphology was observed for the film deposited using 100 mol% fluorine, relative to zinc. This film consisted of large, hexagonal plates which were highly ordered, with their surfaces facing upwards. Again, this indicates the high level of preferred orientation for this film, which agrees with the XRD data, which shows significant preferred orientation in the (101) direction.

The observable variation in surface morphology indicates that F is having an effect on the growth of the film.

Pawar *et al.* deposited FZO films *via* spray pyrolysis, using zinc acetate (similar to $Zn(acac)_2$) and ammonium fluoride as their precursors.[325] They did not observe such a drastic change in surface morphology with fluorine concentration. Their FZO films had dense morphologies, with small (<100 nm), spherical grains. This is due to the spray pyrolysis technique, in which the precursor solution is sprayed directly at the heated substrate, and hence there is less time for precursors to diffuse and form the intricate grain structures observed in the films deposited *via* AACVD.

4.3.6 *Optical Properties*

All of the as-deposited FSZO films were visibly transparent. Increasing the fluorine concentration from 5 mol% to 10 mol% in the precursor solution led to an increase in visible transmittance (Figure 4.12). Increasing the fluorine concentration further to 30 mol% did not affect the visible transmittance. When 100 mol% fluorine was used, the visible transmittance decreased again.

Table 4.4: Optical properties of FSZO films deposited *via* AACVD.

Film	$T_{\lambda 400\text{-}700}$ /%	Band gap /eV ($\pm$ 0.01eV)
5 mol% F	75	3.24
10 mol% F	83	3.26
30 mol% F	83	3.25
100 mol% F	75	3.25

The XPS data revealed that the fluorine concentration in the film remained low (Figure 4.9). However, increasing the fluorine concentration in solution led to an increase in the incorporation of silicon (Figure 4.10). Thus, the change in optical properties is likely

due to silicon. The initial increase in transmittance may be a result of a widening of the optical band gap, due to the Burstein-Moss effect. The eventual reduction in transmittance could be due to the band gap narrowing effect. It could also be a result of the high concentration of silicon in the film, which led to the creation of a high concentration of colour centres.[7]

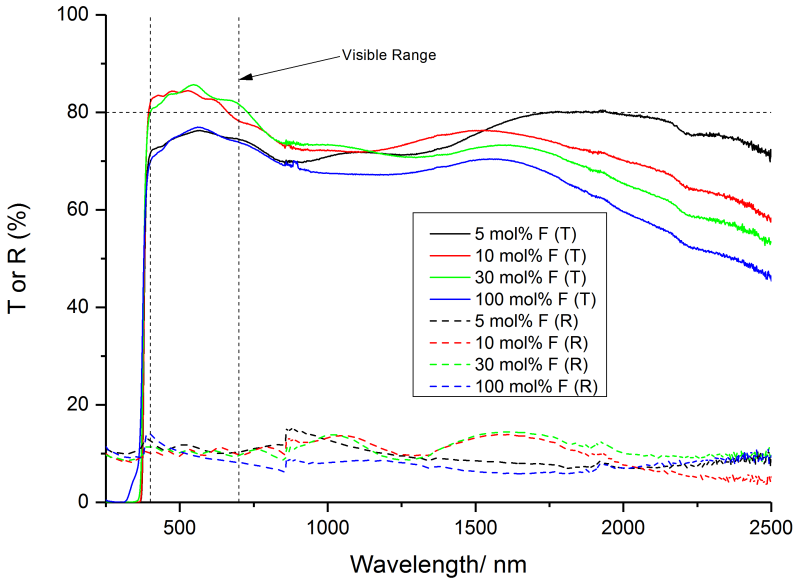

Figure 4.12: Transmission-reflectance spectra for FSZO films deposited *via* AACVD.

With regards to the band gaps of the films, which were calculated from Tauc plots, no significant difference was observed (Table 4.4). However, a case could be made that a very small band gap widening is observed by increasing the fluorine concentration from 5 mol% to 10 mol%. This would be due to the Burstein-Moss effect. Further increasing the fluorine concentration led to a small band gap narrowing. The band gaps of the FSZO films are wider than the SZO films (Table 4.2). This could be due to the higher incorporation of Si^{3+}, which resulted in a higher carrier concentration, thus raising the

Fermi level higher than the maximum position possible by doping with silicon only.

4.3.7 *Electrical Properties*

The electrical properties of the FSZO films are summarised in Table 4.5. All of the films displayed *n*-type conductivity, with electrons as the majority charge carriers. The most conductive FSZO film was the film deposited using 5 mol% fluorine in the precursor solution. This film had a resistivity of 2.8 $\times 10^{-2}$ Ω·cm, which is higher than the most conductive SZO films.

Table 4.5: Electrical properties of FSZO films deposited *via* AACVD.

Film	Resistivity / $\times 10^{-2}$ Ω·cm	Carrier concentration / $\times 10^{19}$ cm^{-3}	Mobility /cm^2/V·s
5 mol% F	2.8	7.8	2.8
10 mol% F	6.9	3.0	3.1
30 mol% F	8.3	2.0	1.8
100 mol% F	N/A	N/A	N/A

Since there is less surface segregation of the silicon in the FSZO films compared to the SZO films, grain boundary scattering alone cannot account for the deterioration in conductivity. The reason for the higher resistivity of the FSZO films could simply be that the concentration of silicon in the FSZO films is too high, and is leading to impurity scattering.

Rashidi *et al.* reported that the electrical properties of their FSZO films deposited *via* spray pyrolysis were superior than their SZO films.[321] The resistivities of their FSZO films showed a threefold improvement in conductivity in comparison to their SZO films, with resistivities of ~1.5 $\times 10^{-3}$ Ω·cm and ~4.8 $\times 10^{-3}$ Ω·cm, respectively.

These values are superior to the FSZO films described in this chapter. However, their FSZO films also showed inferior optical properties.

4.4 CONCLUSIONS

AACVD has been used to deposited silicon-doped zinc oxide thin films on glass substrates, at dopant concentrations ranging from 0.2 mol% to 10 mol% relative to zinc in solution. All of the films were of high quality, with a high adherence to the substrate. Just as with the films deposited in the previous chapter, wurtzite ZnO was the only phase present in the XRD patterns. SEM images revealed the layered growth mechanism of the grain structure. The films were highly transparent, with up to 80% visible transmittance. Additionally, silicon was shown to be an effective dopant element, by improving the electrical properties of the films, compared to the non-conductive undoped ZnO film. A minimum resistivity of 2×10^{-2} Ω·cm was obtained for the 4 mol% SZO film. Although this was not as low as the 10 mol% AZO film, this film also displayed a mobility of 16.5 $cm^2/V{\cdot}s$, which was higher than any of the films from Chapter 3.

It was also found that co-doping Si with fluorine affected the properties of the films, by allowing more silicon to be incorporated into the film. Therefore, co-doping with fluorine can be used to increase the uptake of silicon into the film. This means that a lower concentration of the silicon precursor should be able to achieve similar improvements in the optoelectronic properties of ZnO. Increasing the concentration of fluorine promoted crystal growth in the (101) direction. Additionally, a high fluorine concentration led to a dramatic change in surface morphology, resulting in a grain structure consisting of large, hexagonal plates. These plates were highly ordered, with their surfaces facing upwards, away from the

substrate. The band gaps of the FSZO films were larger than those of the SZO films, which led to higher visible transmittance. However, the minimum resistivity of the FSZO films was higher.

5

ZINC ANTIMONATE THIN FILMS DEPOSITED *VIA* SPIN COATING

This chapter first focuses on attempts at depositing zinc antimonate thin films *via* AACVD. Following this, it describes zinc antimonate thin films which were successfully deposited *via* spin coating.

5.1 INTRODUCTION

Zinc antimonate [$ZnSb_2O_6$] is a material which has not been investigated as extensively as zinc oxide. It was first identified in a mineral extracted from tin ores mined in Mexico in the 1940s.[326]

Over half a century later, Nishiyama *et al.* became the first group to report that $ZnSb_2O_6$ exhibits *n*-type semiconductivity, due to inherent oxygen vacancies.[327] Following this, Matsushima *et al.* calculated the band structure of $ZnSb_2O_6$.[328] They found that the lower conduction band consists mainly of antimony 5s and oxygen 2p antibonding states. They also predicted a high carrier mobility in $ZnSb_2O_6$, due to the high dispersion, or band width, in the lower conduction band. A larger band width is related to a greater overlap of adjacent orbitals, and leads to more delocalised states than a narrow band.[5,329] Thus, a large band width or dispersion leads to superior electrical properties.

$ZnSb_2O_6$ crystallises in the trirutile structure, with zinc and antimony atoms octahedrally coordinated by six oxygen atoms in each rutile unit.[330] The edge-sharing octahedra that make up the crystal structure are a contributing factor towards high carrier

mobility. Kawazoe *et al.* stated that, in these rutile chains, because there is no intervening oxygen between the metal cations, the M–M bond distance is short. This results in direct overlap of the s orbitals of neighbouring metal cations. Consequently, there is a large dispersion of the conduction band, which subsequently results in high carrier mobility.[331] The promising electrical properties, coupled with its wide band gap (reported as being ~3.0–3.35 eV)[328,332–335] make $ZnSb_2O_6$ a potential TCO material.

$ZnSb_2O_6$ is typically synthesised in micropowder or nanopowder form. It has been prepared *via* solid state synthesis,[327,334] co-precipitation synthesis,[333,336] sol-gel synthesis,[330] and microwave assisted colloidal synthesis.[337,338]

There have been few reports on the deposition of $ZnSb_2O_6$ thin films. Tamaki *et al.* deposited $ZnSb_2O_6$ films on alumina substrates *via* dip coating.[339] Choi *et al.* made a paste from $ZnSb_2O_6$ nanoparticles, and deposited a film on FTO-coated glass substrates using a Doctor Blade.[335] Zhu *et al.* used the same technique, but their paste was made using a mixture of Sb_2O_3 and ZnO nanoparticles, and they deposited their films onto Al_2O_3 substrates.[340] Additionally, the literature has previously focused on gas sensing and photocatalytic applications for $ZnSb_2O_6$. This chapter describes the first attempt to exploit its potential for TCO applications.

5.2 ATTEMPTS AT ZINC ANTIMONATE THIN FILMS *VIA* AACVD

5.2.1 *Experimental*

The equipment for AACVD was set up as described in Section 2.2. A 2 cm^2 quartz square was used as the substrate, and was heated to 550 °C. Compressed air was the carrier gas, with a flow rate of 1 L

min^{-1}. $Zn(acac)_2$ was used as the zinc precursor, due to its low cost and stability, and antimony ethoxide [$Sb(OEt)_3$] was used as the antimony precursor, as it is relatively stable and commercially available. The Zn:Sb ratio in MeOH was 1:2.

It was found that stirring $Zn(acac)_2$ and $Sb(OEt)_3$ together in MeOH in a 1:2 ratio for 30 mins resulted in the formation of a white precipitate. Balasubramaniam *et al.* synthesised $ZnSb_2O_6$ nanoparticles by stirring two very similar precursors (zinc acetate, and antimony trichloride) in MeOH for 30 mins.[333] Therefore, the white precipitate was identified as $ZnSb_2O_6$. A particulate solution is unsuitable for AACVD, as the particles will not be transported to the reactor.

For this reason, dual source AACVD was used. In this technique, two bubblers are used, each with their own humidifier. Two precursor solutions are made up, each one containing a different precursor. Two aerosol mists are generated simultaneously and transported to the reactor *via* a Y-piece connector. This prevents the reaction of the precursors in solution.

Following the deposition, the films were annealed in a muffle furnace, in air at 1000 °C for 10 hours, to allow a crystal phase to form.

5.2.2 *Results and Discussion*

Dual source AACVD successfully deposited films on the quartz substrate. The depositions were repeated several times to ensure reproducibility. The as-deposited films were optically transparent and adherent. They passed the Scotch tape test and resisted being scratched with a steel scalpel. However, the films were too resistive to be able to determine any electrical properties using the van der

Pauw technique. In addition, the resistances of the films could not be obtained using a two-point probe, which can determine resistances on the order of megaohms (MΩ). This suggests that the resistances of these films were even higher than this range.

The XRD patterns of the as-deposited films had no sharp peaks, indicating the films were completely amorphous. Amorphous films are often in a metastable state, and annealing them at high temperature can provide enough energy to rearrange the constituent atoms to form a more thermodynamically stable crystal structure. As stated above, the inherent conductivity of $ZnSb_2O_6$ is related to the overlapping of adjacent atoms in the trirutile structure. To improve the crystallinity, the films were annealed.

Improving the crystallinity can often improve the electrical properties, by providing the charge carriers with better transport pathways. An XRD pattern was recorded after the films were removed from the furnace (Figure 5.1). The XRD pattern was vastly different, as several peaks emerged. However, the peaks were not due to the formation of $ZnSb_2O_6$ or ZnO. Instead, they can partly be assigned to the quartz substrate which, unlike glass, is crystalline. This may be because the annealing process resulted in delamination of some of the film, revealing the substrate beneath. In addition, some of the minor peaks are possibly due to Sb_2O_3, Sb_2O_4, and Sb_2O_5 phases.

Despite the emergence of peaks in the XRD pattern after annealing, the films remained electrically insulating. This is because a crystalline $ZnSb_2O_6$ phase did not form. It will be necessary to improve the deposition conditions in order to deposit a conductive $ZnSb_2O_6$ film. The main obstacle is ensuring that only Sb^{5+} forms. This may prove to be difficult, as Allen *et al.* calculated that the formation energy Sb^{5+} in the form of Sb_2O_5 is higher than the formation energies of both Sb_2O_3 and Sb_2O_4.[341]

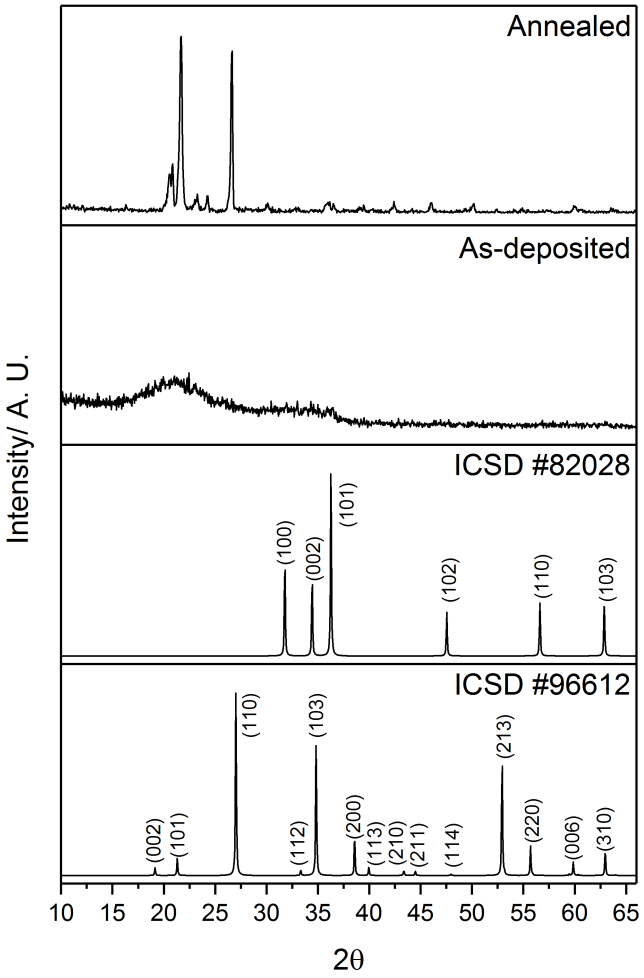

Figure 5.1: Typical X-ray diffraction patterns of as-deposited and annealed films, deposited *via* AACVD. Diffraction patterns of $ZnSb_2O_6$ from ICSD #96612, and ZnO from ICSD #82028 are also included for reference.

5.3 ZINC ANTIMONATE THIN FILMS DEPOSITED *VIA* SPIN COATING

5.3.1 *Experimental*

$ZnSb_2O_6$ nanoparticles were synthesised by stirring $Zn(acac)_2$ and $Sb(OEt)_3$ together in MeOH in a 1:2 ratio for 30 mins. For some depositions, the solvent was then removed by rotary evaporation. The white precipitate was dispersed in ink vehicles supplied by Sun

Chemical (U10197 and U9593). These ink vehicles are a mixture of various solvents. The exact composition is withheld by Sun Chemical. The resultant $ZnSb_2O_6$ dispersion was used to deposit films in a Laurell WS-650MZ-23NPPB Spin Coater.

A 2 cm^2 quartz square was used as the substrate. It was spun at 5000 revolutions per minute (RPM). A droplet of the $ZnSb_2O_6$ ink was dropped onto the substrate every 10 seconds for 5 minutes. At this point, the substrate was removed and left to dry at room temperature for an hour. Subsequently, it was annealed in a muffle furnace at 600 °C for 6 hours, in air.

5.3.2 *Results and Discussion*

The $ZnSb_2O_6$ nanoparticles were dispersed in two Sun Chemical ink vehicles (U10197 and U9593) using a tip sonicator. The inks were spin coated onto quartz substrates.

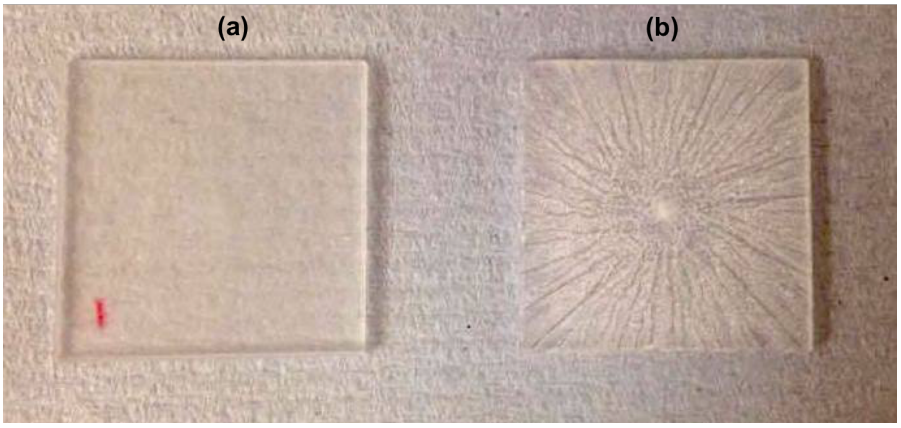

Figure 5.2: Images of as-deposited films, deposited *via* spin coating using inks of $ZnSb_2O_6$ nanoparticles dispersed in (a) U10197, and (b) U9593.

The resultant films were highly dissimilar in terms of quality (Figure 5.2). The film deposited using U10197 was more uniform, with better coverage of the substrate. In addition, it was more visibly transparent. The film deposited using U9593 had streaks and cracks across the

surface of the substrate. This may suggest that the nanoparticles were not sufficiently dispersed in U9593, which led to larger clusters that could not adhere to the substrate during the deposition process.

Lewis *et al.* observed that the quality of their spin coated PbS films improved markedly when they added polystyrene to the solution, in a 6:1 ratio with the precursors.[342] The polystyrene acted as a matrix which contains the precursors and improved their adherence to the substrate. As it is an organic compound, annealing subsequently removed the polystyrene whilst simultaneously allowing the precursors to react, forming a higher quality film. For this reason, another film was deposited from the U10197 ink vehicle, but with 600 wt.% polystyrene in solution, relative to the mass of the precursors. All of the as-deposited films had amorphous XRD patterns, with no peaks indicating a crystalline phase. After annealing at 600 °C for 6 hours, the films showed a significant improvement in terms of crystallinity (Figure 5.3a). The XRD patterns of the annealed $ZnSb_2O_6$ films revealed peaks that corresponded exclusively to trirutile $ZnSb_2O_6$. No peaks corresponding to ZnO or any other secondary phases were observed. In addition, unlike the films deposited *via* AACVD (Figure 5.1), the XRD patterns of the films deposited *via* spin coating did not show any peaks corresponding to the quartz substrate.

The presence of polystyrene in solution resulted in more intense peaks in the XRD pattern, possibly indicating an improvement in crystal quality. However, all of the films were too resistive to be able to determine their electrical properties using the van der Pauw technique. This could be due to poor film quality, with morphological defects that led to poor transport properties.

In order to see if the electrical properties could be improved, the films were fluorine-doped. $ZnSb_2O_6$ inks were made using the same

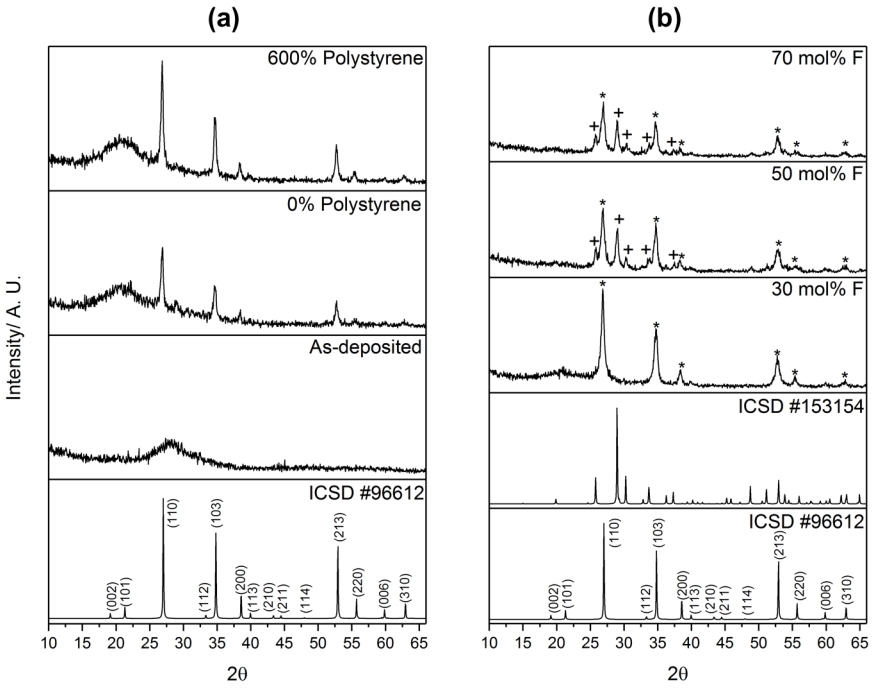

Figure 5.3: Typical X-ray diffraction patterns of (a) the as-deposited and annealed $ZnSb_2O_6$ films deposited *via* spin coating, with and without polystyrene in solution, and (b) the annealed fluorine-doped $ZnSb_2O_6$ films deposited *via* spin coating. The peaks corresponding to $ZnSb_2O_6$ (*) and Sb_2O_4 (+) have been labelled. Diffraction patterns of $ZnSb_2O_6$ from ICSD #96612, and Sb_2O_4 from ICSD #153154 are also included for reference.

method as before, with U10197 as the ink vehicle, and a 6:1 ratio of polystyrene in solution. Dopant quantities of trifluoroacetic acid (TFA) were added at the same time as the $Zn(acac)_2$ and $Sb(OEt)_3$. The fluorine concentrations used were 30 mol%, 50 mol%, and 70 mol% relative to zinc in solution. The quality of the resultant films deteriorated when the concentration of TFA in solution was increased (Figure 5.4). Higher TFA concentrations led to poorer coverage and larger gaps and cracks in the film.

The annealed fluorine-doped films were examined using XRD (Figure 5.3b). When 30 mol% fluorine was used in solution, the XRD pattern was almost identical to the undoped $ZnSb_2O_6$ film deposited using a 6:1 ratio of polystyrene in solution. Hence, using just 30 mol% fluorine in solution did not significantly affect the film. However,

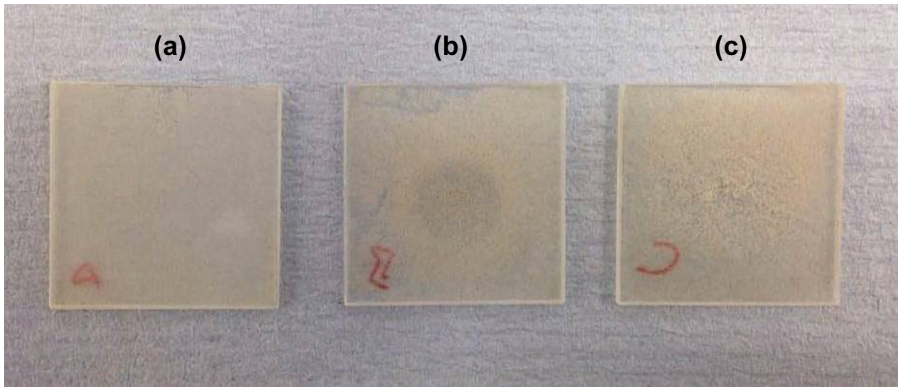

Figure 5.4: Images of annealed films, deposited *via* spin coating with (a) 30 mol%, (b) 50 mol%, and (c) 70 mol% F relative to Zn in solution.

upon increasing the fluorine concentration further, two observations were made. Firstly, the overall peak intensity decreased, possibly indicating a deterioration in crystal quality. Secondly, additional peaks emerged, which were assigned to a secondary phase of Sb_2O_4. This may be because the TFA led to the formation of F^- ions in solution, which could have reduced some of the Sb^{5+} to Sb^{3+}. Both Sb^{3+} and Sb^{5+} are present in Sb_2O_4.[343]

The fluorine-doped films were non-conductive, which could be a combination of the relatively poor quality of the morphologies, and the emergence of a secondary Sb_2O_4 phase.

The optical properties of the films were determined using UV/vis spectroscopy (Figure 5.5). The 30 mol% fluorine-doped film had the highest visible transmittance. Increasing the fluorine concentration led to an increase in optical absoprtion. This could be due the incorporation of F^- ions, which can form colour centres in the film.[344] Slassi *et al.* found that fluorine-doping ZnO resulted in the formation of shallow donor states with fluorine 2p character.[345] They also observed that at high fluorine concentrations, the optical transmittance decreased due to an increase in absorption. Thus, it is possible that the decrease in optical transmittance may also be due to an increase in absorption due to shallow fluorine 2p states.

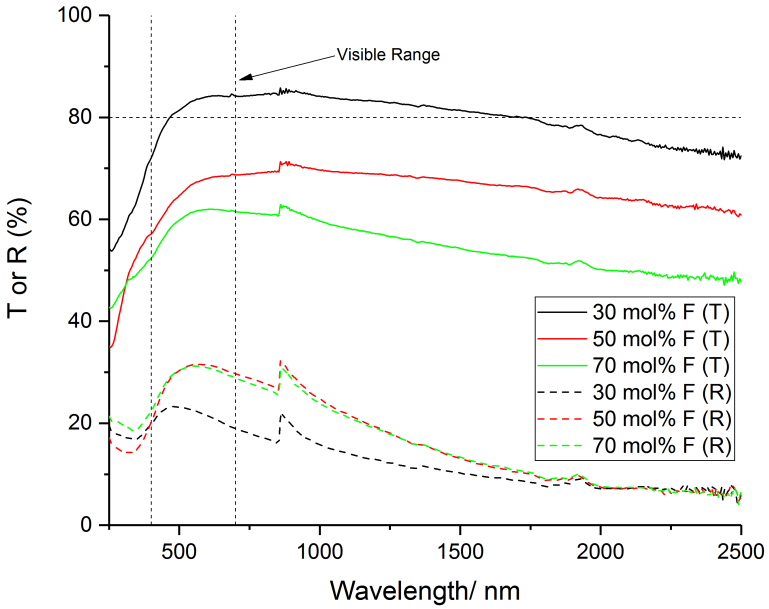

Figure 5.5: Transmission-reflectance spectra for the fluorine-doped $ZnSb_2O_6$ films deposited *via* spin coating, after annealing.

5.4 CONCLUSIONS

It was found that dual source AACVD was unsuccessful at depositing $ZnSb_2O_6$ thin films. The XRD patterns of the annealed films only displayed peaks for the quartz substrate, and for secondary antimony oxide phases. The films were all non-conductive.

A $ZnSb_2O_6$ ink was made by dispersing $ZnSb_2O_6$ nanoparticles in an ink vehicle supplied by Sun Chemical. U10197 was found to be a superior ink vehicle, and resulted in higher quality films. The addition of polystyrene in solution in a 6:1 ratio with the precursors led to a slight improvement in the crystal quality of the films. In an attempt to improve the conductivity, the films were fluorine-doped. It was found that high concentrations of F^- in solution may have led to the reduction of Sb^{5+}, leading to the formation of a secondary Sb_2O_4 phase. Increasing the fluorine concentration also led to a decrease

in the quality of the films, and a decrease in visible transmittance. Again, all of the films were non-conductive.

Further work is needed to improve the quality of the films, by increasing the film thickness, or by improving the dispersion of the nanoparticles in the ink. Additionally, annealing for different lengths of times, or at different temperatures could lead to improved film quality. Once this is achieved, a full dopant study can be performed to find the optimum dopant concentration for superior optoelectronic properties.

6

INVESTIGATING THE SCALE UP OF AACVD

This chapter focuses on steps towards the scale-up of AACVD — from a laboratory scale technique to a large scale technique which can be used for commercial depositions. The effects of transporting the aerosol prior to film deposition are investigated. The size of the droplet size distribution is also determined. The droplet size data was recorded in collaboration with Dr. Michael Powell. The droplet size data analysis was done by myself. Following this, the effect of precursor concentration on the film growth rates was determined at the laboratory scale, and at a larger scale. The film depositions and data analysis in this section were done in collaboration with Dr. Michael Powell. For this reason, the discussions in Section 6.4 will be kept relatively brief. A more in-depth discussion of Section 6.4.2 can be found in the paper by Powell *et al.*[112]

6.1 INTRODUCTION

AACVD has many advantages over conventional APCVD. These are discussed in detail in Section 1.4. In brief, the main advantages of AACVD are as follows:

1. More precursors are available for CVD-type depositions, as the requirement is solubility, rather than volatility.
2. Morphological control over the resultant film is easily achievable by varying the deposition conditions.

3. A simplified reactor design allows films to be deposited with ease, and with relatively low cost.

Despite its numerous benefits, AACVD is not currently used for any commercial depositions. This is because the scale-up of AACVD has not yet been properly investigated. Certain obstacles must be overcome, such as the long-distance transportation of the aerosol, increasing film growth rates, and engineering solvent extraction and recycling methods. This chapter will focus on the first two problems.

6.2 AEROSOL TRANSPORT STUDY

In an industrial setting, depositions on glass substrates are performed as the glass ribbon emerges, still hot, from the float line. For safety reasons, the precursor solution would need to be kept far from this area, to prevent the accidental ignition of the solvent. Hence, it is likely that the aerosol would be generated remotely, and then transported to the float line, to deposit as a film on the hot glass. The aerosol may need to be transported tens of metres from where it is generated, to where it is deposited. To investigate the feasibility of this, an aerosol transport study was performed. The 10 mol% AZO film had the best optoelectronic properties of any of the films deposited *via* AACVD described in this thesis. For this reason, it was selected for this study

6.2.1 *Experimental*

The conditions were maintained as described in Section 3.2.1. MeOH was used as the solvent, rather than a solvent mixture. This was done to avoid unwanted solvent effects, and to ensure that the mist is uniform, so that it would pass through the tubing at a constant rate.

The only difference in the deposition parameters was that the length of tubing between the bubbler and the baffle was increased, represented by the length *d* in Figure 2.1. The lengths of tubing used were 0.5 m, 2 m, 8 m, and 50 m. The 2 m tubing was coiled once, with a coil diameter of 0.4 m. The 8 m and 50 m tubing were coiled multiple times, with a coil diameter of 0.4 m.

6.2.2 *Film Synthesis*

The films were generally of high quality. They adhered well to the glass substrates, passing the Scotch tape test, and they resisted being scratched with a steel scalpel.

The films deposited using 0.5 m and 2 m tubing had interference patterns, indicating there was a thickness gradient, with some regions comparable to the wavelength of light. The films deposited using 8 m and 50 m tubing did not display interference patterns, which may have indicated that the films were thinner. The film deposited using 50 m tubing was so thin that it was barely visible upon the glass substrate.

The highest quality regions of the films were the regions nearest to the baffle, so these regions were characterised.

6.2.3 *Crystal Structure*

The crystal structures of the films were analysed by XRD (Figure 6.1). The film deposited using 0.5 m tubing showed a typical XRD pattern for AZO, with a preferential orientation in the (002) direction. The relative intensities of the peaks were very similar to the 10 mol% AZO film deposited in Chapter 3, which were deposited using the typical 0.1 m tubing. However, the overall peak intensities were lower,

possibly indicating the film deposited using 0.5 m tubing was thinner, or of a lower crystal quality.

The film deposited using 2 m tubing actually showed an increase in peak intensity. This suggests that the film had a more crystalline structure, or that it formed a thicker, or denser film. This could be due to the longer tubing allowing more residence time for the precursors to mix and react within the droplets. Thus, it may indicate that pre-deposition reactions within the droplets were taking place, which promoted film growth.

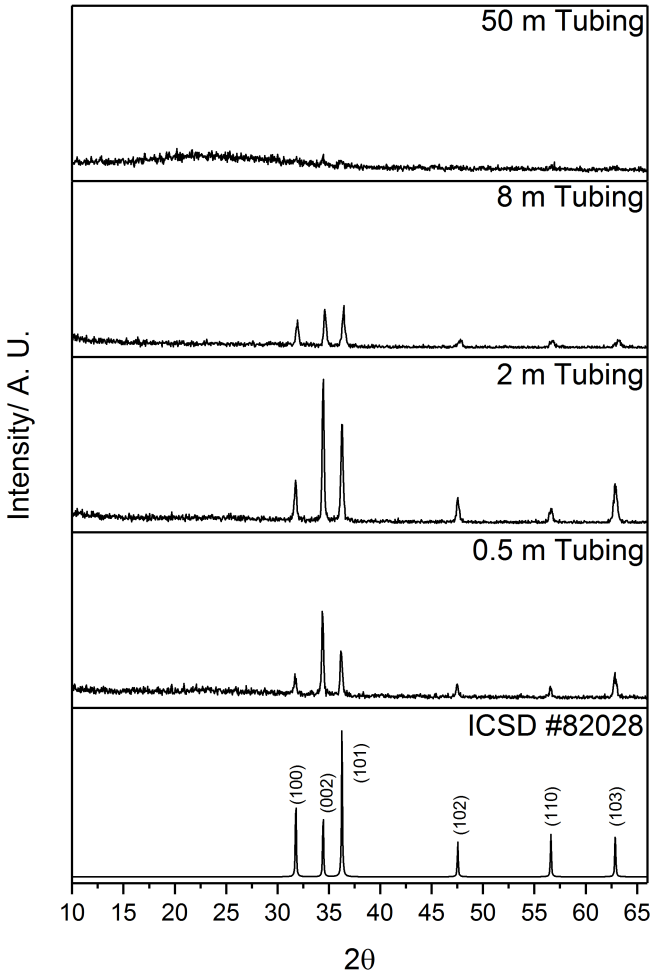

Figure 6.1: X-ray diffraction patterns of the 10 mol% AZO films deposited *via* AACVD, using increasing tubing lengths. A diffraction pattern of ZnO from ICSD #82028 is included for reference.

When 8 m tubing was used, the resultant film had much lower intensity peaks. This suggests that the film was thinner, or of poorer crystalline quality. This could be due to the aerosol condensing along the interiors of the tubing, leading to the precursors being lost prior to reaching the reactor.

The film deposited using 50 m tubing had very low intensity peaks. The majority of the XRD pattern consisted of a large amorphous region, indicating the film was so thin that the amorphous glass substrate beneath the film was being detected by the X-rays. Again, this suggests that a significant amount of precursor was being lost in the tubing prior to reaching the reactor.

Thus, there may be two competing processes affecting film growth. The first is the residence time of the precursors. Allowing more time for molecular mixing and pre-deposition reactions may promote film growth. However, the use of long lengths of tubing can also result in the aerosol condensing along the walls of the tubes. Consequently, insufficient precursor reaches the substrate for regular film growth.

6.2.4 *Surface Morphology*

Two regions of each film were analysed using SEM. The first region was the region closest to the baffle (Figure 6.2), as it consistently showed the highest quality films in terms of coverage and uniformity. The second region was 5 cm further along film (Figure 6.3). This was done to investigate how the surface morphology varied as the precursors travelled deeper within the reactor.

The region closest to the baffle is the same region that was analysed in previous chapters, so the images in Figure 6.2 can be compared to the SEM image of the 10 mol% AZO film from Chapter 3, which was deposited using the standard 0.1 m tubing. (Figure 3.12a).

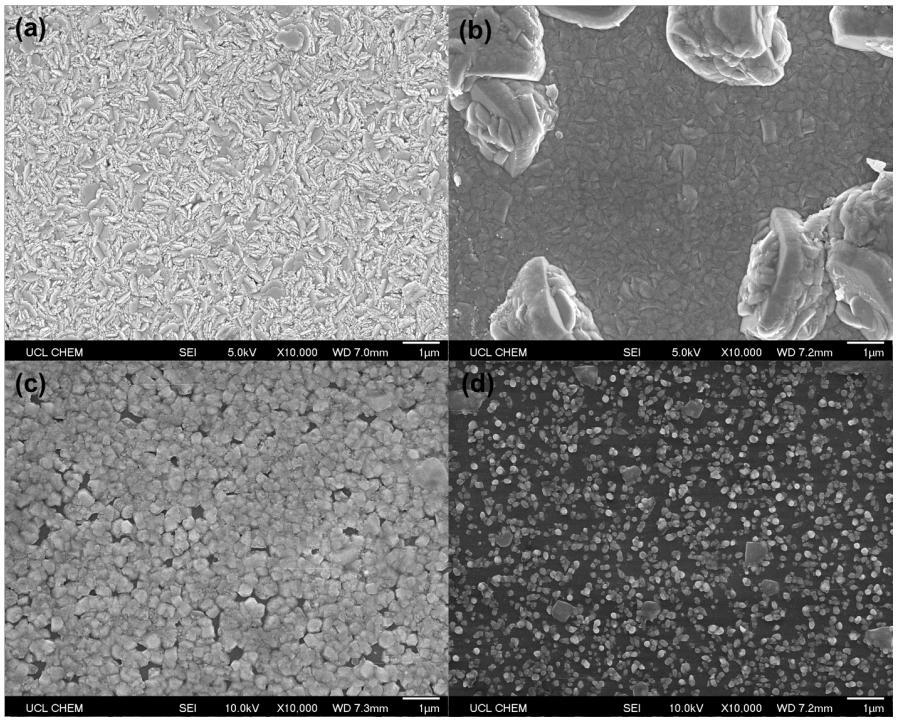

Figure 6.2: SEM images of the baffle-ends of the 10 mol% AZO films deposited *via* AACVD, using (a) 0.5 m, (b) 2 m, (c) 8 m, and (d) 50 m tubing.

When 0.5 m tubing was used (Figure 6.2a), the morphology was similar to the 10 mol% AZO film from Chapter 3. The grains in both films consisted of interlocking plates which appeared to be etched. This suggests that transporting the aerosol 0.5 m to the substrate did not hinder the film deposition.

Moving 5 cm further along the film, the morphology changed significantly (Figure 6.3a). Rather than the densely packed grain structure visible next to the baffle, a more porous morphology was observed. Additionally, the grain shape changed from plates to rounder, faceted grains. The hollow interiors of the grains were also visible, due to cracks in the upper surfaces. The change in morphology was due to the depletion in the precursors as the aerosol flowed further into the reactor.

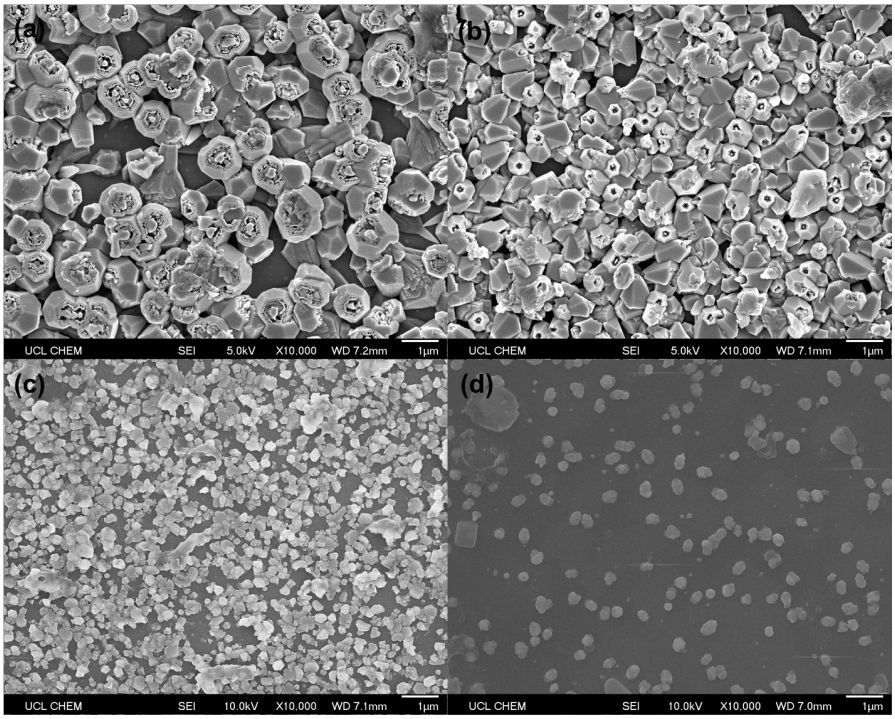

Figure 6.3: SEM images taken 5 cm further away from the baffle ends of the 10 mol% AZO films deposited *via* AACVD, using (a) 0.5 m, (b) 2 m, (c) 8 m, and (d) 50 m tubing.

When 2 m tubing was used (Figure 6.2b), the surface morphology became smoother in comparison to when 0.5 m was used. Additionally, large features were visible scattered across the film.

Again, there is a drastic change in morphology 5 cm further along the film (Figure 6.3b). This change is similar to what was observed for the film deposited using 0.5 m tubing. The shapes of the grains became rounder and more faceted. However, these faceted grains appeared slightly smaller, and slightly more elongated in comparison to the faceted grains from the film deposited using 0.5 m tubing.

The film deposited using 8 m tubing had smaller grains, with gaps in between (Figure 6.2c). Similarly, 5 cm further along the film, the grains were even smaller, with even larger gaps (Figure 6.3c). These morphologies indicate that insufficient precursors had reached the film surface in order to allow a continuous film to grow. This suggests

that some of the precursor was being lost along the tubing before it could reach the reactor.

The film deposited using 50 m tubing had only a small amount of film growth near the baffle (Figure 6.2d). Very small, disconnected grains can be seen scattered across the substrate. Moving 5 cm further along the film, the grains were even more scattered, with very large gaps between them (Figure 6.3d). Again, these morphologies suggest that a significant amount of precursor had been lost in the tubing prior to reaching the reactor.

For all the films, the region closest to the baffle had a denser morphology than the region 5 cm further along the film. This suggests that the deposition process was mass transport limited, whereby the chemical reactions at the surface were rapid. This means that the rate of deposition was determined by the rate at which fresh precursors can be supplied to the growing film.[98]

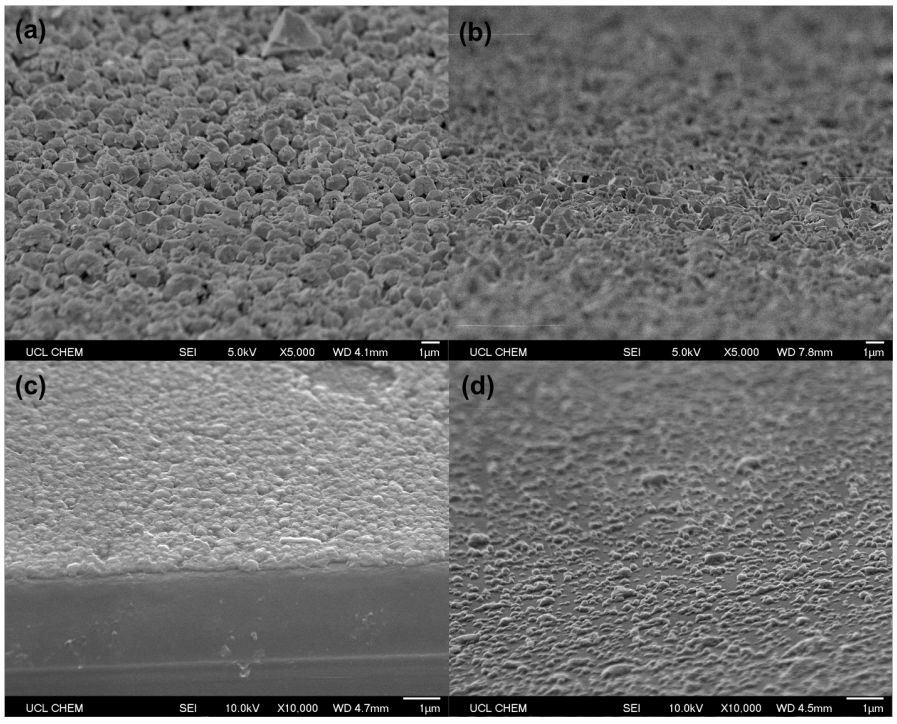

Figure 6.4: Angled SEM images of the 10 mol% AZO films deposited *via* AACVD, using (a) 0.5 m, (b) 2 m, (c) 8 m, and (d) 50 m tubing.

The deterioration in film growth and thickness with increasing tubing length can be seen in angled SEM images of the films (Figure 6.4). It can be seen that the film thickness decreases from 1 μm for the film deposited using 0.5 m tubing, to ~0.2 μm for the film deposited using 8 m tubing. Increasing the tubing length further to 50 m resulted in very little film growth, and poor substrate coverage.

6.2.5 *Droplet Size Analysis*

The average droplet diameter for different lengths of tubing was measured using Malvern Spraytec equipment, which utilises laser diffraction to determine the droplet size distribution in a spray or mist. This method relies on Mie theory, which states that, when light is scattered by a particle, the angle of scattering is inversely proportional to the particle size.[346–349]

Table 6.1: Average droplet sizes and distribution spans for aerosol mists generated within a glass bubbler, using an ultrasonic humidifier.

Tubing length /m	Average droplet diameter /μm	Average distribution span
0	8.0	2.2
2	4.8	1.2
4	5.3	1.0
8	5.4	0.8

The average droplet diameters and the droplet size distributions were obtained. The width of the distribution is given by the span, which is obtained using the following equation:

$$\text{span} = \frac{d_v(90) - d_v(10)}{d_v(50)} \tag{6.1}$$

where $d_v(n)$ is the droplet diameter below which, n% of the spray lies.[291] The results are presented in Table 6.1.

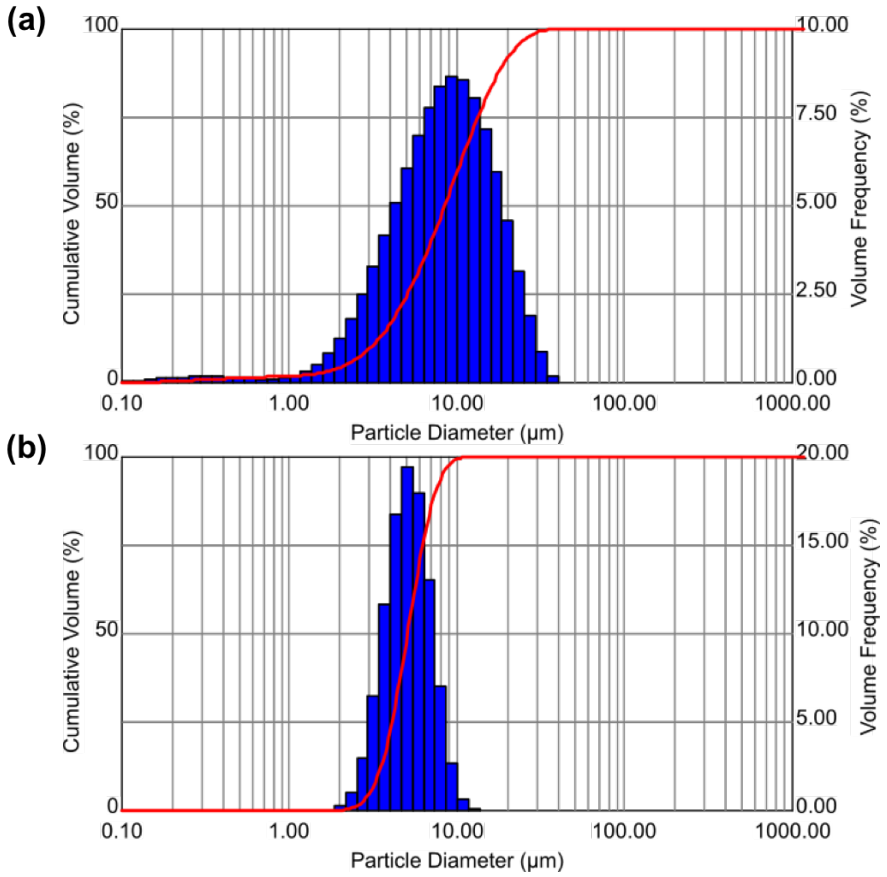

Figure 6.5: Size distribution of aerosol droplets, for (a) a mist as it emerges from the bubbler, and (b) a mist that has been transported 8 m through coiled tubing. Each bar in the histogram represents a size band of particles, with its height corresponding to the percentage of the aerosol which is within that band. The red line is the cumulative undersize, which represents the percentage of the aerosol which has a droplet diameter below a given size.

The average droplet diameter at the point where the mist leaves the bubbler (0 m tubing) is 8.0 µm. Transporting the aerosol led to a decrease in the average droplet diameter. Filho *et al.* developed a model that predicted that the average droplet size would decrease and that the droplet size distribution would become more narrow after transporting the aerosol through tubing.[350] Wang *et al.* stated that droplets in laminar or turbulent flow can undergo coagulation, whereby the coagulation rate is proportional to the third power of the

droplet diameter (d^3).[291] Van Borm *et al.* reported that larger droplets are removed from an aerosol due to gravitational settling, which leads to the average droplet diameter shifting to smaller values.[351]

Therefore, the observed reduction in droplet diameter upon transporting the aerosol mist was due to the agglomeration of droplets, which led to an increase in gravitational and centrifugal settling of the larger droplets. However, the distance that the aerosol was transported did not seem to have a significant effect on the average droplet diameter.

The droplet diameter distribution, measured by the span, decreased linearly with tubing length. This can be seen clearly in Figure 6.5. The reason for this narrowing of the distribution is most likely because the further the aerosol was transported, the more time there was for the smaller droplets in the mist to agglomerate, and for larger droplets to condense on the walls of the tubing.

6.3 QUANTIFYING THE AMOUNT OF AEROSOL LOST IN THE TUBING

It is apparent that a significant amount of aerosol was condensing along the interior walls of the tubing, prior to reaching the reactor. This had detrimental effects on film growth, as the mass flow of precursors was reduced.

6.3.1 *Experimental*

To estimate the amount of aerosol lost along the tubing, a typical precursor solution for 10 mol% AZO was made up, and an aerosol mist was generated in the usual way as described in Chapter 3. The aerosol was passed through different lengths of coiled tubing (2 m, 8 m, and 50 m) using N_2 carrier gas at a flow rate of 1 L min^{-1}.

Instead of attaching the far end of the tubing to the reactor, it was attached to a pre-weighed cold-trap, which contained glass wool, and was submerged in liquid N_2 to ensure that all of the aerosol that entered the cold trap would condense. The initial mass of the precursor solution was also weighed. The difference in the mass of the cold trap before and after the "deposition" was used to estimate the amount of aerosol lost along the tubing. Each "deposition" was repeated at least three times to ensure reproducibility of the results.

6.3.2 *Results and Discussion*

The change in mass of the cold trap was used to calculate the mass of the solution that remained in the tubing (Table 6.2). From this, the volume of the solution lost in the tubing was calculated, as well as the percentage loss.

Table 6.2: Approximate amounts of solution lost in the tubing, when passing the aerosol along different lengths of tubing. The initial mass of the 20 mL precursor solution was 16.4 g.

Tubing Length /m	Approximate amount lost in tubing /g	Approximate amount lost in tubing /mL	Approximate amount lost in tubing /%
2	8–9	10–11	~50
8	13–14	16–17	~80
50	15–16	19–20	~95

It can be seen that, by transporting the aerosol just 2 m prior to deposition, approximately 50% was lost before reaching the reactor. When the length of tubing was increased to 8 m, the majority of the aerosol was lost. Increasing the length further to 50 m resulted in almost all of the aerosol condensing before it reached the reactor. This explains why the quality of the film deposited using 50 m tubing was so poor, as shown by its XRD pattern (Figure 6.1) and its SEM

images (Figures 6.2d, 6.3d, and 6.4d). Only ~5% of the aerosol was able to navigate the tubing to deliver the precursors to the substrate.

Based on these results, it seems unfeasible to transport an aerosol tens of metres to the substrate, as is required for an industrial deposition process. It should be mentioned that the tubing for these experiments was arranged in a coil. This is an extreme arrangement, since in an industrial setting, although there were still be bends and turns, there will also be long straight sections. It would be easier for the aerosol to traverse a straight section, as it would not collide with the walls to the same extent. However, it is evident that a significant amount of aerosol will likely be lost in the tubing when transported long distances. The 2 m tubing only contained a single coil, and thus a relatively high percentage of the tubing was straight, compared to the 8 m and 50 m tubing. Despite this, approximately 50% of the aerosol was lost in 2 m tubing before reaching the reactor.

6.4 THE EFFECT OF PRECURSOR CONCENTRATION ON FILM GROWTH RATES

One drawback of AACVD is that the growth rates of the films are typically quite low. The films deposited *via* AACVD in Chapters 3 and 4 were grown in 30-40 minutes, and had thicknesses of ~1 μm. Thus, the growth rates achieved for these films were approximately 30 nm min^{-1}. Similarly, Manzi *et al.* deposited AZO films *via* AACVD and were able to grow 470–500 nm thick films in 30–35 minutes, yielding a growth rate of ~16 nm min^{-1}.[187] Nolan *et al.* deposited IZO films *via* AACVD, which were approximately 200 nm thick, in a deposition time of 20 minutes.[188] This gave a deposition rate of ~10 nm min^{-1}. Chen *et al.* deposited ZnO thin films *via* AACVD.[352] Their films were approximately 1 μm, and were grown in 60–100 mins, which gave a

growth rate of ~13 nm min^{-1}. Basharat *et al.* deposited Ga_2O_3 thin films *via* AACVD.[213] Their films were 300–400 nm thick, and were grown in approximately 120 mins. This yielded a growth rate of ~3 nm min^{-1}.

These growth rates of *ca.* 10s of nm min^{-1} are too low for most industrial applications, which usually require growth rates of 10s or even 100s nm s^{-1}.[112] This section describes a route towards scaling AACVD for industrial purposes, by improving the growth rates of FTO films. This was done by investigating the concentrations of the precursors in solution. FTO was used as the material for this study, as it is a well-characterised, and effective TCO. It is known to grow with ease and consistency.

6.4.1 *Experimental*

6.4.1.1 *Laboratory Scale Depositions*

A typical precursor solution was made up by dissolving monobutyltin trichloride [$^{n}BuSnCl_3$] in MeOH. The concentration of $^{n}BuSnCl_3$ was varied between 0.2 and 2 mol dm^{-3}. Ammonium fluoride [NH_4F] was used as the fluorine source, at a concentration of either 15 or 30 mol% fluorine relative to tin. The sample descriptions are summarised in Table 6.3.

An aerosol mist of the precursor solution was generated using a TSI Model 3076 Constant Output Atomiser, which typically generates 0.3 μm droplets.[38,45] This was used instead of the humidifier from previous chapters, because it generally produces a more continuous supply of aerosol, which is important when examining the growth rates.

Compressed air was used as the carrier gas, at a constant pressure of 2 bar. The deposition temperature was maintained at 550 °C, as Noor *et al.* found that this temperature gave optimum TCO properties

Table 6.3: Descriptions of FTO samples deposited *via* AACVD, on the laboratory scale.

Sample	Concentration of $^{n}BuSnCl_3$ /mol dm^{-3}	Concentration of F relative to Sn /mol%
FTO1	0.2	15
FTO2	0.2	30
FTO3	0.5	15
FTO4	0.5	30
FTO5	1.0	15
FTO6	1.0	30
FTO7	2.0	15
FTO8	2.0	30

for FTO films deposited *via* AACVD.[45] Deposition times were fixed at 5 minutes. As in previous chapters, Pilkington barrier glass cut to an area of 10 x 4.5 cm^2 was used as the substrate. After each deposition, the substrate was left to cool to below 100 °C, under a continuous flow of carrier gas. At this point, the film was removed for analysis.

6.4.1.2 *Larger Scale Depositions*

A typical precursor solution was made up by dissolving monobutyltin trichloride [$^{n}BuSnCl_3$] in MeOH. The concentration of $^{n}BuSnCl_3$ was varied between 0.4 and 0.74 mol dm^{-3}. Ammonium fluoride [NH_4F] was used as the fluorine source, at a concentration of 15 mol% relative to Sn. The sample descriptions are summarised in Table 6.4.

An aerosol mist of the precursor solution was generated using a Sonozap Sonaer high temperature atomiser nozzle, which uses an ultrasonic piezoelectric device that operates at 30 kHz, and is capable of atomising up to 100 mL min^{-1}. A syringe pump was used to draw the precuror solution through the nozzle, and the aerosol was generated at the tip. The aerosol was directed into the flow of the carrier gas. N_2 was used as the carrier gas, at a flow rate of 12 L min^{-1}. Tubing was attached to the exhaust of the reactor, and a pump was used to vent

Table 6.4: Descriptions of FTO samples deposited *via* AACVD, on a larger scale.

Sample	Concentration of $^{n}BuSnCl_3$ /mol dm^{-3}	Deposition time /s
FTOA	0.40	210
FTOB	0.47	210
FTOC	0.54	210
FTOD	0.60	210
FTOE	0.60	60
FTOF	0.60	30
FTOG	0.67	30
FTOH	0.74	20

the exhaust into the fumehood. This helped to reduce turbulant flow. The setup is shown in Figure 6.9a. The deposition temperature was maintained at 550 °C.[45] Deposition times were varied, as described in Table 6.4. Pilkington barrier glass cut to an area of 20 x 9 cm^2 was used as the substrate.

6.4.2 *Laboratory Scale Depositions*

The properties of the FTO films are summarised in Table 6.5. The films were all adhesive, passing the Scotch tape test, and resisted being scratched with a steel scalpel.

All of the as-deposited films consisted exclusively of tetragonal cassiterite SnO_2 (Figure 6.6). No secondary phases were observed by XRD. Increasing the precursor concentration in solution resulted in an increase in preferrential growth of the (200) plane. It has been observed previously that fluorine incorporation promotes growth in the (200) plane.[45,353] This suggests that increasing the tin concentration in solution also led to an increase in fluorine incorporation.

Table 6.5: Structural, optical, and electrical properties of FTO films deposited *via* AACVD on the laboratory scale. Full sample descriptions can be found in Table 6.3.

Film	Film thickness /μm	$T_{\lambda 400\text{-}700}$ /%	Resistivity $\times 10^{-3}$ /Ω·cm	Carrier concentration $\times 10^{20}$ /cm^{-3}	Mobility /cm^2/V·s
FTO1	0.15	83	26.1	0.7	3.5
FTO2	0.15	82	4.5	1.5	9.2
FTO3	0.40	80	0.9	4.6	14.9
FTO4	0.40	80	1.3	2.9	16.6
FTO5	0.50	78	0.3	11.8	15.7
FTO6	0.50	79	0.3	12.3	19.4
FTO7	0.50	79	1.0	3.1	21.1
FTO8	0.50	80	1.0	3.2	20.5

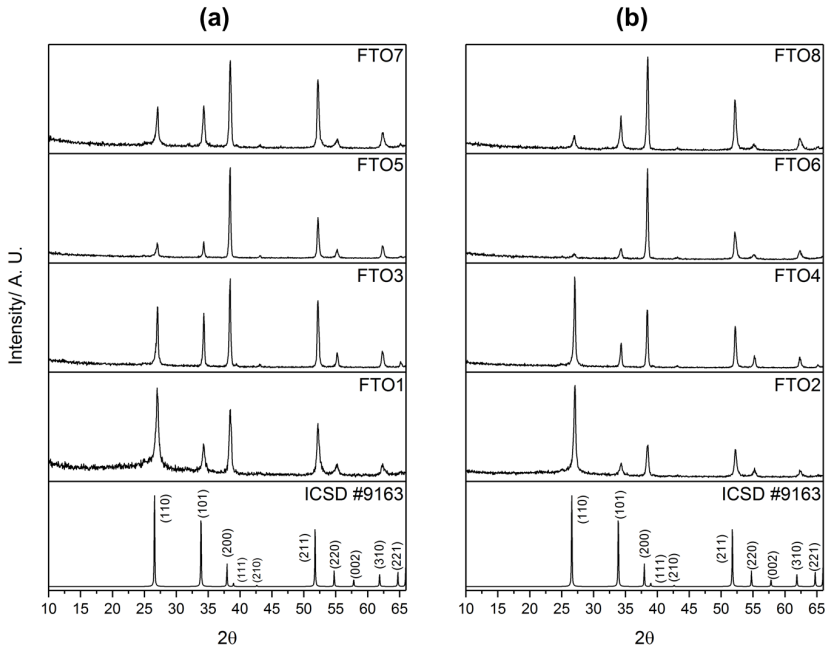

Figure 6.6: X-ray diffraction patterns of the FTO films deposited *via* AACVD at the laboratory scale, using different concentrations of ^{n}BuSnCl$_3$ in solution, with (a) 15 mol%, and (b) 30 mol% fluorine, relative to tin. Full sample descriptions can be found in Table 6.3.

Apart from the change in preferred orientation, the other feature observed when the precursor concentration was increased was the increase in crystal quality. This is indicated by the more intense

peaks in the XRD patterns for the films deposited with high dopant concentrations. However, this could also be related to an increase in the film thicknesses. The film thicknesses were obtained by ellipsometry, and are shown in Table 6.5. It is apparent that the film thicknesses increased with $^{n}BuSnCl_3$ concentration in solution, up to a concentration of 1 mol dm^{-3}. When the concentration was increased to 2 mol dm^{-3}, the solution became too viscous to be atomised as effectively, and the thickness did not increase further.

Since the deposition times were fixed at 5 minutes, a film thickness of 500 nm corresponds to a growth rate of 100 nm min^{-1}. This is a significant improvement over typical AACVD growth rates, which are *ca.* 10 nm min^{-1}.

XPS analysis of the films confirmed the presence of Sn^{4+}, with a binding energy of 487.0 eV ($\pm$ 0.2 eV) at the surfaces and within the bulks of the films (Figure 6.7). This corresponds to literature values for SnO_2.[354,355]

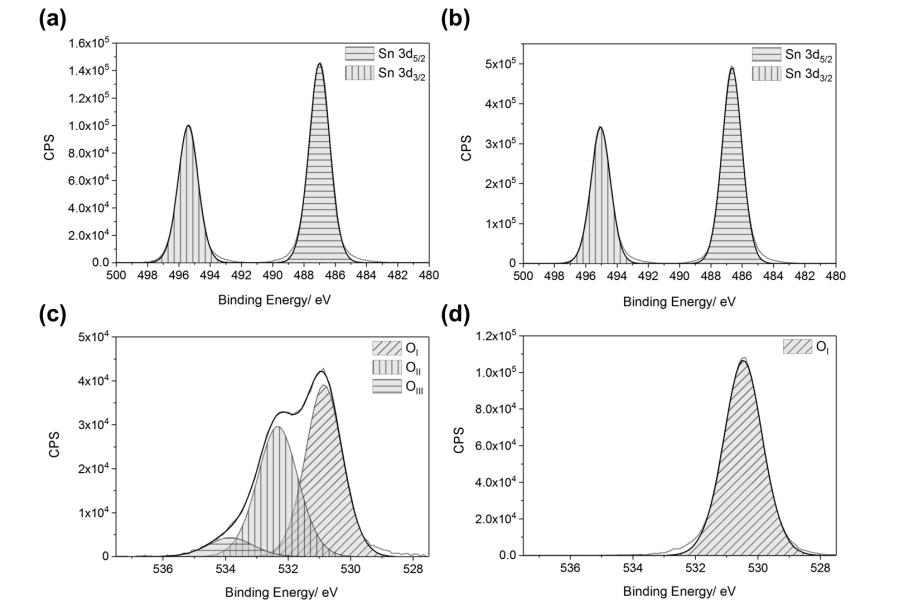

Figure 6.7: Typical XPS spectra for the FTO films deposited *via* AACVD at the laboratory scale, showing the (a) tin 3d peaks at the film surface, (b) tin 3d peaks in the bulk of the film, (c) oxygen 2p peaks at the film surface, and (d) oxygen 2p peaks in the bulk of the film.

The presence of fluorine was also confirmed by the presence of the fluorine 1s peak. However, the concentration of fluorine incorporated into the films was low for all the films (~0.5–1 atom%). Etching the film showed that the fluorine was not surface segregated, and was evenly distributed throughout the bulks of the films.

The surface oxygen 2p peaks revealed multiple oxygen environments, O_I, O_{II}, and O_{III}, corresponding to O–Sn, O–C (from surface-bound carbon), and O–H (from surface-bound water), respectively. In the bulks of the films, only the O–Sn environment at 530.6 eV (± 0.2 eV) was observed.[356]

The surface morphologies of the films were analysed using SEM (Figure 6.8). The grains consisted of pyramidal-like structures. The films deposited using 0.2 mol dm^{-3} $^{n}BuSnCl_3$ showed significant spaces between grains, which can be attributed to the lower tin concentration in solution. The films deposited using 30 mol% fluorine had smaller grain sizes than the 15 mol% analogues. This suggests that fluorine had an influence over the growth mechanism. Changing the tin concentration in solution did not have a significant effect over the surface morphologies.

All of the films displayed a high visible transmittance (Table 6.5). The fluorine concentration did not appear to have a significant effect over the optical properties, most likely due to the fact that the fluorine concentration in the films was consistently low, as determined by XPS. Generally, the thicker films had a slightly lower visible transmittance, due to the increased path length for light, which led to an increase in absorption. Interestingly, the films deposited using 1 mol dm^{-3} $^{n}BuSnCl_3$ showed optical properties that were reminiscent of low-emissivity coatings. These coatings are optically transparent, with a high reflectance in the NIR region, which grants them thermally insulating properties.[247]

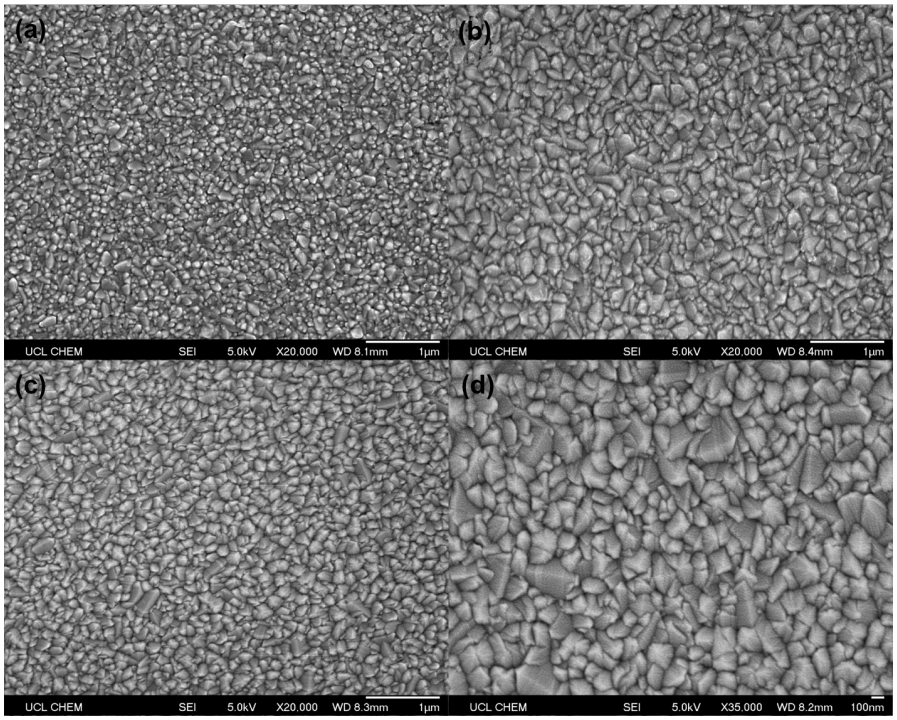

Figure 6.8: SEM images of (a) FTO2, (b) FTO6, (c) FTO7, and FTO8, all deposited *via* AACVD. Full sample descriptions can be found in Table 6.3.

The electrical properties of the films showed a significant improvement when increasing the $^{n}BuSnCl_3$ concentration from 0.2 to 1 mol dm^{-3}, where a minimum resistivity of 3×10^{-4} Ω·cm was achieved (Table 6.5). It was also found that, for low $^{n}BuSnCl_3$ concentrations, using 30 mol% fluorine in solution resulted in vastly superior electrical properties. However, when higher concentrations of $^{n}BuSnCl_3$ were used, the fluorine concentration did not have a significant effect over the electrical properties.

The electrical properties of these films were superior to previous attempts at depositing FTO by various techniques, including magnetron sputtering,[37] APCVD,[43] and spray pyrolysis.[353] Additionally, they are comparable to industrial standards (Table 3.4). Noor *et al.* also deposited FTO films *via* AACVD, at 550 °C, using the same precursors, solvent, and carrier gas as those used for the films in this section.[45] They achieved a resistivity value of 4×10^{-4} Ω·cm, which agrees with these findings. However, their depositions were

performed in 30 minutes, which indicates that the same electronic properties could be achieved in a much shorter time, simply by increasing the precursor concentration in solution.

6.4.3 *Larger Scale Depositions*

The properties of the FTO films deposited at the larger scale are summarised in Table 6.6. The films showed excellent coverage of the larger substrates, and displayed typical interference patterns, which is due to the suction exhaust drawing the aerosol through the reactor (Figure 6.9b).

Table 6.6: Structural, optical, and electrical properties of FTO films deposited *via* AACVD on a larger scale. Full sample descriptions can be found in Table 6.4.

Film	Film thickness /μm	$T_{\lambda 400\text{-}700}$ /%	Resistivity $\times 10^{-3}$ /Ω·cm	Carrier concentration $\times 10^{20}$ /cm^{-3}	Mobility /cm^2/V·s
FTOA	0.30	86	N/A	N/A	N/A
FTOB	0.73	82	5.8	0.7	16.1
FTOC	0.65	81	2.8	1.0	23.2
FTOD	0.17	85	9.4	0.4	15.2
FTOE	0.45	84	8.5	0.6	12.9
FTOF	0.30	83	3.6	1.4	12.6
FTOG	0.80	85	2.3	1.1	23.9
FTOH	0.67	83	2.7	0.9	24.4

The regions of the films nearest to the baffle were the thickest. The samples deposited using higher concentrations of $^{n}BuSnCl_3$ (FTOC, FTOD, and FTOE) were so thick near the baffle that they began to delaminate a few minutes after being removed from the reactor. Additionally, thickness-related optical absorption was occurring in these thick regions, leading to darkening of the films. For this reason, the central region of the films were characterised, where the

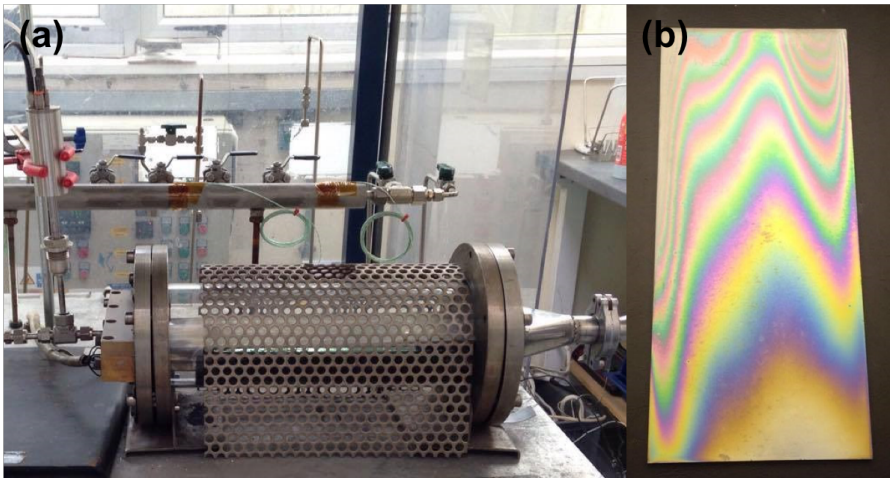

Figure 6.9: (a) An image of the laboratory AACVD setup for large scale depositions. The Sonozap Sonaer high temperature atomiser nozzle can be seen clamped on the left. The generated aerosol was directed into the stream of the carrier gas, which flowed through the piping coming from the left of the image, directly to the baffle. The exit port of the reactor on the right was attached to tubing which pumped the exhaust away. (b) An image of a typical film, viewed at an angle to display the interference fringes. The substrate dimensions are 20 x 9 cm^2. The baffle-end of the substrate is at the top of the image.

adhesion was superior. In this region, all of the films passed the Scotch tape test, and resisted being scratched with a steel scalpel.

The thicknesses of the films were determined by ellipsometry, and are given in Table 6.6. A maximum growth rate of 2 $\mu m\ min^{-1}$ was achieved for sample FTOH, which was deposited in just 20 s. This is sufficient for industrial applications, and hence confirms AACVD as a scalable technique.

All of the films consisted exclusively of cassiterite SnO_2 (Figure 6.10). In general, the films deposited using lower concentrations of $^nBuSnCl_3$ in solution displayed relatively poor crystal quality, even with longer deposition times, suggesting that insufficient precursor was being supplied to the growing film. Conversely, using high concentrations of $^nBuSnCl_3$ resulted in superior crystal growth, even with short deposition times. This indicates that the early stages of film growth are important for the overall crystallinity. Sufficient

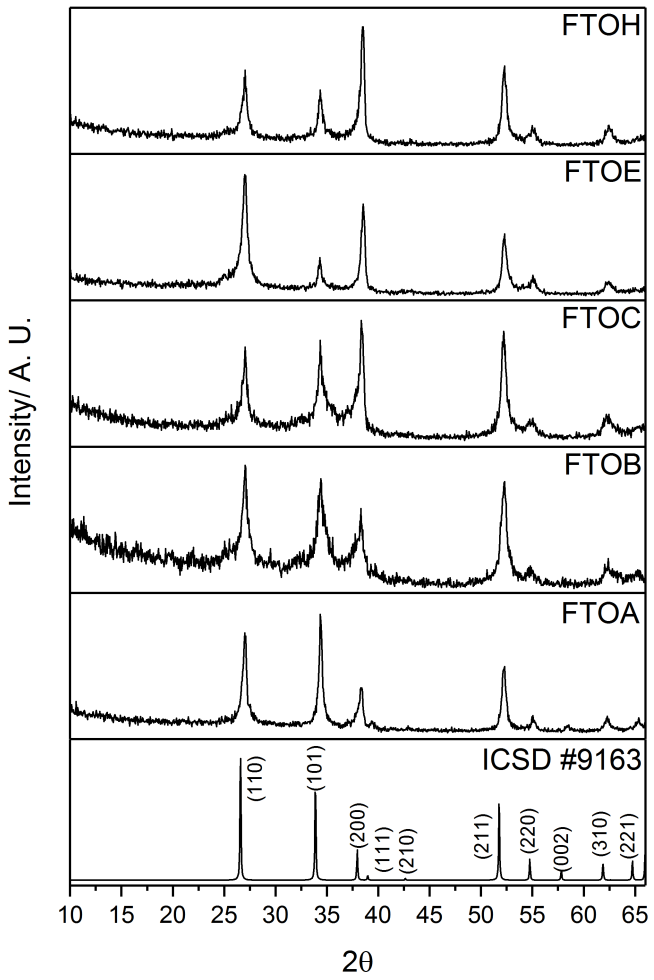

Figure 6.10: Typical X-ray diffraction patterns of the FTO films deposited *via* AACVD at a larger scale. Full sample descriptions can be found in Table 6.4.

precursor must be available as the film begins to deposit, to act as a seed for the polycrystalline growth. If the film is not initially supplied with enough precursor, the overall crystal quality will be worse, even if the crystallites have longer to grow.

This hypothesis is confirmed when examining the surface morphologies of the FTOC and FTOH. These films had very similar thicknesses, as determined by ellipsometry, so comparing their morphologies should give an indication of their growth mechanism. When the film was deposited using a low concentration of $^{n}BuSnCl_3$

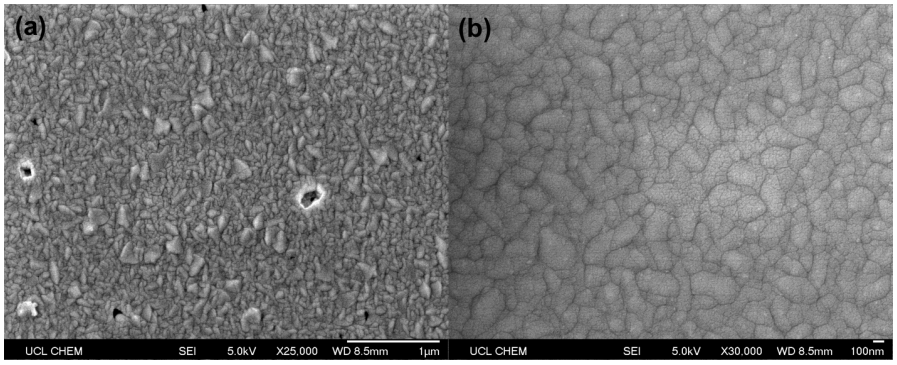

Figure 6.11: SEM images of (a) FTOC, and (b) FTOH, both deposited *via* AACVD, showing typical surface morphologies. Full sample descriptions can be found in Table 6.4.

as in sample FTOC (Figure 6.11a), the crystallites were small, and large pinhole defects were present between the grains. When comparing this morphology to that of FTOH (Figure 6.11b), the effect of precursor concentration can clearly be seen. The grains of sample FTOH were significantly larger and more well-connected. This is significant, considering the deposition time for FTOH was approximately 10% of what was allowed for FTOC. This denser morphology indicates that having a high concentration of precursor available in the early stages of film growth resulted in a far superior grain structure.

All of the as-deposited films displayed high transparency in the visible part of the spectrum, meeting the 80% requirement for commercial applications (Figure 6.12). Similarly, the films displayed excellent electronic properties, achieving minimum resistivity values of 2.3 $\times 10^{-3}$ Ω·cm and 2.7 $\times 10^{-3}$ Ω·cm for samples FTOG and FTOH, which were deposited in just 30 s and 20 s, respectively. Therefore, materials which are appropriate for TCO applications have been deposited at high growth rates, making the deposition technique a feasible route for industrial processes.

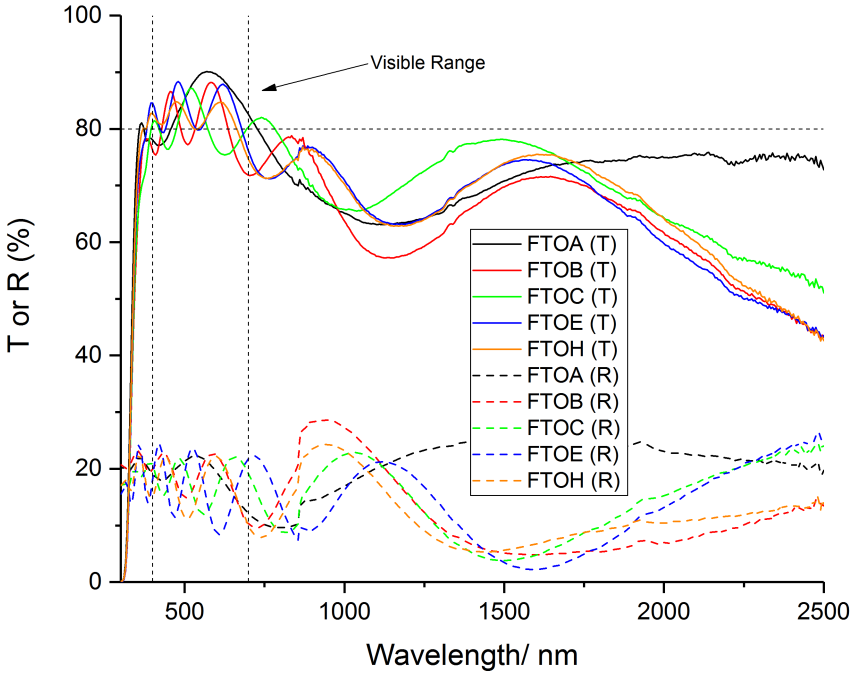

Figure 6.12: Typical transmission-reflectance spectra of the FTO films deposited *via* AACVD at the larger scale. Full sample descriptions can be found in Table 6.4.

6.5 CONCLUSIONS

The transport of the aerosol mist prior to deposition was investigated. It was found that transporting the aerosol 2 m prior to deposition improved the properties of the resultant AZO film, since there was a longer residence time for pre-deposition reactions to occur. However, transporting the aerosol 8 m and led to a significant deterioration in film quality. This was deemed to be due to the large amount of aerosol condensing on the walls of the tubing — approximately 95% for 50 m tubing. In addition, the droplet size distribution was measured, after transporting the aerosol. It was found that transporting the aerosol a short distance (2 m) led to a reduction in droplet diameter. Transporting the aerosol any distance further than this did not result in a significant change in diameter. Moreover,

the droplet size distribution decreased linearly with tubing length, as there was more time for small droplets to agglomerate, and large droplets to settle in the tubing.

The growth rates of FTO films deposited *via* AACVD have been improved from *ca.* 10 nm min^{-1} to 2 μm min^{-1}, by increasing the precursor concentration in solution, and by modifying the deposition set up. The resultant films were shown to maintain their excellent optoelectronic properties, which were comparable to current industrial standards. This work has shown the versatility of the AACVD technique, and how it has the potential to deposit films at the required growth rates for commercial applications.

Part III

CONCLUSIONS, APPENDIX AND BIBLIOGRAPHY

7

CONCLUSIONS

This thesis has focused on the synthesis of zinc-based thin films for TCO applications. Chapter 3 described the synthesis of aluminium-, gallium-, and indium-doped zinc oxide thin films *via* AACVD. These dopants were also used in tandem to prepare co-doped zinc oxide. Following this, a solvent study was performed using the most conductive film, to examine the effect of the solvent on the resultant films.

In Chapter 4, silicon-doped zinc oxide films were deposited *via* AACVD, in the same conditions as the films from Chapter 3. In addition, fluorine/silicon co-doped films were synthesised to see how the addition of fluorine would affect the films.

Chapter 5 detailed attempts at synthesising conductive $ZnSb_2O_6$ thin films *via* dual source AACVD and *via* spin coating. It was found that $ZnSb_2O_6$ could not be made *via* dual source AACVD. However, spin coating an easily synthesised $ZnSb_2O_6$ ink was a viable technique to deposit $ZnSb_2O_6$ thin films.

Finally, Chapter 6 described the investigation into the scale up of AACVD. An aerosol transport study was performed to ascertain the feasibility of transporting the aerosol long distances prior to deposition, as would be the case in an industrial deposition process. Following this, scaled-up depositions of fluorine-doped tin oxide were performed at high growth rates, by increasing the precursor concentration in solution.

A summary of the key findings from the work described in this thesis, as well as the necessary future work is presented in Table 7.1.

Table 7.1: Summary of key results and future work.

Chapter	Results	Future work
3	• AZO, GZO, IZO, AGZO, IGZO, and AIZO thin films synthesised *via* AACVD. • Transmittance >80% for most films. • Lowest resistivity for 10 mol% AZO (5×10^{-3} /Ω·cm) • Incorporation of In^{3+} led to disorder and deterioration in properties. • Solvent mixture of MeOH and ethyl acetate resulted in 60% reduction in resistivity.	• Use alternative precursors for depositions. • Optimise dopant concentrations for co-doped films. • Deposit films using other dual solvent mixtures. • Optimise solvent ratios for solvent mixtures.
4	• SZO and FSZO thin films synthesised *via* AACVD. • Higher resistivity compared to AZO, but also higher mobility. • Co-doping with fluorine resulted in higher incorporation of silicon.	• Deposit SZO films using alternative precursors. • Deposit SZO using solvent mixture. • Optimise dopant concentrations for FSZO.
5	• $ZnSb_2O_6$ films could not be deposited *via* AACVD. • $ZnSb_2O_6$ films were deposited *via* spin coating. • All films were non-conductive, even when doped with fluorine.	• Use alternative precursors for AACVD depositions. • Optimise AACVD conditions. • Optimise spin coating depositions. • Optimise doping element and concentrations.
6	• Aerosol transported up to 50 m prior to deposition. • Transporting aerosol just 2 m led to approximately 50% losses of solution. • FTO films deposited at growth rates of 2 μm min^{-1}.	• Transport aerosol using different types of tubing. • Perform large-scale depositions of ZnO films.

Overall, the work described in this thesis has shown the versatility of AACVD as a technique to prepare effective TCO thin films. It has been used to successfully deposit many zinc-based TCO materials, from various air-stable precursors, and in a variety of conditions. Although the optoelectronic properties do not meet those of industrial standards deposited by other techniques such as magnetron sputtering, the ease of deposition makes these results promising. The scalability of the AACVD technique has also been demonstrated, by improving the film growth rates to levels which are comparable to current industrial deposition techniques. Future work related to this research project could build upon these findings, leading to the discovery of other sustainable TCO materials from inexpensive zinc precursors. Additionally, the scale up of AACVD can be accomplished by engineering more effective aerosol transport systems.

A

APPENDIX

A.1 REFINEMENT OF XRD DATA

The diffraction pattern of a material is determined by its crystal structure, and contains a vast amount of important information. The peak position is due to the interplanar distance, which is related to the type of crystal structure. The peak intensity is due to atomic positions within the unit cell, as well as factors such as preferred orientation. The peak width and shape can be related to the instrument, sample orientation and to crystalline defects.

Thus, the XRD data can be refined to extract information such as unit cell parameters, atom positions, etc. The two main ways to do this are Rietveld refinement and Le Bail refinement. Both of these methods rely on a least-squares process, whereby each time a calculated model of the data is refined, the model tends towards the minimum value of the sum of the square of the differences between the experimental data and the model, thus gradually improving the model until it matches the observed data. Each iteration of the model is refined by changing the values of different parameters. The parameters which are refined are slightly different, depending on which method is being employed.

A.1.1 *Reitveld Refinement*

In Reitveld refinement, two types of parameters can be refined: instrumental and structural. The instrumental parameters (which are dependant on the diffractometer and sample orientation) are the instrumental zero error ($2\theta_{zero}$), the unit cell metric tensor (*A*, *B*, *C*, *D*, *E*, *F*), the peak width parameters (*U*, *V*, *W*), the peak shape parameters (*P*, η), and the preferred orientation parameter (*G*). The structural parameters (which are dependant on the crystal structure of the sample) are the overall scale factor (*c*), the fractional atomic coordinates (x_n, y_n, z_n), the isotropic temperature factor (B_n) or the anisotropic temperature factor (β_{ij}), and the site occupation factor (N_n).

The peak intensities of the model are calculated from these parameters, and are refined using the following equation:

$$\Delta = \sum_{n=1}^{N} \{I_n(obs) - I_n(calc)\} \tag{A.1}$$

where Δ is the least squares value, and $I_n(obs)$ and $I_n(calc)$ are the intensities of the nth peaks from the experimental data and the calculated model, respectively.

A.1.2 *Le Bail Refinement*

Le Bail refinement typically refines the same parameters as Rietveld refinement, except for the peak intensities. The intensities are initally set to an arbitrary value. Each time a refinement iteration is performed, the calculated intensity values are set as the observed intensity values. This process is repeated, thus slowly converging

towards the experimentally observed values. Since the intensities are not refined using least squares, this method requires less computing power. In general, Le Bail refinement estimates the best possible fit when there are irregular profiles. Since peak intensities are not refined, preferred orientation can be modelled with relative ease.

BIBLIOGRAPHY

(1) G. F. Nordberg, B. A. Fowler, M. Nordberg and L. T. Friberg, *Handbook on the Toxicology of Metals*, Academic Press, 3rd edn., 2007, p. 975 (cited on page 3).

(2) S. C. Dixon, D. O. Scanlon, C. J. Carmalt and I. P. Parkin, *J. Mater. Chem. C*, 2016, **419**, 6946–6961 (cited on pages 4, 8).

(3) K. Hayashi, S. Matsuishi, T. Kamiya, M. Hirano and H. Hosono, *Nature*, 2002, **419**, 462–465 (cited on page 4).

(4) S. M. Sze, *Semiconductor Devices: Physics and Technology*, 2006, p. 568 (cited on page 5).

(5) R. Hoffmann, *Solids and surfaces: A chemist's view of bonding in extended structures*, VCH Publishers, 1st edn., 1988, p. 139 (cited on pages 5, 82, 137).

(6) P. T. Yu and M. Cardona, *Fundamentals of Semiconductors - Physics and Materials Properties*, Springer-Verlag Berlin Heidelberg, 2010, pp. 1–669 (cited on pages 5, 9, 54).

(7) C. E. Housecroft and A. G. Sharpe, *Inorganic Chemistry*, Prentice Hall, 2nd edn., 2005, p. 992 (cited on pages 8, 133).

(8) A. R. West, *Solid State Chemistry and its Applications*, Wiley-Blackwell, 2nd edn., 2003, p. 453 (cited on page 9).

(9) G. R. Rossman, *Gems & Gemology*, 1981, **17**, 60–71 (cited on page 9).

(10) K. Nassau, *Scientific American*, 1980, **243**, 124–154 (cited on pages 9, 61).

(11) E. Burstein, *Physical Review*, 1954, **93**, 632–633 (cited on page 9).

(12) T. S. Moss, *Proceedings of the Physical Society, Section B*, 1954, **67**, 775–782 (cited on page 9).

(13) S. Jin, Y. Yang, J. E. Medvedeva, J. R. Ireland, A. W. Metz, J. Ni, C. R. Kannewurf, A. J. Freeman and T. J. Marks, *Journal of the American Chemical Society*, 2004, **126**, 13787–13793 (cited on page 9).

(14) A. Jain, P. Sagar and R. M. Mehra, *Solid-State Electronics*, 2006, **50**, 1420–1424 (cited on pages 9, 10, 12).

(15) H. Hung-Chun Lai, T. Basheer, V. L. Kuznetsov, R. G. Egdell, R. M. J. Jacobs, M. Pepper and P. P. Edwards, *Journal of Applied Physics*, 2012, **112**, 083708 (cited on pages 9, 60).

(16) K. G. Saw, N. M. Aznan, F. K. Yam, S. S. Ng and S. Y. Pung, *PLoS ONE*, 2015, **10**, 1–17 (cited on pages 9, 97).

(17) A. K. Das, P Misra and L. M. Kukreja, *Journal of Physics D: Applied Physics*, 2009, **42**, 165405 (cited on pages 10, 12, 112, 113, 116, 118, 124).

(18) B. E. Sernelius, K.-F. Berggren, Z.-C. Jin, I. Hamberg and C. G. Granqvist, *Physical Review B*, 1988, **37**, 244–248 (cited on page 10).

(19) J. G. Lu, S. Fujita, T. Kawaharamura, H. Nishinaka, Y. Kamada, T. Ohshima, Z. Z. Ye, Y. J. Zeng, Y. Z. Zhang, L. P. Zhu, H. P. He and B. H. Zhao, *Journal of Applied Physic*s, 2007, **101**, 083705 (cited on pages 10, 13).

(20) B. K. Meyer, H. Alves, D. M. Hofmann, W. Kriegseis, D. Forster, F. Bertram, J. Christen, A. Hoffmann, M. Straßburg, M. Dworzak, U. Haboeck and A. V. Rodina, *Physica Status Solidi (B) Basic Research*, 2004, **241**, 231–260 (cited on pages 10, 12).

(21) I. Hamberg, C. G. Granqvist, K. F. Berggren, B. E. Sernelius and L. Engström, *Physical Review B*, 1984, **30**, 3240–3249 (cited on page 10).

(22) M. R. Waugh, G. Hyett and I. P. Parkin, *Chemical Vapor Deposition*, 2008, **14**, 366–372 (cited on page 10).

(23) A. Jiménez-González and R. Suárez-Parra, *Journal of Crystal Growth*, 1996, **167**, 649–655 (cited on page 10).

(24) S. Y. Myonga and K. S. Lim, *Applied Physics Letters*, 2003, **82**, 3026–3028 (cited on page 10).

(25) G. D. Mahan, *Journal of Applied Physics*, 1980, **51**, 2634–2646 (cited on page 10).

(26) S. C. Jain, J. M. McGregor and D. J. Roulston, *Journal of Applied Physics*, 1990, **68**, 3747–3749 (cited on page 12).

(27) T. Maruyama and K. Fukui, *Thin Solid Films*, 1991, **203**, 297–302 (cited on page 15).

(28) J Kane and H. P. Schweizer, *Thin Solid Films*, 1975, **29**, 155–163 (cited on page 15).

(29) K. Chopra, S. Major and D. Pandya, *Thin Solid Films*, 1983, **102**, 1–46 (cited on page 15).

(30) H. Kim, C. M. Gilmore, A. Pique, J. S. Horwitz, H. Mattoussi, H. Murata, Z. H. Kafafi and D. B. Chrisey, *Journal of Applied Physics*, 1999, **86**, 6451–6461 (cited on page 15).

(31) T. Minami, *Semiconductor Science and Technology*, 2005, **20**, S35–S44 (cited on pages 16, 20).

(32) I. A. Rauf, *Journal of Applied Physics*, 1996, **79**, 4057 (cited on page 16).

(33) Y. Sawada, C. Kobayashi, S. Seki and H. Funakubo, *Thin Solid Films*, 2002, **409**, 46–50 (cited on page 16).

(34) Y. Shigesato, S. Takaki and T. Haranoh, *Journal of Applied Physics*, 1992, **71**, 3356–3364 (cited on page 16).

(35) P. Gerhardinger and D. Strickler, *Key Engineering Materials*, 2008, **380**, 169 (cited on page 16).

(36) S. A. Yousif and J. M. Abass, *International Letters of Chemistry, Physics and Astronomy*, 2013, **13**, 90–102 (cited on page 16).

(37) Z. Banyamin, P. Kelly, G. West and J. Boardman, *Coatings*, 2014, **4**, 732–746 (cited on pages 16, 168).

(38) D. S. Bhachu, M. R. Waugh, K. Zeissler, W. R. Branford and I. P. Parkin, *Chemistry - A European Journal*, 2011, **17**, 11613–11621 (cited on pages 16, 35, 81, 97, 162).

(39) J. Suffner, P. Ágoston, J. Kling and H. Hahn, *Journal of Nanoparticle Research*, 2010, **12**, 2579–2588 (cited on page 16).

(40) A. Ortiz, S. Lopez and E. Martinez, *Solar Energy Materials*, 1989, **18**, 143–149 (cited on page 16).

(41) A. Bhardwaj, B. Gupta, A. Raza, A. Sharma and O. Agnihotri, *Solar Cells*, 1981, **5**, 39–49 (cited on page 16).

(42) S. Shanthi, C. Subramanian and P. Ramasamy, *Materials Science and Engineering: B*, 1999, **57**, 127–134 (cited on page 16).

(43) S. Suh, Z. Zhang, W.-K. Chu and D. M. Hoffman, *Thin Solid Films*, 1999, **345**, 240–243 (cited on pages 16, 168).

(44) A. Gupta, D. K. Pandya and S. C. Kashyap, *Japanese Journal of Applied Physics*, 2004, **43**, L1592–L1594 (cited on page 16).

(45) N. Noor and I. P. Parkin, *Journal of Materials Chemistry C*, 2013, **1**, 984 (cited on pages 16, 85, 98, 128, 162–164, 168).

(46) U.S. Geological Survey, *Mineral Commodity Summaries*, 1998, 199 (cited on page 17).

(47) U.S. Geological Survey, *Mineral Commodity Summaries*, 1999, 199 (cited on page 17).

(48) U.S. Geological Survey, *Mineral Commodity Summaries*, 2000, 196 (cited on page 17).

(49) U.S. Geological Survey, *Mineral Commodity Summaries*, 2001, 192 (cited on page 17).

(50) U.S. Geological Survey, *Mineral Commodity Summaries*, 2002, 197 (cited on page 17).

(51) U.S. Geological Survey, *Mineral Commodity Summaries*, 2003, 199 (cited on page 17).

(52) U.S. Geological Survey, *Mineral Commodity Summaries*, 2004, 197 (cited on page 17).

(53) U.S. Geological Survey, *Mineral Commodity Summaries*, 2005, 197 (cited on page 17).

(54) U.S. Geological Survey, *Mineral Commodity Summaries*, 2006, 199 (cited on page 17).

(55) U.S. Geological Survey, *Mineral Commodity Summaries*, 2007, 195 (cited on page 17).

(56) U.S. Geological Survey, *Mineral Commodity Summaries*, 2008, 199 (cited on page 17).

(57) U.S. Geological Survey, *Mineral Commodity Summaries*, 2009, 195 (cited on page 17).

(58) U.S. Geological Survey, *Mineral Commodity Summaries*, 2010, 193 (cited on page 17).

(59) U.S. Geological Survey, *Mineral Commodity Summaries*, 2011, 198 (cited on page 17).

(60) U.S. Geological Survey, *Mineral Commodity Summaries*, 2012, 198 (cited on page 17).

(61) U.S. Geological Survey, *Mineral Commodity Summaries*, 2013, 198 (cited on page 17).

(62) U.S. Geological Survey, *Mineral Commodity Summaries*, 2014, 196 (cited on page 17).

(63) U.S. Geological Survey, *Mineral Commodity Summaries*, 2015, 196 (cited on page 17).

(64) U.S. Geological Survey, *Mineral Commodity Summaries*, 2016, 202 (cited on page 17).

(65) U.S. Geological Survey, *Mineral Commodity Summaries*, 2017, 202 (cited on page 17).

(66) K Ellmer, *Journal of Physics D: Applied Physics*, 2001, **34**, 3097–3108 (cited on page 17).

(67) H. Morkoc and U. Ozgur, *Zinc Oxide: Fundamentals, Materials and Device Technology*, Wiley-VCH Verlag GmbH & Co. KGaA, 2009 (cited on pages 18, 20).

(68) D. Look, D. Reynolds, J. Sizelove, R. Jones, C. Litton, G. Cantwell and W. Harsch, *Solid State Communications*, 1998, **105**, 399–401 (cited on page 18).

(69) D. C. Look, J. W. Hemsky and J. R. Sizelove, *Physical Review Letters*, 1999, **82**, 2552–2555 (cited on page 18).

(70) A. Janotti and C. G. Van De Walle, *Physical Review B - Condensed Matter and Materials Physics*, 2007, **76**, 1–22 (cited on pages 18, 71).

(71) P. Gondoni, M. Ghidelli, F. Di Fonzo, V. Russo, P. Bruno, J. Martí-Rujas, C. E. Bottani, A. Li Bassi and C. S. Casari, *Thin Solid Films*, 2012, **520**, 4707–4711 (cited on pages 18, 60).

(72) F. Oba, A. Togo, I. Tanaka, J. Paier and G. Kresse, *Physical Review B - Condensed Matter and Materials Physics*, 2008, **77**, 3–8 (cited on pages 18, 83).

(73) A. Janotti and C. G. Van De Walle, *Applied Physics Letters*, 2005, **87**, 1–3 (cited on page 18).

(74) D. H. Kim, G. W. Lee and Y. C. Kim, *Solid State Communications*, 2012, **152**, 1711–1714 (cited on page 18).

(75) C. G. Van De Walle, *Physical Review Letters*, 2000, **85**, 1012–1015 (cited on page 20).

(76) P. D. C. King and T. D. Veal, *Journal of Physics: Condensed Matter*, 2011, **23**, 334214 (cited on page 20).

(77) A. Janotti and C. G. Van de Walle, *Nature Materials*, 2007, **6**, 44–47 (cited on page 20).

(78) H. Q. Le and S. J. Chua, *Journal of Physics D: Applied Physics*, 2011, **44**, 125104 (cited on pages 20, 86).

(79) C. R. A. Catlow, A. A. Sokol and A. Walsh, *Chemical Communications*, 2011, **47**, 3386 (cited on page 20).

(80) A. Janotti and C. G. Van de Walle, *Reports on Progress in Physics*, 2009, **72**, 126501 (cited on pages 20–22).

(81) U Ozgur, Y. I. Alivov, C. Liu, A. Teke, M. A. Reshchikov, S. Dogan, V. Avrutin, S. J. Cho and H. Morko, *Journal of Applied Physics*, 2005, **98**, 1–103 (cited on page 21).

(82) L. V. Butov, *Superlattices and Microstructures*, 2017, **108**, 2–26 (cited on page 21).

(83) D. F. Paraguay, L. W. Estrada, N. D. R. Acosta, E. Andrade and M. Miki-Yoshida, *Thin Solid Films*, 1999, **350**, 192–202 (cited on page 21).

(84) J. G. Wilkes, E. D. Conte, Y. Kim, M. Holcomb, J. B. Sutherland and D. W. Miller, *Journal of Chromatography A*, 2000, **880**, 3–33 (cited on page 21).

(85) K. Eda, *IEEE Electrical Insulation Magazine*, 1989, **5**, 28–30 (cited on page 22).

(86) K Choy, *Progress in Materials Science*, 2003, **48**, 57–170 (cited on pages 23, 25, 32, 33, 41).

(87) B. Eckhardt, *Philosophical Transactions of the Royal Society A*, 2009, **367**, 449–455 (cited on page 23).

(88) W.-M. Zhang, G. Meng and X. Wei, *Microfluid Nanofluid*, 2012, **13**, 845–882 (cited on pages 23, 24).

(89) T. T. Kodas and M. J. Hampden-smith, in *The Chemistry of Metal CVD*, 1994, ch. 9, pp. 429–498 (cited on pages 24, 31).

(90) P. J. Mohr and B. N. Taylor, *Review of Modern Physics*, 2012, **84**, 1527–1605 (cited on pages 24, 28).

(91) X.-T. Yan and Y. Xu, *Chemical Vapour Deposition: An Intergrated Engineering Design Approach*, Springer-Verlag London, 1st edn., 2010, ch. 2 (cited on pages 24, 25).

(92) A. Rockett, *The Materials Science of Semiconductors*, Springer Science+Business Media, 1st edn., 2008, pp. 1–662 (cited on pages 25, 30, 34, 55).

(93) C. He and G. Ahmadi, *Aerosol Science and Technology*, 1998, **29**, 525–546 (cited on page 26).

(94) J. K. Platten, *Journal of Applied Mechanics*, 2006, **73**, 5 (cited on page 26).

(95) S. Duhr and D. Braun, *Proceedings of the National Academy of Sciences of the United States of America*, 2006, **103**, 19678–82 (cited on pages 26, 27).

(96) M. Eslamian and M. Z. Saghir, *International Journal of Thermal Sciences*, 2014, **80**, 58–64 (cited on page 26).

(97) X.-T. Yan and Y. Xu, *Chemical Vapour Deposition: An Integrated Engineering Design for Advanced Materials*, Springer London, 2010 (cited on pages 28, 30).

(98) H. O. Pierson, *Handbook of Chemical Vapor Deposition: Principles, Technology and Applications*, Noyes Publications, New York, 2nd edn., 1999 (cited on pages 30, 156).

(99) G Job and F Herrmann, *European Journal of Physics*, 2006, **27**, 353–371 (cited on page 30).

(100) N. M. Hwang and D. Y. Yoon, *Journal of Materials Science Letters*, 1994, **13**, 1437–1439 (cited on page 30).

(101) A. C. Jones and M. L. Hitchman, *Overview of Chemical Vapour Deposition*, Royal Society of Chemistry, 1st edn., 2008 (cited on pages 31–33, 35).

(102) A. G. Rajan, J. H. Warner, D. Blankschtein and M. S. Strano, *ACS Nano*, 2016, **10**, 4330–4344 (cited on page 31).

(103) C Bernard, E Blanquet and M Pons, *Surface and Coatings Technology*, 2007, **202**, 790–797 (cited on page 32).

(104) K. Seshan, *Handbook of Thin-Film Deposition Processes and Techniques*, Noyes Publications, Norwich, New York, Second, 2000, vol. 31, pp. 1–629 (cited on pages 32, 54).

(105) J.-O. Carlsson, *Handbook of Deposition Technologies for Films and Coatings*, William Andrew, 3rd edn., 2010 (cited on page 34).

(106) X. Hou and K.-L. Choy, *Chemical Vapor Deposition*, 2006, **12**, 583–596 (cited on pages 38, 39, 105).

(107) A. Gurav, T. Kodas, T. Pluym and Y. Xiong, *Aerosol Science and Technology*, 1993, **19**, 411–452 (cited on page 38).

(108) J. N. Smith, R. C. Flagan and J. L. Beauchamp, *Journal of Physical Chemistry A*, 2000, **106**, 9957–9967 (cited on page 39).

(109) A. Gomez and G. Chen, *Combustion Science and Technology*, 1994, **96**, 47–59 (cited on page 40).

(110) P. Marchand, I. A. Hassan, I. P. Parkin and C. J. Carmalt, *Dalton Transactions*, 2013, **42**, 9406–22 (cited on pages 40, 98).

(111) C. E. Knapp and C. J. Carmalt, *Chem. Soc. Rev.*, 2016, **45**, 1036–1064 (cited on page 40).

(112) M. J. Powell, D. B. Potter, R. L. Wilson, J. A. Darr, I. P. Parkin and C. J. Carmalt, *Materials & Design*, 2017, **129**, 116–124 (cited on pages 41, 85, 128, 149, 162).

(113) S. O'Brien, M. G. Nolan, M. Çopuroglu, J. a. Hamilton, I. Povey, L. Pereira, R. Martins, E. Fortunato and M. Pemble, *Thin Solid Films*, 2010, **518**, 4515–4519 (cited on page 44).

(114) A. Hadri, M. Taibi, M. Loghmarti, C. Nassiri, T. Slimani Tlemçani and A. Mzerd, *Thin Solid Films*, 2016, **601**, 7–12 (cited on page 44).

(115) D. O. Scanlon, C. W. Dunnill, J Buckeridge, S. A. Shevlin, A. J. Logsdail, S. M. Woodley, C. R. A. Catlow, M. J. Powell, R. G. Palgrave, I. P. Parkin, G. W. Watson, T. W. Keal, P Sherwood, A Walsh and A. A. Sokol, *Nature Materials*, 2013, **12**, 798–801 (cited on page 45).

(116) T. Luttrell, S. Halpegamage, J. Tao, A. Kramer, E. Sutter and M. Batzill, *Scientific Reports*, 2014, **4**, 4043 (cited on page 46).

(117) J. Zhang, P. Zhou, J. Liu and J. Yu, *Physical Chemistry Chemical Physics*, 2014, **16**, 20382–20386 (cited on page 46).

(118) W. H. Miller, *A Treatise on Crystallography*, For J. & J. J. Deighton, 1839 (cited on page 46).

(119) B. Averill and P. Eldredge, *Chemistry: Principles, Patterns, and Applications*, Pearson/Prentice Hall, 1st edn., 2006, p. 2365 (cited on page 46).

(120) A. L. Patterson, *Physical Review*, 1939, **56**, 978–982 (cited on page 48).

(121) J. Langford and A. Wilson, *J. Appl. Cryst.*, 1978, **11**, 102–113 (cited on page 48).

(122) S. J. S. Qazi, A. R. Rennie, J. K. Cockcroft and M. Vickers, *Journal of Colloid and Interface Science*, 2009, **338**, 105–110 (cited on page 48).

(123) A. Larson and R. V. Dreele, *General Structure Analysis System (GSAS)*, tech. rep., 2000, LAUR 86–748 (cited on page 48).

(124) B. H. Toby, *Journal of Applied Crystallography*, 2001, **34**, 210–213 (cited on page 48).

(125) W. D. Callister, *Materials Science and Engineering: An Introduction*, John Wiley & Sons, 7th edn., 2007 (cited on page 52).

(126) B. Faust, *Modern Chemical Techniques*, Royal Society of Chemistry, 1st edn., 1997, p. 200 (cited on page 52).

(127) M. F. Al-Kuhaili, S. M. Durrani, A. S. El-Said and R. Heller, *Journal of Materials Research*, 2016, 1–10 (cited on page 53).

(128) E. H. Hall, *American Journal of Mathematics*, 1879, **2**, 287–292 (cited on page 53).

(129) T. Ohgaki, N. Ohashi, S. Sugimura, H. Ryoken, I. Sakaguchi, Y. Adachi and H. Haneda, *Journal of Materials Research*, 2008, **23**, 2293–2295 (cited on page 55).

(130) L. J. van der Pauw, *Philips Technical Review*, 1958, **20**, 220–224 (cited on page 55).

(131) T. Minami, H. Sato, H. Nanto and S. Takata, *Japanese Journal of Applied Physics*, 1985, **24**, L781–L784 (cited on page 60).

(132) E. Fortunato, V. Assunção, A. Gonçalves, A. Marques, H. Águas, L. Pereira, I. Ferreira, P. Vilarinho and R. Martins, *Thin Solid Films*, 2004, **451-452**, 443–447 (cited on page 60).

(133) M. Kon, P. K. Song, Y. Shigesato, P. Frach, A. Mizukami and K. Suzuki, *Japanese Journal of Applied Physics*, 2002, **41**, 814–819 (cited on page 60).

(134) R. Hong and S. Xu, *Journal of Materials Science and Technology*, 2010, **26**, 872–877 (cited on page 60).

(135) H. Zhu, E. Bunte, J. Hüpkes, H. Siekmann and S. M. Huang, *Thin Solid Films*, 2009, **517**, 3161–3166 (cited on page 60).

(136) S. Fernandez, A. Martinez-Steele, J. J. Gandia and F. B. Naranjo, *Thin Solid Films*, 2009, **517**, 3152–3156 (cited on page 60).

(137) L.-Y. Lin, M.-C. Jeong, D.-E. Kim and J.-M. Myoung, *Surface and Coatings Technology*, 2006, **201**, 2547–2552 (cited on page 60).

(138) K. Djessas, I. Bouchama, J. L. Gauffier and Z. B. Ayadi, *Thin Solid Films*, 2014, **555**, 28–32 (cited on page 60).

(139) D. Zhu, Q. Wang, S. Han, P. Cao, W. Liu, F. Jia, Y. Zeng, X. Ma and Y. Lu, *Applied Surface Science*, 2014, **298**, 208–213 (cited on page 60).

(140) K.-W. Seo, H.-S. Shin, J.-H. Lee, K.-B. Chung and H.-K. Kim, *Vacuum*, 2014, **101**, 250–256 (cited on pages 60, 86).

(141) J.-A. Jeong, H.-S. Shin, K.-H. Choi and H.-K. Kim, *Journal of Physics D: Applied Physics*, 2010, **43**, 465403 (cited on page 60).

(142) Y.-D. Ko, K.-C. Kim and Y.-S. Kim, *Superlattices and Microstructures*, 2012, **51**, 933–941 (cited on pages 60, 97).

(143) Z. Ben Ayadi, H. Mahdhi, K. Djessas, J. L. Gauffier, L. El Mir and S. Alaya, *Thin Solid Films*, 2014, **553**, 123–126 (cited on page 60).

(144) T. Ohgaki, Y. Kawamura, T. Kuroda, N. Ohashi, Y. Adachi, T. Tsurumi, F. Minami and H. Haneda, *Key Engineering Materials*, 2003, **248**, 91–94 (cited on page 60).

(145) L. Mandalapu, F. Xiu, Z. Yang and J. Liu, *Solid-State Electronics*, 2007, **51**, 1014–1017 (cited on page 60).

(146) C.-Y. Chen, L.-H. Hsiao and J.-I. Chyi, *Journal of Crystal Growth*, 2015, **425**, 216–220 (cited on page 60).

(147) C. S. Yeh, C. C. Kuo, B. R. Huang and S Dhar, *Journal of Optoelectronics and Advanced Materials*, 2005, **7**, 3039–3046 (cited on page 60).

(148) H. Agura, A. Suzuki, T. Matsushita, T. Aoki and M. Okuda, *Thin Solid Films*, 2003, **445**, 263–267 (cited on page 60).

(149) G. Socol, D. Craciun, I. Mihailescu, N. Stefan, C. Besleaga, L. Ion, S. Antohe, K. Kim, D. Norton, S. Pearton, a.C. Galca and V. Craciun, *Thin Solid Films*, 2011, **520**, 1274–1277 (cited on page 60).

(150) S.-M. Park, T. Ikegami and K. Ebihara, *Thin Solid Films*, 2006, **513**, 90–94 (cited on page 60).

(151) S. Jin-Hyun, S. Dong-Kyun, L. HeeYoung, L. Jai-Yeoul, C. Nam-In and L. Se-Jong, *Journal of the Korean Physical Society*, 2009, **55**, 947 (cited on pages 60, 86).

(152) J. A. Sans, J. F. Sánchez-Royo, A. Segura, G. Tobias and E. Canadell, *Physical Review B*, 2009, **79**, 195105 (cited on page 60).

(153) J.-H. Kim and S.-M. Koo, *Ceramics International*, 2015, **41**, 37–42 (cited on pages 60, 97).

(154) C.-F. Yu, S.-H. Chen, S.-J. Sun and H. Chou, *Applied Surface Science*, 2011, **257**, 6498–6502 (cited on pages 60, 64, 70).

(155) Y. Hou, A. M. Soleimanpour and A. H. Jayatissa, *Sensors and Actuators, B: Chemical*, 2013, **177**, 761–769 (cited on page 60).

(156) M. J. Alam and D. C. Cameron, *Journal of Vacuum Science & Technology A: Vacuum, Surfaces, and Films*, 2001, **19**, 1642–1646 (cited on page 60).

(157) V. Fathollahi and M. M. Amini, *Materials Letters*, 2001, **50**, 235–239 (cited on page 60).

(158) I. Y. Y. Bu, *Materials Science in Semiconductor Processing*, 2014, **27**, 19–25 (cited on page 60).

(159) M. Ohyama, H. Kozuka and T. Yoko, *Journal of the American Ceramic Society*, 2005, **81**, 1622–1632 (cited on pages 60, 73).

(160) I. Y. Y. Bu, *Ceramics International*, 2014, **40**, 11941–11946 (cited on page 60).

(161) W Tang and D. C. Cameron, *Thin Solid Films*, 1994, **238**, 83–87 (cited on page 60).

(162) W. J. Maeng and J.-S. Park, *Journal of Electroceramics*, 2013, **31**, 338–344 (cited on page 60).

(163) A. Illiberi, R. Scherpenborg, M. Theelen, P. Poodt and F. Roozeboom, *Journal of Vacuum Science & Technology A: Vacuum, Surfaces, and Films*, 2013, **31**, 061504 (cited on page 60).

(164) P. R. Chalker, P. A. Marshall, S. Romani, J. W. Roberts, S. J. C. Irvine, D. A. Lamb, A. J. Clayton and P. A. Williams, *Journal of Vacuum Science & Technology A: Vacuum, Surfaces, and Films*, 2013, **31**, 01A120 (cited on page 60).

(165) H. Saarenpää, T. Niemi, A. Tukiainen, H. Lemmetyinen and N. Tkachenko, *Solar Energy Materials and Solar Cells*, 2010, **94**, 1379–1383 (cited on page 60).

(166) S. C. Gong, J. G. Jang, H. J. Chang and J.-S. Park, *Synthetic Metals*, 2011, **161**, 823–827 (cited on page 60).

(167) G. Luka, L. Wachnicki, B. Witkowski, T. Krajewski, R. Jakiela, E. Guziewicz and M. Godlewski, *Materials Science and Engineering: B*, 2011, **176**, 237–241 (cited on pages 60, 73).

(168) T. Dhakal, A. S. Nandur, R. Christian, P. Vasekar, S. Desu, C. Westgate, D. I. Koukis, D. J. Arenas and D. B. Tanner, *Solar Energy*, 2012, **86**, 1306–1312 (cited on page 60).

(169) S Edinger, N Bansal, M Bauch, R. A. Wibowo, G Ujvari, R Hamid, G Trimmel and T Dimopoulos, *Journal of Materials Science*, 2017, **52**, 8591–8602 (cited on pages 60, 65).

(170) S. Major, A. Banerjee and K. Chopra, *Thin Solid Films*, 1983, **108**, 333–340 (cited on pages 60, 65).

(171) A. Aktaruzzaman, G. Sharma and L. Malhotra, *Thin Solid Films*, 1991, **198**, 67–74 (cited on page 60).

(172) N. Islam, T. B. Ghosh, K. L. Chopra and H. N. Acharya, *Thin Solid Films*, 1996, **280**, 20–25 (cited on page 60).

(173) M. Miki-Yoshida, F. Paraduay-Delgado, Q. Estrada-Lopez and E. Andrade, *Thin Solid Films*, 2000, **376**, 99–109 (cited on pages 60, 65, 73).

(174) O. Makuku, F. Mbaiwa and T. Sathiaraj, *Ceramics International*, 2016, **42**, 14581–14586 (cited on pages 60, 86).

(175) J Morales, W. L. Estrada, E Andrade and M Miki-yoshida, *Thin Solid Films*, 2000, **366**, 16–27 (cited on pages 60, 65).

(176) K. Nakahara, K. Tamura, M. Sakai, D. Nakagawa, N. Ito, M. Sonobe, H. Takasu, H. Tampo, P. Fons, K. Matsubara, K. Iwata, A. Yamada and S. Niki, *Japanese Journal of Applied Physics, Part 2: Letters*, 2004, **43** (cited on page 60).

(177) J. Nishino, T. Kawarada, S. Ohshio, H. Saitoh, K. Maruyama and K. Kamata, *Journal of Materials Science Letters*, 1997, **16**, 2887–2890 (cited on page 60).

(178) J. Hu and R. G. Gordon, *Journal of Applied Physics*, 1992, **71**, 880–890 (cited on page 60).

(179) J. Hu and R. G. Gordon, *Journal of Applied Physics*, 1992, **72**, 5381–5392 (cited on page 60).

(180) T. Terasako, Y. Ogura, K. Ohmae, S. Fujimoto, M. Yagi and S. Shirakata, *Surface & Coatings Technology*, 2013, **230**, 245–253 (cited on page 60).

(181) Y.-C. Huang, Z.-Y. Li, H.-h. Chen, W.-Y. Uen, S.-M. Lan, S.-M. Liao, Y.-H. Huang, C.-T. Ku, M.-C. Chen, T.-N. Yang and C.-C. Chiang, *Thin Solid Films*, 2009, **517**, 5537–5542 (cited on page 60).

(182) H. Jung, D. Kim and H. Kim, *Applied Surface Science*, 2014, **297**, 125–129 (cited on pages 60, 70).

(183) D. Kim, I. Yun and H. Kim, *Current Applied Physics*, 2010, **10**, S459–S462 (cited on page 60).

(184) J. D. Ye, S. L. Gu, S. M. Zhu, S. M. Liu, Y. D. Zheng, R. Zhang, Y. Shi, H. Q. Yu and Y. D. Ye, *Journal of Crystal Growth*, 2005, **283**, 279–285 (cited on page 60).

(185) A. Nebatti, C. Pflitsch, B. Curdts and B. Atakan, *Materials Science in Semiconductor Processing*, 2015, **39**, 467–475 (cited on pages 60, 86).

(186) C. H. Lee and D. W. Kim, *Journal of Electroceramics*, 2014, **33**, 12–16 (cited on page 60).

(187) J. A. Manzi, C. E. Knapp, I. P. Parkin and C. J. Carmalt, *Thin Solid Films*, 2016, **616**, 477–481 (cited on pages 60, 64, 106, 161).

(188) M. Nolan, J. Hamilton, S. O'Brien, G. Bruno, L. Pereira, E. Fortunato, R. Martins, I. Povey and M. Pemble, *Journal of Photochemistry and Photobiology A: Chemistry*, 2011, **219**, 10–15 (cited on pages 60, 85, 161).

(189) S. D. Ponja, S. Sathasivam, I. P. Parkin and C. J. Carmalt, *RSC Advances*, 2014, **4**, 49723–49728 (cited on pages 60, 63, 71, 84, 125, 127).

(190) D. S. Bhachu, G. Sankar and I. P. Parkin, *Chemistry of Materials*, 2012, **24**, 4704–4710 (cited on pages 60, 61, 63, 76, 84).

(191) S. Chen, N. Noor, I. P. Parkin and R. Binions, *J. Mater. Chem. A*, 2014, **2**, 17174–17182 (cited on pages 60, 85).

(192) S. Chen, G. Carraro, D. Barreca and R. Binions, *Thin Solid Films*, 2014, **584**, 316–319 (cited on pages 60, 63, 84, 93).

(193) S. Kuprenaite, T. Murauskas, A. Abrutis, V. Kubilius, Z. Saltyte and V. Plausinaitiene, *Surface and Coatings Technology*, 2014, **271**, 156–164 (cited on pages 60, 101).

(194) A. Dadgar, N. Oleynik, D. Forster, S. Deiter, H. Witek, J. Bläsing, F. Bertram, A. Krtschil, A. Diez, J. Christen and A. Krost, *Journal of Crystal Growth*, 2004, **267**, 140–144 (cited on page 60).

(195) R. Wang, L. L. H. King and A. W. Sleight, *Journal of Materials Research*, 2011, **11**, 1659–1664 (cited on page 61).

(196) G. Walters and I. Parkin, *Applied Surface Science*, 2009, **255**, 6555–6560 (cited on page 61).

(197) N. Fujimura, T. Nishihara, S. Goto, J. Xu and T. Ito, *Journal of Crystal Growth*, 1993, **130**, 269–279 (cited on page 63).

(198) Y. Kajikawa, *Journal of Crystal Growth*, 2006, **289**, 387–394 (cited on pages 64, 80).

(199) A. Gulino, I. Fragala, S. Chimiche and V. A. Doria, *Chemistry of Materials*, 2002, **14**, 116–121 (cited on pages 64, 70, 71, 73).

(200) R. K. Shukla, A. Srivastava, A. Srivastava and K. C. Dubey, *Journal of Crystal Growth*, 2006, **294**, 427–431 (cited on page 64).

(201) D. S. Y. Jayathilake, T. A. N. Peiris, J. Sagu, D. B. Potter, K. G. U. Wijayantha, C. J. Carmalt and D. J. Southee, *ACS Sustainable Chemistry & Engineering*, 2017, **5**, 4820–4829 (cited on pages 64, 72, 73).

(202) M. Krunks and E. Mellikov, *Thin Solid Films*, 1995, **270**, 33–36 (cited on page 65).

(203) P. Nunes, E. Fortunato, P. Tonello, F. Braz Fernandes, P. Vilarinho and R. Martins, *Vacuum*, 2002, **64**, 281–285 (cited on page 65).

(204) D. Goyal, C. Agashe, M. Takwale, V. Bhide, S. Mahamuni and S. Kulkarni, *Journal of Materials Research*, 1993, **8**, 1052–1056 (cited on pages 65, 70).

(205) M. P. Taylor, D. W. Readey, M. F.A. M. Van Hest, C. W. Teplin, J. L. Alleman, M. S. Dabney, L. M. Gedvilas, B. M. Keyes, B. To, J. D. Perkins and D. S. Ginley, *Advanced Functional Materials*, 2008, **18**, 3169–3178 (cited on page 66).

(206) L.-p. Wang, F. Zhang, S. Chen and Z.-h. Bai, *International Journal of Minerals, Metallurgy, and Materials*, 2017, **24**, 455–461 (cited on page 66).

(207) K. Tang, S. Gu, J. Liu, J. Ye, S. Zhu and Y. Zheng, *Journal of Alloys and Compounds*, 2015, **653**, 643–648 (cited on page 66).

(208) H. M. Rietveld, *Acta Crystallographica*, 1967, **22**, 151–152 (cited on page 66).

(209) H. M. Rietveld, *A profile refinement method for nuclear and magnetic structures*, 1969 (cited on page 66).

(210) A. Le Bail, H. Duroy and J. L. Fourquet, *Materials Research Bulletin*, 1988, **23**, 447–452 (cited on page 66).

(211) A. Nakrela, N. Benramdane, A. Bouzidi, Z. Kebbab, M. Medles and C. Mathieu, *Results in Physics*, 2016, **6**, 133–138 (cited on page 67).

(212) S. Basharat, C. J. Carmalt, S. A. Barnett, D. A. Tocher and H. O. Davies, *Inorganic Chemistry*, 2007, **46**, 9473–9480 (cited on page 68).

(213) S. Basharat, C. J. Carmalt, R. Binions, R. Palgrave and I. P. Parkin, *Dalton transactions (Cambridge, England : 2003)*, 2008, **9226**, 591–595 (cited on pages 68, 162).

(214) W. R. Theis, *Zeitschrift für Physik A*, 1979, **358**, 355–358 (cited on page 69).

(215) G Beck and N. Davidovich, *Il Nuovo Cimento B*, 1975, **27**, 19–26 (cited on page 69).

(216) G Dresselhaus, *Physical Review*, 1955, **100**, 580–586 (cited on page 69).

(217) R. J. Elliott, *Physical Review*, 1954, **96**, 266–279 (cited on page 69).

(218) N. H. Nguyen Tran, H. T. Nguyen, Y.-R. Liu, M. Aminzare, A. T. T. Pham, S. Cho, D. P. Wong, K.-H. Chen, T. Seetawan, N. K. Pham, H. K. T. Ta, C. V. Tran and T. B. Phan, *ACS Applied Materials & Interfaces*, 2016, **8**, 33916–33923 (cited on pages 70, 86, 87, 90).

(219) S. Chirakkara and S. B. Krupanidhi, *physica status solidi (RRL) - Rapid Research Letter*s, 2012, **6**, 34–36 (cited on pages 70, 86).

(220) J. H. Lim, S. M. Lee, H.-S. Kim, H. Y. Kim, J. Park, S.-B. Jung, G. C. Park, J. Kim and J. Joo, *Scientific Reports*, 2017, **7**, 41992 (cited on pages 70, 86, 93).

(221) K. Mun Wong, S. M. Alay-E-Abbas, Y. Fang, A. Shaukat and Y. Lei, *Journal of Applied Physics*, 2013, **114**, 034901 (cited on page 70).

(222) B. Deng, A. Luisa da Rosa, T. Frauenheim, J. P. Xiao, X. Q. Shi, R. Q. Zhang and M. a. Van Hove, *Nanoscale*, 2014, **6**, 11882–6 (cited on page 71).

(223) G. Y. Huang, C. Y. Wang and J. T. Wang, *Solid State Communications*, 2009, **149**, 199–204 (cited on page 71).

(224) J. Carrasco, N. Lopez and F. Illas, *Physical Review Letters*, 2004, **93**, 3–6 (cited on page 71).

(225) W. Theis and K. Horn, *Physical Review B*, 1993, **47**, 60–63 (cited on page 71).

(226) C. Berg, S. Raaen, A. Borg, J. N. Andersen, E. Lundgren and R. Nyholm, *Physical Review B*, 1993, **47**, 13063–13066 (cited on page 71).

(227) A. C. Miller, F. P. Mccluskey and J. A. Taylor, *Journal of Vacuum Science & Technology A: Vacuum, Surfaces, and Films*, 1991, **1461**, 1461–1465 (cited on page 71).

(228) R Hauert, J Patscheider, M. Tobler and R. Zehringer, *Surface Science*, 1993, **292**, 121–129 (cited on page 72).

(229) K. Domen and T. J. Chuang, *The Journal of Chemical Physics*, 1989, **90**, 3318–3331 (cited on page 72).

(230) G. L. Lay, D. Mao, A. Kahn, Y. Hwu and G. Margaritondo, *Physical Review B*, 1991, **43** (cited on page 72).

(231) P. R. Varekamp, M. C. Håkansson, J. Kanski, D. K. Shuh, M. Björkqvist, M. Gothelid, W. C. Simpson, U. O. Karlsson and J. A. Yarmoff, *Physical Review B*, 1996, **54**, 2101–2113 (cited on page 72).

(232) D. Mao, M. Santos, M. Shayegan, A. Kahn, G. L. Lay, Y. Hwu, G. Margaritondo, L. T. Florez and J. P. Harbison, *Physica B*, 1992, **45**, 1273–1283 (cited on page 72).

(233) G. Cossu, G. M. Ingo, G. Mattogno, G. Padeletti and G. M. Proietti, *Applied Surface Science*, 1992, **56-58**, 81–88 (cited on page 72).

(234) R. Carli and C. L. Bianchi, *Applied Surface Science*, 1994, **74**, 99–102 (cited on page 72).

(235) S. Evans, *Surface and Interface Analysis*, 1985, **7**, 299–302 (cited on page 72).

(236) G Leonhardt, A Berndtsson, J Hedman, M Klasson, R Nilsson and C Nordling, *Physica Status Solidi B.*, 1973, **241**, 241–248 (cited on page 72).

(237) M Pessa, A Vuoristo, M Vulli and S Aksela, *Physical Review B*, 1979, **20**, 3115–3123 (cited on page 72).

(238) J. C. Fan and J. B. Goodenough, *Journal of Applied Physics*, 1977, **48**, 3524–3531 (cited on page 72).

(239) L. L. Kazmerski, O. Jamjoum, P. J. Ireland and S. K. Deb, *Journal of Vacuum Science and Technology*, 1981, **19**, 467–471 (cited on page 72).

(240) A. W. C. Lin, N. R. Armstrong and T. Kuwana, *Analytical Chemistry*, 1977, **49**, 1228–1235 (cited on page 72).

(241) D. Cahen, P. J. Ireland, L. L. Kazmerski and F. A. Thiel, *Journal of Applied Physics*, 1985, **57**, 4761–4771 (cited on page 72).

(242) G. Hollinger, R. Skheyta-Kabbani and M. Gendry, *Physical Review B*, 1994, **49**, 11159–11167 (cited on page 72).

(243) S. S. Shinde, P. S. Shinde, S. M. Pawar, A. V. Moholkar, C. H. Bhosale and K. Y. Rajpure, *Solid State Sciences*, 2008, **10**, 1209–1214 (cited on page 73).

(244) A. Bosio, N. Romeo, S. Mazzamuto and V. Canevari, *Progress in Crystal Growth and Characterization of Materials*, 2006, **52**, 247–279 (cited on page 73).

(245) J.-H. Lee and B.-O. Park, *Thin Solid Films*, 2003, **426**, 94–99 (cited on page 73).

(246) J. Muller, B. Rech, J. Springer and M. Vanecek, *Solar Energy*, 2004, **77**, 917–930 (cited on page 80).

(247) K Ellmer, *Nature Photonics*, 2012, **6**, 808–816 (cited on pages 81, 167).

(248) C. G. Granqvist, *Solar Energy Materials and Solar Cells*, 2007, **91**, 1529–1598 (cited on page 81).

(249) I Chambouleyron and J. M. Martinez, in *Handbook of Thin Films Materials*, Academic Press, 2002, vol. 3, ch. 12, pp. 593–622 (cited on page 81).

(250) M. Bazzani, A. Neroni, A. Calzolari and A. Catellani, *Applied Physics Letters*, 2011, **98**, 121907 (cited on pages 82, 124).

(251) J.-Y. Noh, H. Kim, Y.-S. Kim and C. H. Park, *Journal of Applied Physics*, 2013, **113**, 153703 (cited on page 83).

(252) N. H. Nickel and M. A. Gluba, *Journal of Electronic Materials*, 2011, **40**, 440–445 (cited on page 84).

(253) R. Wu, W. Zhang, H. Zhang, D. Song, Q. Ma, J. Liu, X. Ma, L. Zhang, L. Zhang and H. Song, *Materials Science in Semiconductor Processing*, 2014, **19**, 24–31 (cited on page 86).

(254) B. Onwona-Agyeman, M. Nakao, T. Kohno, D. Liyanage, K. Murakami and T. Kitaoka, *Chemical Engineering Journal*, 2013, **219**, 273–277 (cited on page 86).

(255) R. Ebrahimifard, M. R. Golobostanfard and H. Abdizadeh, *Applied Surface Science*, 2014, **290**, 252–259 (cited on pages 86, 100).

(256) S.-C. Chang, *Nanoscale research letters*, 2014, **9**, 562 (cited on pages 86, 97).

(257) J. Liu, W. Zhang, D. Song, Q. Ma, L. Zhang, H. Zhang, L. Zhang and R. Wu, *Journal of Alloys and Compounds*, 2013, **575**, 174–182 (cited on page 86).

(258) S.-C. Chang, *International Journal of Photoenergy*, 2014, **2014**, 1–6 (cited on page 86).

(259) H. Zhao, J. He, J. Hu, S. Chen and Q. Xie, *Materials Letters*, 2016, **164**, 80–83 (cited on page 86).

(260) C. M. Hsu, W. C. Tzou, C. F. Yang and Y. J. Liou, *Materials*, 2015, **8**, 2769–2781 (cited on page 86).

(261) V. K. Jayaraman, A. M. Alvarez and M. d.l.l. O. Amador, *Physica E*, 2017, **86**, 164–167 (cited on page 86).

(262) Y. Liu, Y. Li and H. Zeng, *Journal of Nanomaterials*, 2013, **2013**, 1–9 (cited on pages 86, 97).

(263) P. Meng, J. Hu and J. He, *Materials Letters*, 2017, **195**, 209–212 (cited on page 86).

(264) T. Tohsophon, N. Wattanasupinyo, B. Silskulsuk and N. Sirikulrat, *Thin Solid Films*, 2011, **520**, 726–729 (cited on page 86).

(265) S. Teehan, H. Efstathiadis and P. Haldar, *Journal of Alloys and Compounds*, 2011, **509**, 1094–1098 (cited on pages 86, 89).

(266) V. K. Jayaraman, A. M. Álvarez, Y. M. Kuwabara, Y. Koudriavstev and M. D.L. L. Olvera Amador, *Materials Science in Semiconductor Processing*, 2016, **47**, 32–36 (cited on page 86).

(267) V. K. Jayaraman, A. Maldonado-Alvarez, A. E. Jimenez-Gonzalez and M. D.L. L. Olvera-Amador, *Materials Letters*, 2016, **181**, 52–55 (cited on page 86).

(268) S. Teehan, H. Efstathiadis and P. Haldar, *Journal of Alloys and Compounds*, 2012, **539**, 129–136 (cited on page 86).

(269) A. A. Yaroshevsky, *Geochemistry International*, 2006, **44**, 48–55 (cited on page 86).

(270) J.-i. Nomoto, M. Konagai, T. Miyata and T. Minami, *Journal of Vacuum Science & Technology A: Vacuum, Surfaces, and Films*, 2010, **28**, 861 (cited on page 87).

(271) V. Assunção, E. Fortunato, A. Marques, H. Águas, I. Ferreira, M. Costa and R. Martins, *Thin Solid Films*, 2003, **427**, 401–405 (cited on page 87).

(272) F. Urbach, *Physical Review*, 1953, **92**, 1324 –1324 (cited on page 95).

(273) F. Mozer and F. Urbach, *Physical Review*, 1956, **102**, 1519 –1523 (cited on page 95).

(274) A. S. Hassanien and A. A. Akl, *Journal of Alloys and Compounds*, 2015, **648**, 280–290 (cited on page 95).

(275) S. Schönau, F. Ruske, S. Neubert and B. Rech, *Applied Physics Letters*, 2013, **103**, 192108 (cited on page 95).

(276) N. Noor and I. P. Parkin, *Thin Solid Films*, 2013, **532**, 26–30 (cited on page 95).

(277) D. Y. Kim, R. Santbergen, K. Ja, M. Sever, J. Krc, M. Topic, S. Ha, C. Zhang, A. Heidt, M. Meier, R. A.C.M.M. V. Swaaij and M. Zeman, *Applied Materials & Interfaces*, 2014, **6** (cited on page 97).

(278) T. Minami, *MRS Bulletin*, 2000, **25**, 38–44 (cited on page 97).

(279) S. K. N, K. V. Bangera and G. K. Shivakumar, *Semiconductors*, 2015, **49**, 920–924 (cited on page 97).

(280) S. Calnan and A. N. Tiwari, *Thin Solid Films*, 2010, **518**, 1839–1849 (cited on page 97).

(281) Z. L. Pei, C. Sun, M. H. Tan, J. Q. Xiao, D. H. Guan, R. F. Huang and L. S. Wen, *Journal of Applied Physics*, 2001, **90**, 3432–3436 (cited on page 97).

(282) H. Liu, V. Avrutin, N. Izyumskaya, Ü Özgr and H. Morkoç, *Superlattices and Microstructures*, 2010, **48**, 458–484 (cited on pages 97, 111).

(283) K. Ellmer and R. Mientus, *Thin Solid Films*, 2008, **516**, 4620–4627 (cited on pages 97, 105).

(284) K. Ellmer and R. Mientus, *Thin Solid Films*, 2008, **516**, 5829–5835 (cited on pages 97, 105).

(285) I. M. Smallwood, *Handbook of Organic Solvent Properties*, Butterworth-Heinemann, 1st edn., 1997, pp. 1–332 (cited on pages 98, 99, 106).

(286) D. Bresser, F. Mueller, M. Fiedler, R. Kloepsch, D. Baither, M. Winter, E. Paillard and S. Passerini, *Chemistry of Materials*, 2013, **25**, 4977–4985 (cited on page 100).

(287) B. Li, Q. Liu, Y. Zhang, Z. Liu and L. Geng, *Journal of Alloys and Compounds*, 2016, **680**, 343–349 (cited on page 100).

(288) A. Kafizas, C. W. Dunnill and I. P. Parkin, *Journal of Materials Chemistry*, 2010, **20**, 8336–8349 (cited on pages 102, 107).

(289) A. Kafizas, N. Noor, C. J. Carmalt and I. P. Parkin, *Journal of Materials Chemistry C*, 2013, **1**, 6335 (cited on pages 102, 107).

(290) A. Kafizas, N. Noor, P. Carmichael, D. O. Scanlon, C. J. Carmalt and I. P. Parkin, *Advanced Functional Materials*, 2014, **24**, 1758–1771 (cited on pages 102, 107, 128).

(291) W.-N. Wang, A. Purwanto, I. W. Lenggoro, K. Okuyama, H. Chang and H. D. Jang, *Industrial & Engineering Chemistry Research*, 2008, **47**, 1650–1659 (cited on pages 105, 158, 159).

(292) C. E. Knapp, J. A. Manzi, A. Kafizas, I. P. Parkin and C. J. Carmalt, *ChemPlusChem*, 2014, **79**, 1024–1029 (cited on page 106).

(293) I. A. Hassan, A. Ratnasothy, D. S. Bhachu, S. Sathasivam and C. J. Carmalt, *Australian Journal of Chemistry*, 2013, **66**, 1274–1280 (cited on page 106).

(294) M. Kitagawa, K. Mori, S. Ishihara, M. Ohno, T. Hirao, Y. Yoshioka and S. Kohiki, *Journal of Applied Physics*, 1983, **54**, 3269–3271 (cited on page 111).

(295) M. A. Martinez, M. T. Gutierrez and C Maffiotte, *Surface & Coatings Technology*, 1998, **110**, 68–72 (cited on page 111).

(296) T. Minami, H. Sato, H. Nanto and S. Takata, *Japanese Journal of Applied Physics*, 1986, **25**, L776–L779 (cited on pages 111, 112).

(297) M. Emziane, K. Durose, D. P. Halliday, N. Romeo and A. Bosio, *Thin Solid Films*, 2006, **511-512**, 66–70 (cited on page 111).

(298) H Qin, H. F. Liu and Y. Z. Yuan, *Surface Engineering*, 2013, **29**, 70–77 (cited on pages 112, 113).

(299) R. E. Treharne, L. J. Phillips, K Durose, A Weerakkody, I. Z. Mitrovic and S Hall, *Journal of Applied Physics*, 2014, **115**, 063505 (cited on page 112).

(300) V. L. Kuznetsov, A. T. Vai, M. Al-mamouri, J. S. Abell, M. Pepper and P. P. Edwards, *Applied Physics Letters*, 2015, **107**, 232103 (cited on pages 112, 113, 118, 124, 125).

(301) J. Nainaparampil and J. Zabinski, *Journal of Materials Research*, 2001, **16**, 3423–3429 (cited on pages 112, 113, 118).

(302) J. Clatot, G. Campet, A. Zeinert, C. Labrugère, M. Nistor and A. Rougier, *Solar Energy Materials and Solar Cells*, 2011, **95**, 2357–2362 (cited on pages 112, 113, 116).

(303) I. Sorar, D. Saygin-Hinczewski, M. Hinczewski and F. Z. Tepehan, *Applied Surface Science*, 2011, **257**, 7343–7349 (cited on pages 112, 118).

(304) M. H. Farooq, H.-L. Yang, X.-G. Xu, C.-J. Ran, J. Miao, M. Y. Rafique, L.-Q. Pan and Y. Jiang, *Rare Metals*, 2013, **32**, 165–168 (cited on pages 112, 113).

(305) T. Srivastava, E. G. Rini, A. Joshi, P. Shirage and S. Sen, *Journal of Nanoscience and Nanotechnology*, 2016, **16**, 1–4 (cited on page 112).

(306) H. Yuan, *Journal of Materials Science: Materials in Electronics*, 2012, **23**, 2075–2081 (cited on pages 112, 113, 115–118, 124, 125).

(307) N. Rashidi, V. L. Kuznetsov, J. R. Dilworth, M. Pepper, P. J. Dobson and P. P. Edwards, *Journal of Materials Chemistry C*, 2013, **1**, 6960 (cited on pages 112, 113, 115, 120, 124, 125).

(308) A. Jilani, M. S. Abdel-wahab, H. Y. Zahran, I. S. Yahia and A. A. Al-Ghamdi, *Applied Physics A: Materials Science and Processing*, 2016, **122**, 1–11 (cited on pages 113, 114).

(309) R. D. Shannon, *Acta Crystallographica Section A: Foundations of Crystallography*, 1976, **32**, 751–767 (cited on pages 114, 115).

(310) W. Körner and C. Elsässer, *Physical Review B - Condensed Matter and Materials Physics*, 2011, **83**, 1–6 (cited on page 115).

(311) H.-C. Wu, Y.-C. Peng and T.-P. Shen, *Materials*, 2012, **5**, 2088–2100 (cited on pages 115, 123).

(312) S. Scholz and K Jacobi, *Surface science*, 1996, **369**, 117–125 (cited on page 116).

(313) H. Yeom, T. Abukawa, Y. Takakuwa, Y. Mori, T. Shimatani, A. Kakizaki and S. Kono, *Physical Review B*, 1996, **54**, 4456–4459 (cited on page 116).

(314) T. Grehk, L. Johansson, S. Gray, M Johansson and A. Flodstrom, *Physical Review B*, 1995, **52**, 16593–16601 (cited on page 116).

(315) T. A. Dang and C. N. Chau, *J. Electrochem. Soc., Vol. 143, No. 1,* 1996, **143**, 302–305 (cited on page 116).

(316) M. R. Alexander, R. D. Short, F. R. Jones, M. Stollenwerk, J. Zabold and W. Michaeli, *Journal of Materials Science*, 1996, **31**, 1879–1885 (cited on page 116).

(317) G. M. Ingo, N. Zacchetti, D. DellaSala and C. Coluzza, *Journal of Vacuum Science & Technology A: Vacuum, Surfaces, and Films*, 1989, **7**, 3048 (cited on page 117).

(318) M. Jeske, K. G. Jung, J. W. Schultze, M. Th??nissen and H. M??nder, *Surface and Interface Analysis*, 1994, **22**, 363–366 (cited on page 117).

(319) H. Iwakuro, T. Inoue, T. Kuroda, H. Ikoma, K. Maeda, H. Ishiwara and S. Furukawa, *Japanese Journal of Applied Physics*, 1993, **32**, 5487–5495 (cited on page 117).

(320) R. Chowdhury, P. Rees, S. Adhikari, F. Scarpa and S. P. Wilks, *Physica B: Condensed Matter*, 2010, **405**, 1980–1985 (cited on page 123).

(321) N. Rashidi, A. T. Vai, V. L. Kuznetsov, J. R. Dilworth and P. P. Edwards, *Chem. Commun.*, 2015, **51**, 9280–9283 (cited on pages 125, 129, 130, 134).

(322) M. D.L. L. Olvera, A. Maldonado and R. Asomoza, *Solar Energy Materials and Solar Cells*, 2002, **73**, 425–433 (cited on page 128).

(323) F. Yakuphanoglu, Y. Caglar, S. Ilican and M. Caglar, *Physica B: Condensed Matter*, 2007, **394**, 86–92 (cited on page 128).

(324) J. Podporska-Carroll, A. Myles, B. Quilty, D. E. McCormack, R. Fagan, S. J. Hinder, D. D. Dionysiou and S. C. Pillai, *Journal of Hazardous Materials*, 2017, **324**, 39–47 (cited on page 128).

(325) B. N. Pawar, D. H. Ham, R. S. Mane, T. Ganesh, B. W. Cho and S. H. Han, *Applied Surface Science*, 2008, **254**, 6294–6297 (cited on page 132).

(326) G. Switzer and W. F. Foshag, *American Mineralogist*, 1955, **40**, 64–69 (cited on page 137).

(327) S. Nishiyama and T. Hattori, *Journal of the Ceramic Society of Japan*, 2000, **108**, 435–438 (cited on pages 137, 138).

(328) S. Matsushima, T. Tanizaki, H. Nakamura, M. Nonaka and M. Arai, *Chemistry Letters*, 2001, **30**, 1010–1011 (cited on pages 137, 138).

(329) N. Sarmadian, R. Saniz, B. Partoens and D. Lamoen, *Scientific Reports*, 2016, **6**, 20446 (cited on page 137).

(330) N. Kikuchi, H. Hosono, H. Kawazoe, O. Tanegashima, I. Ota and Y. Kimura, *Journal of the American Ceramic Society*, 2005, **88**, 2793–2797 (cited on pages 137, 138).

(331) H. Kawazoe, N. Ueda, H. Un'No, T. Omata, H. Hosono and H. Tanoue, *Journal of Applied Physics*, 1994, **76**, 7935–7941 (cited on page 138).

(332) J. Singh, N. Bhardwaj, S Uma and M. C. Group, *Bulletin of Materials Science*, 2013, **36**, 287–291 (cited on page 138).

(333) M Balasubramaniam and S Balakumar, *Materials Science in Semiconductor Processing*, 2016, **56**, 287–294 (cited on pages 138, 139).

(334) N. Arunkumar and R. Vijayaraghavan, *RSC Advances*, 2014, **4**, 65223–65231 (cited on page 138).

(335) S. C. Choi, W. S. Yun, S. H. Sohn, C.-c. Chen, L.-c. Chen, S.-j. Kuo, H. Chang, M.-j. Kao, M.-h. Yeh and L.-y. Lin, *Japanese Journal of Applied Physics*, 2012, **51**, 1–4 (cited on page 138).

(336) J. Li, K. Du, Y. Lai, Y. Chen and Z. Zhang, *J. Mater. Chem. A*, 2017, **5**, 10843–10848 (cited on page 138).

(337) C. R. Michel, N. L. López Contreras, M. A. López-Alvarez and A. H. Martínez-Preciado, *Sensors and Actuators, B: Chemical*, 2012, **171-172**, 686–690 (cited on page 138).

(338) H. Guillen-Bonilla, J. Reyes-Gómez, L. Gildo-Ortiz, M. Flores-Martínez, M. D. L. Olvera-Amador and J. Santoyo-Salazar, *Journal of Nanomaterials*, 2015, **16**, 1–8 (cited on page 138).

(339) J. Tamaki, Y. Yamada, Y. Yamamoto, M. Matsuoka and I. Ota, *Sensors and Actuators B*, 2000, **66**, 70–73 (cited on page 138).

(340) B. L. Zhu, C. S. Xie, A. H. Wang, D. W. Zeng, M. L. Hu and W. Y. Wang, *Materials Research Bulletin*, 2004, **39**, 409–415 (cited on page 138).

(341) J. P. Allen, J. J. Carey, A. Walsh, D. O. Scanlon and G. W. Watson, *Journal of Physical Chemistry C*, 2013, **117**, 14759–14769 (cited on page 140).

(342) E. A. Lewis, P. D. McNaughter, Z. Yin, Y. Chen, J. R. Brent, S. A. Saah, J. Raftery, J. A. Awudza, M. A. Malik, P. Obrien and S. J. Haigh, *Chemistry of Materials*, 2015, **27**, 2127–2136 (cited on page 143).

(343) B. Ouni, M. Haj Lakhdar, R. Boughalmi, T. Larbi, A. Boukhachem, A. Madani, K. Boubaker and M. Amlouk, *Journal of Non-Crystalline Solids*, 2013, **367**, 1–7 (cited on page 145).

(344) N. Kamarulzaman, M. F. Kasim and R. Rusdi, *Nanoscale Research Letters*, 2015, **10**, 346 (cited on page 145).

(345) A. Slassi, Y. Ziat, Z. Zarhri, M. Abdellaoui and A. Fakhim Lamrani, *Physica Scripta*, 2015, **90** (cited on page 145).

(346) G. Mie, *Annalen der Physik*, 1908, **330**, 377–445 (cited on page 157).

(347) M. I. Mishchenko and L. D. Travis, *Bulletin of the American Meteorological Society*, 2008, **89**, 1853–1861 (cited on page 157).

(348) M. I. Mishchenko, *Journal of Quantitative Spectroscopy and Radiative Transfer*, 2009, **110**, 808–832 (cited on page 157).

(349) H. Horvath, *Journal of Quantitative Spectroscopy and Radiative Transfer*, 2009, **110**, 787–799 (cited on page 157).

(350) P. I. O. Filho, D. B. Potter, M. J. Powell, C. J. Carmalt, P. Angeli and E. S. Fraga, *Proceedings of the 27th European Symposium on Computer Aided Process Engineering*, 2017, **40**, 2245–2250 (cited on page 158).

(351) W. A. H. Van Borm, J. A. C. Broekaert, R. Klockenkamper, P. Tschopel and F. C. Adams, *Spectrochimica Acta. Part B, Atomic Spectroscopy*, 1991, **46**, 1033 –1049 (cited on page 159).

(352) S. Chen, M. McLachlan, A. Sapelkin and R. Binions, *J. Mater. Chem. A*, 2015, **3**, 22311–22315 (cited on page 161).

(353) A. V. Moholkar, S. M. Pawar, K. Y. Rajpure, C. H. Bhosale and J. H. Kim, *Applied Surface Science*, 2009, **255**, 9358–9364 (cited on pages 164, 168).

(354) W.-K. Choi, J.-S. Cho, S.-K. Song, H.-J. Jung and S.-K. Koh, *Japanese Journal of Applied Physics*, 1996, **35**, 5820–5924 (cited on page 166).

(355) C Quijada, J. L. Va, F Vicent, E Morallo, D. D. I. Textil, E. P.S. D. Alcoy and U. P. D. Valencia, *Journal of applied electrochemistry*, 1998, **28**, 607–612 (cited on page 166).

(356) A. B. Christie, J. Lee, I. Sutherland and J. M. Walls, *Applications of Surface Science*, 1983, **15**, 224–237 (cited on page 167).